Dissertation
submitted to the
Combined Faculties for the Natural Sciences and for Mathematics
of the Ruperto-Carola University of Heidelberg, Germany
for the degree of
Doctor of Natural Sciences

presented by

Mrityunjay Kundu
born in West Bengal, India

Oral examination: December 12, 2007

Energy absorption, ionization, and harmonic emission in laser-irradiated atomic clusters

Referees: **PD Dr. Dieter Bauer**

Prof. Dr. Ralf S. Klessen

Zusammenfassung

Die exzellente Kopplung zwischen Laserlicht und atomaren Clustern ist bekannt und experimentell belegt. Allerdings wird der physikalische Mechanismus, welcher der Laserabsorption zugrunde liegt, noch immer kontrovers diskutiert. Lineare Resonanzabsorption (LR) tritt im Falle ausreichend langer Laserpulse bei optischen oder längeren Wellenlängen auf. Hierbei steigt die Mie-Plasmafrequenz zunächst auf Werte oberhalb der Laserfrequenz an, sinkt anschließend während der Clusterexpansion und trifft daher die Laserfrequenz zu einem bestimmten Zeitpunkt. Im Gegensatz dazu tritt LR in kurzen Pulsen nicht auf. Trotzdem besteht effiziente Energieabsorption fort. Mit Hilfe von particle-in-cell Simulationen und analytischen Modellierungen wird gezeigt, daß jene Clusterelektronen, die zur effizienten Laserabsorption beitragen eine nichtlineare Resonanz (NLR) durchlaufen, d.h., die instantane Frequenz ihrer Bewegung im zeitabhängigen, anharmonischen Potential gleicht vorübergehend der Laserfrequenz. Es wird weiterhin gezeigt, daß für vorgegebene Laserintensität und Cluster eine optimale Laserwellenlänge für die Absorption existiert, welche unter üblichen Voraussetzungen im Ultravioletten liegt. Dies bewirkt eine deutlich höhere Absorptionseffizienz, als das Ausnutzen der LR während der Expansion. Das Emissionsspektrum laserbestrahlter Cluster wird ebenfalls untersucht. Lediglich die tief gebundenen, kohärent im Clusterpotential oszillierenden Elektronen tragen zur Emission von Harmonischen niedriger Ordnung bei. Im Gegensatz dazu emittieren Elektronen, welche die NLR passieren, Strahlung mit zufälliger Phase, was die Emission hoher Harmonischer verhindert. Ein Pump-Probeexperiment zur Messung der zeitabhängigen Nanocluster-Ladungsdichte mittels Harmonischenstrahlung wird vorgeschlagen.

Abstract

The excellent coupling of laser light to atomic clusters is a known, experimentally established fact. However, the physical mechanism of laser absorption is still controversially discussed. Linear resonance (LR) absorption occurs for sufficiently long laser pulses of optical or longer wavelengths. Here the Mie-plasma frequency initially rises above the laser frequency, then drops due to cluster expansion and therefore meets the laser frequency at some point. Instead, in few-cycle laser pulses this LR is not met but efficient laser energy absorption is found to persist. By particle-in-cell simulations and analytical modelling it is shown that the cluster electrons contributing to efficient absorption pass a nonlinear resonance (NLR), i.e., the instantaneous frequency of their motion in a time-dependent, anharmonic potential transiently meets the laser frequency. For a given laser intensity and cluster it is further shown that an optimum laser wavelength for absorption exists which typically lies in the ultraviolet regime. This yields a higher laser absorption efficiency than employing LR during the cluster expansion. The emission spectrum of laser-irradiated clusters is also investigated. Only the deeply bound, coherently oscillating electrons in the cluster potential contribute to low-order harmonic emission. In contrast, electrons crossing the NLR and leaving the cluster emit radiation with random phase which inhibits high-order harmonics. A pump-probe experiment is proposed to measure the time-dependent nano-cluster charge density by detecting the harmonic radiation.

Dedication

To my mother – Bhanumoti Kundu – who passed away
when I was about to complete this thesis. As a growing
child, I saw her struggling to survive, to strive for food
and shelter for her children after my father died in her early
life. Life was not too easy for a woman in the hand-to-mouth
poverty-stricken condition in seventies. Her love, affection
to her children and determination in spite of difficulties
always inspired me. I dedicate this work in her memory.

The following peer reviewed articles were published in connection with this thesis work:

- *Nonlinear Resonance Absorption in the Laser-Cluster Interaction*,
  M. Kundu and D. Bauer, Phys. Rev. Lett. **96**, 123401 (2006).
- *Collisionless energy absorption in the short-pulse intense laser-cluster interaction*,
  M. Kundu and D. Bauer, Phys. Rev. A **74**, 063202 (2006).
- *Harmonic generation from laser-irradiated clusters*,
  M. Kundu, S.V. Popruzhenko, and D. Bauer, Phys. Rev. A **76**, 033201 (2007).

Articles in preparation:

- *Harmonic emission from laser-driven nanoplasmas*,
  S.V. Popruzhenko, M. Kundu, W. Becker, D.F. Zaretsky, and D. Bauer.
- *Optimizing the ionization and energy absorption of laser-irradiated clusters*,
  M. Kundu, S.V. Popruzhenko, and D. Bauer.

Contents

Introduction

The development of laser technology [1] during the last two decades significantly advanced the field of intense light-matter interaction. Laser pulses of intensity up to several times $10^{19}\,\mathrm{Wcm^{-2}}$, now available in various laboratories worldwide, can easily ionize matter into a hot plasma. For example, the ionization of the hydrogen atom within a fraction of a laser cycle requires an intensity $\approx 10^{14}\mathrm{Wcm^{-2}}$, which is much less than one atomic unit of laser intensity, i.e., $3.51 \times 10^{16}\mathrm{Wcm^{-2}}$. The shortest laser pulses consist of only two laser cycles within full width half maximum [2–6], corresponding to 5-6 femtoseconds (1 femtosecond = 10^{-15} seconds).

One of the primary goals of intense laser-matter interaction experiments is to deposit as much laser energy as possible into the matter because laser plasmas are of interest for the development of efficient table-top sources of x-rays, energetic keV electrons, and MeV ions. Fast ions were shown to drive nuclear fusion reactions in deuterium plasmas.

Laser-matter interaction experiments typically involve either low density gases or high density solids as targets. Gas phase targets are attractive for the generation of short wavelength radiation through the process of high harmonic generation (HHG). The harmonic frequencies may exceed 300 times the incoming fundamental frequency. Gases, however, usually show poor absorption of laser energy and produce only low x-ray yields.

Solid targets, on the other hand, often show a better absorption of laser light and particle energies up to the MeV range. Due to collisional heating, resonance absorption, and various plasma instabilities a significant fraction of the laser energy can be deposited into the solid density plasma. However, due to the presence of a highly reflective skin layer at the target front and due to the conduction of heat into the cold bulk, the conversion efficiency of laser light into electrons, ions, and x-ray photons is not optimal.

Rare-gas clusters (for example argon or xenon) with van der Waals-bonding, metal clusters with delocalized electrons, and fullerenes (e.g., C_{60} molecules) in intense laser fields have emerged as a new class of targets. Since clusters are smaller in size than a near infrared laser wavelength (800 nm in most experiments) and the plasma skin depth, no over-critical skin layer, which could act like a mirror and reflects the laser pulse, is formed at the front surface of clusters, contrary to solid targets. Therefore they can be fully penetrated by the intense laser light and can absorb the laser energy very efficiently. Almost 100% laser energy conversion in clusters was reported in experiments [7]. The high charge states of the cluster ions, generation of keV electrons, MeV ions, and x-ray photons are the consequences of this intense and efficient laser-cluster interaction [8–10].

The laser-cluster interaction scenario on which most of the researchers in the field agree upon is as follows. After the laser irradiation of a cluster, electrons first absorb energy and leave their "parent" ions (inner ionization). The total electric field (i.e., laser plus space charge field) inside the cluster may enhance inner ionization up to high charge states (ionization ignition [11, 12]). The electrons, upon absorbing laser energy and leaving the cluster, leave behind a positively charged ion background (outer ionization). This positively charged ionic background finally expands due to Coulomb repulsion and hydrodynamic pressure, thus converting electron energy into ion energy. One of the main goals of this thesis is to contribute to the understanding of the laser absorption mechanism.

The only possible routes to the absorption of laser energy are either resonances (linear or nonlinear) or non-adiabaticities (all possible kinds of collisions). Collisional ionization (absorption) is of minor importance at wavelengths $\approx 500\,\mathrm{nm}$ or greater [13–16] whereas it may be important at short wavelengths [16–18]. In this thesis, we focus on collisionless absorption processes.

For laser wavelengths $\lambda_\mathrm{l} \geq 500\,\mathrm{nm}$, immediately after the removal of the first electrons from the cluster atoms, the charge density ρ rises so fast that the Mie-plasma frequency $\omega_\mathrm{Mie}(t) = \sqrt{4\pi\rho(t)/3}$ (atomic units are used unless noted otherwise) exceeds the laser frequency ω_l. Subsequently ω_Mie decreases due to the expansion of the ionic core. Hence the "conventional" linear resonance (LR)

$$\omega_\mathrm{Mie}(t) = \omega_\mathrm{l} \tag{1}$$

occurs not before the cluster has sufficiently expanded (typically after a few hundred femtoseconds). At LR the electric field inside the cluster is enhanced instead of shielded [19] so that even higher charge states can be created and even more energy can be absorbed from the laser. The importance of LR has been demonstrated both in pump-probe experiments and simulations [20–27] with longer laser pulses. Instead, in the few-cycle ultrashort laser pulse-regime or in the early duration of long laser pulses clusters do not expand sufficiently and the LR condition (1) is never met. We show that even in this case absorption is efficient and that the dominant absorption mechanism in this regime is nonlinear resonance absorption.

In general, the eigenfrequency ω of a particle in a given potential depends on the excursion amplitude (or the energy) of the particle, $\omega = \omega[\hat{\boldsymbol{r}}]$. Figure 1 shows schematically that with increasing excursion and energy the eigenperiod of the oscillatory motion also increases and $\omega[\hat{\boldsymbol{r}}]$ decreases. In a (laser-) driven system (e.g., a cluster) the excursion amplitude is also time-dependent so that $\omega[\hat{\boldsymbol{r}}]$ may transiently meet the NLR condition

$$\omega[\hat{\boldsymbol{r}}(t)] = \omega_\mathrm{l}. \tag{2}$$

The origin of NLR lies in the anharmonicity of the cluster potential and its importance [28–33] has been pointed out previously. Until now NLR was observed only in simple model systems [30, 31, 34, 35] where electrons and ions are modelled by homogeneously charged rigid spheres. However, the many-body nature inhibited the clear identification of the absorption mechanisms in molecular dynamics or particle-in-cell (PIC) simulations. In this thesis we identify the NLR within the so-called rigid sphere model (RSM) and then

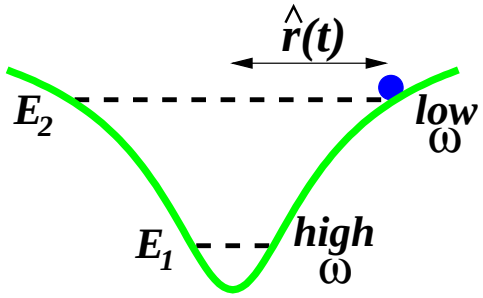

Figure 1: Dependence of the eigenfrequency ω on energy and excursion of an oscillator in an anharmonic potential. At the lower energy E_1 the oscillatory motion has a smaller period (high frequency) compared to the time period at the higher energy E_2. As the oscillator is driven up in the potential during its motion ω decreases. If ω meets the driver frequency nonlinear resonance occurs.

analyze our PIC results in the same spirit, namely in terms of nonlinear oscillators. We prove that essentially *all* electrons contributing to outer ionization pass through the NLR, so that NLR is unequivocally identified as *the* collisionless absorption mechanism when linear resonance does not occur.

The energy absorption by cluster electrons in circularly polarized laser light has received less attention so far, at least theoretically. Almost no effect of the laser polarization on the x-ray emission [36–38] and on the ion energy distribution [39] were reported in experiments with rare-gas clusters. From a theoretical point-of-view, circular polarization (CP) is particularly interesting because one may think that "collisions with the cluster boundary" may be responsible [14] for the energy absorption in linearly polarized (LP) fields. However, such collisions (i.e., reflections) would be strongly reduced in a CP field and energy absorption should be less efficient. We show that NLR occurs in CP fields as well and is equally efficient.

In a laser field the electron dynamics breaks the spherical symmetry, leading to an asymmetry in the total field which, in turn, induces an asymmetry and inhomogeneity in the ion charge distribution. Simple models usually do not take this inhomogeneity and asymmetry into account. By self-consistent PIC simulations of laser-irradiated rare-gas clusters (argon, xenon) and deuterium clusters we confirm the asymmetry in the ion energy distribution found in recent experiments [40, 41].

Due to dependencies on the various laser and cluster parameters an optimization of laser energy absorption in clusters is difficult to achieve. It is known [20–27] that the energy coupling is efficient during the LR mentioned above. However, for long pulses and long wavelengths to achieve LR the cluster plasma density has to drop significantly and the energy absorption (also the charge states) in such a low density plasma may not be optimized. A short-pulse laser of shorter wavelength may allow for an early LR during the charging of the cluster plasma. For a xenon cluster at a given laser intensity we predict that an optimized wavelength exists, typically in the ultraviolet (UV) regime.

Although HHG is under extensive study for laser-atom or laser-molecule interactions, very little is known about harmonic generation in the clustered target. In the laser-

atom or laser-molecule case HHG is understood by a three-step model where an electron executes its motion in the laser field after the ionization, is driven back to its parent ion and, upon recombination emits harmonics. However, for laser-irradiated clusters this mechanism does not work. We study harmonic emission from cluster nanoplasmas subject to short, intense infrared laser pulses. A pronounced resonant enhancement of the low-order harmonic yields is found when the Mie frequency of the ionizing and expanding cluster resonates with the respective laser harmonic frequency. We show that a strong, nonlinear resonant coupling of the cluster electrons with the laser field inhibits coherent electron motion, suppressing the emitted radiation and restricting the spectrum to only low-order harmonics. We also suggest a pump-probe scheme to monitor the ionization dynamics and charge density of expanding clusters.

The thesis is organized as follows:

Chapter 1 presents a short overview of the interaction of lasers with atomic clusters.

The main working tool to obtain the results presented in this thesis is a three-dimensional PIC code. The development of the PIC code was as an integral part of this thesis work. Necessary details are given in Chapter 2.

Chapter 3 focuses on the identification of the NLR energy absorption mechanism.

In Chapter 4 a more realistic scenario of laser-cluster interaction is presented where self-consistent inner ionization and ion motion are taken into account.

In Chapter 5 we study the optimization of ionization and laser energy absorption.

Chapter 6 is devoted to harmonic generation from clusters. Finally we conclude the thesis.

Unless noted otherwise we use atomic units ($4\pi\epsilon_0 = \hbar = a_0 = e = m_\mathrm{e} = 1$ and $c \approx 137$) in this work where ϵ_0 is the permittivity in free space, $\hbar$ is the Planck constant, a_0 is the Bohr radius, c is the light speed in vacuum, $-e$ and m_e are the charge and mass of an electron, respectively. A perturbative solution of RSM is given in appendix A. The relation between atomic units (a.u.) and SI units is given in appendix B.

Chapter 1

Basics of laser-cluster interaction

This chapter presents an overview of the prevailing theories and concepts which are necessary for the understanding of laser-cluster interaction. We start with non-relativistic classical electron dynamics in a monochromatic laser field. Relevant mechanisms of the ionization, electron heating and the cluster expansion are also discussed.

1.1 Classical electron dynamics in a laser field

Laser radiation is a transverse electromagnetic wave, usually described by the electric field $\boldsymbol{E}_\mathrm{l}$, magnetic field $\boldsymbol{B}_\mathrm{l}$ and the propagation vector $\boldsymbol{k}$ which are mutually orthogonal. In such a laser field, the motion of an electron of velocity $\boldsymbol{v}_\mathrm{e}$ is governed by Newton's second law of motion (in atomic units)

$$\frac{\mathrm{d}\boldsymbol{v}_\mathrm{e}}{\mathrm{d}t} = -\boldsymbol{E}_\mathrm{l} - (\boldsymbol{v}_\mathrm{e} \times \boldsymbol{B}_\mathrm{l})\,. \tag{1.1}$$

If the laser light is linearly polarized, the electric field can be taken as (the real part of) $\boldsymbol{E}_\mathrm{l} = \boldsymbol{E}_0 \exp(\mathrm{i}\omega_\mathrm{l} t - \mathrm{i}\boldsymbol{k}\cdot\boldsymbol{r})$ and similarly the magnetic field. For the excursion $\boldsymbol{r}(t)$ of an electron much smaller than the laser wavelength λ_l the spatial variation of the light field can be neglected. This is known as the "dipole approximation" where $\boldsymbol{E}_\mathrm{l} = \boldsymbol{E}_0 \exp(\mathrm{i}\omega_\mathrm{l} t)$. The dipole approximation implies the omission of the magnetic field so that the electron motion is in the plane of laser polarization due to the absence of the $\boldsymbol{v}_\mathrm{e} \times \boldsymbol{B}_\mathrm{l}$ drift force. Above the laser intensity $10^{18}\mathrm{Wcm}^{-2}$ for $\lambda_\mathrm{l} \approx 800$ nm, although an exact demarcation is difficult to draw, the $\boldsymbol{v}_\mathrm{e} \times \boldsymbol{B}_\mathrm{l}$ force is important due to relativistic electron velocities. Below the intensity $10^{18}\mathrm{Wcm}^{-2}$, the electron motion can be regarded as non-relativistic [42] and the dipole approximation can be applied. In this case Eq. (1.1) simplifies to the form

$$\frac{\mathrm{d}\boldsymbol{v}_\mathrm{e}}{\mathrm{d}t} = -\boldsymbol{E}_\mathrm{l}. \tag{1.2}$$

In this work we assume the validity of the dipole approximation since the cluster size (of a few nanometer) is much smaller than λ_l and the intensities considered are below

λ_l (nm)	ω_l (a.u.)	U_p (a.u.)	U_p (keV)
1056	0.0431	3830.4	103.8
800	0.0569	2198.4	59.57
600	0.0759	1236.6	33.51
300	0.152	309.1	8.377

Table 1.1: Ponderomotive energy U_p vs wavelengths at a laser intensity $10^{18}\mathrm{Wcm}^{-2}$.

$10^{18}\mathrm{Wcm}^{-2}$. For a linearly polarized laser field (along $\boldsymbol{x}$) $\boldsymbol{E}_l = E_0\hat{\boldsymbol{x}}\cos(\omega_l t)$ one finds [from the Eq.(1.2)] the velocity $v_e(t)$ and the position $x_e(t)$ of the electron as

$$v_e(t) = -\frac{E_0}{\omega_l}\sin(\omega_l t), \quad x_e(t) = -\frac{E_0}{\omega_l^2}\left[1-\cos(\omega_l t)\right], \tag{1.3}$$

assuming $v_e(0) = 0$ and $x_e(0) = 0$ at the initial time $t = 0$. Equation (1.3) gives the respective upper limit $x_{em} = E_0/\omega_l^2$ of the excursion amplitude and the velocity $v_{em} = E_0/\omega_l$ which are called the quiver amplitude and the quiver velocity of an electron during the laser pulse. Due to the oscillatory motion of the electron, the average values of the above quantities over a laser cycle are customarily used. The cycle average of the electron kinetic energy is known as the ponderomotive potential U_p, i.e.,

$$U_p = \overline{v_e^2/2} = E_0^2/(4\omega_l^2) = I_0/(4\omega_l^2). \tag{1.4}$$

Here we have used $I_0 = E_0^2$. If the ponderomotive energy U_p of an electron approaches its rest-mass energy $m_e c^2$, relativistic electron dynamics set in. This can happen either through an increase of the laser intensity or an increase of the laser wavelength, as is evident from Eq. (1.4). Table 1.1 lists U_p at different laser wavelengths for an intensity $I_0 = 10^{18}\mathrm{Wcm}^{-2}$. U_p becomes comparable to the rest mass-energy of the electron i.e., $m_e c^2 = 0.51$ MeV with increasing laser wavelength. However with the lasers operating in the optical and near infrared frequency range (< 1100 nm) the electron dynamics can be considered non-relativistic if the laser intensity is below $10^{18}\mathrm{Wcm}^{-2}$.

1.2 Ionization processes of atoms

The interaction of the laser field with an atomic cluster leads to the removal of electrons from the different atomic shells and the creation of ions of different charge states. This is known as cluster *inner ionization*. Depending upon the laser intensity and the laser wavelength different processes of inner ionization become significant. Although ionization of isolated atoms is different from the ionization of atoms aggregated to a cluster, a theoretical description of the inner ionization of rare-gas atomic clusters often uses the atomic ionization concepts which can be grouped into two broad categories: (i) ionization by the external laser field and (ii) ionization due to the collisions of electrons with ions. In the context of ionization of atoms by laser fields, the ponderomotive potential U_p [in

Eq. (1.4)] enters another important parameter

$$\gamma = \sqrt{I_\mathrm{p}/2U_\mathrm{p}} \tag{1.5}$$

for an atom of ionization potential I_p. γ is called the Keldysh parameter [43] which is often used to distinguish the multiphoton ionization regime [44–49] from the tunnel ionization [48–51] regime of atoms (see below). When $\gamma < 1$ atomic ionization proceeds either via tunneling or over-the-barrier [48–50, 52] while $\gamma > 1$ indicates the multiphoton process of ionization. In the following we briefly discuss different processes of atomic ionization.

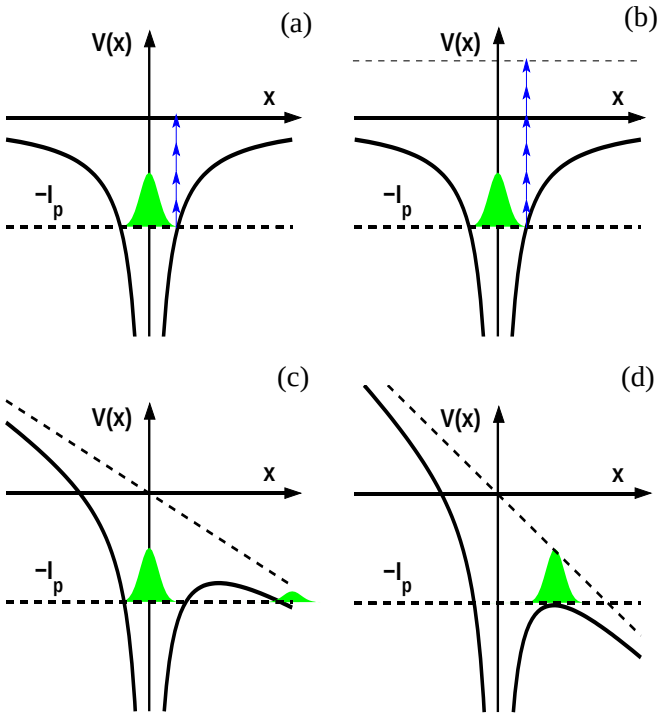

Figure 1.1: (a) Multiphoton ionization (MPI): electron with binding energy $-I_\mathrm{p}$ absorbs n laser photons (indicated by up-arrows) each having energy $\hbar\omega_\mathrm{l}$ and escapes from the atom with minimal kinetic energy. (b) Above threshold ionization (ATI): in this case an electron absorbs more photons than required and escapes from the atom with higher momentum. (c) Tunnelling ionization (TI): the laser field is strong enough to disturb the atomic potential but the barrier remains above the binding energy. In this case there is a (small) probability that the electron wave-packet tunnels through the barrier. (d) Over-the-barrier ionization (OBI): the laser field is very strong, depleting the barrier below the ionization level $-I_\mathrm{p}$ so that the electron escapes over-the-barrier (classically).

1.2.1 Multiphoton ionization

Multiphoton ionization (MPI) is the ionization of an atom by absorbing more than one photon of the incident electromagnetic wave. MPI can be understood quantum mechanically [45–48] in higher order perturbation theory which we omit here. Schematically it is illustrated in Fig. 1.1(a). By this process an electron acquires an energy higher than the ionization potential of the atom and becomes free. If a number s of laser photons in excess of the minimum number n required for ionization is absorbed, the electron leaves the atom with an excess energy

$$E_{\mathrm{f}} = (n+s)\hbar\omega_{\mathrm{l}} - I_{\mathrm{p}} \tag{1.6}$$

which is a generalization of Einstein's equation for the photoelectric effect. The case $s \neq 0$ [see Fig. 1.1(b)] is called above threshold ionization (ATI) [42, 44, 48, 53].

1.2.2 Tunnelling ionization

For laser intensities above $10^{14}\mathrm{Wcm}^{-2}$ but below $10^{15}\mathrm{Wcm}^{-2}$, the driver field is strong enough to distort the atomic potential [42, 48–50]. Moreover, the laser period is long on an atomic time scale so that a quasi-static viewpoint is applicable. The net effective potential $V(x)$ "seen" by the electron (in an ion of charge number $\mathcal{Z}$) is given by [52, 54]

$$V(x) = -\mathcal{Z}/|x| - x|E_{\mathrm{l}}| \tag{1.7}$$

in a.u. At the instant when the quasi-static laser field E_{l} points in $-x$-direction the electron tunnels out in $+x$-direction. Then E_{l} should be taken as E_0. This is schematically shown in Fig. 1.1(c) along the polarization axis. The existence of a barrier permits tunnelling of the electron wave packet into the continuum. This is known as tunnelling ionization (TI) which can be described by semi-classical approaches [51].

1.2.3 Over-the-barrier-ionization

For even higher laser intensities, the driver field is so strong that the initial electron energy level is above the barrier, which is schematically shown in Fig. 1.1(d). The ejection of the electron wave-packet above the barrier is known as over-the-barrier-ionization (OBI) [42, 48, 52]. Differentiating $V(x)$ [in Eq. (1.7)] with respect to the excursion x, and demanding that the effective force $\partial V/\partial x = \mathcal{Z}/x^2 - E_{\mathrm{l}}$ vanishes at the barrier location x_{b} one finds $x_{\mathrm{b}} = \sqrt{\mathcal{Z}/E_{\mathrm{l}}}$ and the potential $V(x_{\mathrm{b}}) = -2x_{\mathrm{b}}E_{\mathrm{l}} = -2\sqrt{\mathcal{Z}E_{\mathrm{l}}}$ at x_{b}. Equating $V(x_{\mathrm{b}})$ with the ionization potential $I_{\mathrm{p}}(\mathcal{Z})$ of the atom of charge number $\mathcal{Z}$, we obtain $I_{\mathrm{p}}(\mathcal{Z}) = -2\sqrt{\mathcal{Z}E_{\mathrm{l}}}$, which at the field maxima ($|E_{\mathrm{l}}| = E_0$) yields the critical laser field E_{crit}, i.e.,

$$E_{\mathrm{crit}} = I_{\mathrm{p}}^2(\mathcal{Z})/(4\mathcal{Z}) \tag{1.8}$$

required to ionize the atom with a probability close to unity. The corresponding intensity $I_{\mathrm{app}} = E_{\mathrm{crit}}^2$ is called the appearance intensity, which reads (in atomic units)

$$I_{\mathrm{app}} = I_{\mathrm{p}}^4(\mathcal{Z})/(16\mathcal{Z}^2). \tag{1.9}$$

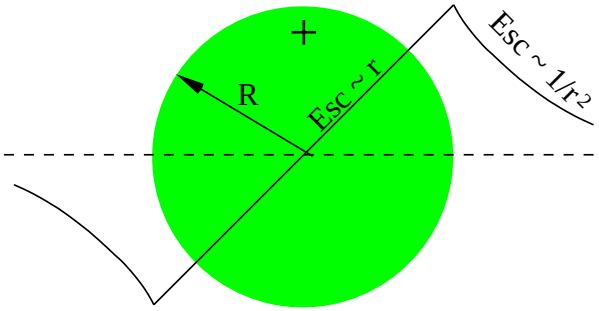

Figure 1.2: Scheme of ionization ignition due to the static electric field E_{sc} of the ionic background. The higher value of the field at the cluster surface creates higher charge states there than in the cluster interior where the static field is lower.

In fact, a very good agreement [54–56] between the appearance intensities as predicted by the OBI model Eq. (1.9) and the respective experimental values for multiply charged noble gas atoms was obtained in a range of laser intensities $\approx 10^{14}\mathrm{Wcm}^{-2} - 10^{17}\mathrm{Wcm}^{-2}$, indicating that the OBI model can be applied to the ionization of atoms at laser intensities of interest in this work. Hence, although each of the above mentioned optical processes (i.e., MPI, ATI, TI and OBI) contribute, we only consider the dominant process, OBI.

1.2.4 Ionization by the space charge field

Due to the finite size of the cluster and the collective coherent oscillation of the electron cloud against the almost static ionic background, an additional electric field appears owing to space charge imbalances. In the beginning of this process atoms have to be already in ionized states so that an electronic and an ionic cloud form. Figure 1.2 schematically illustrates the static electric field in the absence of electrons. This static field, being maximum at the cluster surface, creates higher charge states of the ions at the surface than in the cluster interior. The ionic field may exceed the applied laser field. For example, a xenon cluster of radius $R = 7$ nm and number of atoms $N = 17256$ gives a field (at the boundary, assuming all atoms are singly charged) $E_{sc} \approx 0.9855$ a.u. which would be equivalent to a laser intensity $\approx 3.4 \times 10^{16}\mathrm{Wcm}^{-2}$ capable of producing even higher charge states up to $\mathcal{Z} = 8$. The additional electric field adds up to the applied laser field and the augmented total field can cause enhanced ionization of an ion inside the cluster. The enhanced ionization further increases the field causing further ionization, hence the name *ionization ignition* [11,12]. However ionization ignition does not continue indefinitely because the removal of electrons from the cluster saturates at some point. The presence of electrons counteracts ionization ignition. As higher charge states are created the ionization potentials increase in a discrete manner due to the higher ionization thresholds of electrons in deeper atomic shells. If the total field cannot meet the required field for ionization of the next shell inner ionization saturates and ionization ignition stops. Ionization ignition causes important effects: (i) it creates higher ionic charge states than possible with the laser field alone, (ii) the space charge field being larger at the cluster boundary than in the center, the ions at the cluster boundary attain higher charges than

the ions in the cluster core by the ionization ignition. Finally, the space charge field leads to a Coulomb explosion [10,37,41,57] of the ionic background more violent than expected from charge states generated by the laser alone.

1.2.5 Ionization by collisions

Although the optical field ionization (OFI) of atoms is the dominant process of ionization in the case of clusters as well, the high atomic density inside the cluster permits ionization due to inelastic collisions of electrons with ions. Collisional ionization (CI) depends on the electron density n_e and the electron temperature T_e. Both the thermal electrons and the electrons driven back to the cluster by the laser field will contribute to the CI. The rate R_T^ci (due to the thermal electron motion) of CI can be determined by the equation

$$R_\mathrm{T}^\mathrm{ci} = n_\mathrm{e}\overline{v_\mathrm{e}\sigma_i} \tag{1.10}$$

with the empirical Lotz [58,59] ionization cross section

$$\sigma_i = \alpha_i q_i \frac{\ln(K_\mathrm{e}/I_\mathrm{p})}{K_\mathrm{e} I_\mathrm{p}}. \tag{1.11}$$

Here $\alpha_i = 2.17$ is an empirical parameter, q_i is the number of electrons in the valence shell of the ion encountering the collision, I_p is its ionization potential and $K_\mathrm{e} = v_\mathrm{e}^2/2$ is the electron kinetic energy. Assuming a Maxwellian distribution of electrons the probability density $f_e(K_\mathrm{e})$ of electrons in the energy range between K_e and $K_\mathrm{e} + \mathrm{d}K_\mathrm{e}$ obeys

$$f_e(K_\mathrm{e})\,\mathrm{d}K_\mathrm{e} = 2\sqrt{\frac{K_\mathrm{e}}{\pi(\kappa T_\mathrm{e})^3}}\exp\left(-K_\mathrm{e}/\kappa T_\mathrm{e}\right)\,\mathrm{d}K_\mathrm{e}, \tag{1.12}$$

with κ the Boltzmann constant. Equations (1.10), (1.11) and (1.12) yield

$$R_\mathrm{T}^\mathrm{ci} = 2\alpha_i q_i n_\mathrm{e}\int_{I_\mathrm{p}}^{\infty}\sqrt{\frac{2}{\pi(\kappa T_\mathrm{e})^3}}\frac{\ln(K_\mathrm{e}/I_\mathrm{p})}{I_\mathrm{p}}\exp\left(-K_\mathrm{e}/\kappa T_\mathrm{e}\right)\,\mathrm{d}K_\mathrm{e}, \tag{1.13}$$

which can be evaluated numerically. The lower limit I_p indicates that no ionization takes place if $K_\mathrm{e} < I_\mathrm{p}$. Similarly the rate of CI due to the laser driven electron collisions can be estimated by $R_\mathrm{L}^\mathrm{ci} = n_\mathrm{e}\overline{v_\mathrm{e}\sigma_i}$, using the characteristic electron velocity $v_\mathrm{e} = -(E_0/\omega_\mathrm{l})\sin(\omega_\mathrm{l}t)$ from Eq. (1.3). The average ionization rate over a laser period T is

$$R_\mathrm{L}^\mathrm{ci} = \frac{4n_\mathrm{e}}{T}\int_{t_\mathrm{i}}^{T/4}\sigma_i\frac{E_0}{\omega_\mathrm{l}}\sin(\omega_\mathrm{l}t)\,\mathrm{d}t = \frac{2n_\mathrm{e}}{\pi}\int_{\tau_\mathrm{i}}^{\pi/2}\sigma_i\frac{E_0}{\omega_\mathrm{l}}\sin\tau\,\mathrm{d}\tau, \tag{1.14}$$

where $\tau = \omega_\mathrm{l}t$ is the normalized time and $\tau_\mathrm{i} = \omega_\mathrm{l}t_\mathrm{i}$ is the initial time when the kinetic energy of the electron is equal to the ionization potential I_p of the atom or ion. With the instantaneous electron kinetic energy $K_\mathrm{e} = v_\mathrm{e}^2/2 = 2U_\mathrm{p}\sin^2\tau$ we can write $\sin\tau\,\mathrm{d}\tau = \mathrm{d}K_\mathrm{e}/(4U_\mathrm{p}\sqrt{1 - K_\mathrm{e}/2U_\mathrm{p}})$. Substituting σ_i and $\sin\tau\,\mathrm{d}\tau$ in Eq. (1.14) one obtains

$$R_\mathrm{L}^\mathrm{ci} = \frac{n_\mathrm{e}\alpha_i q_i}{\pi I_\mathrm{p}\sqrt{U_\mathrm{p}}}\int_{I_\mathrm{p}}^{2U_\mathrm{p}}\frac{\ln(K_\mathrm{e}/I_\mathrm{p})}{K_\mathrm{e} I_\mathrm{p}}\frac{\mathrm{d}K_\mathrm{e}}{\sqrt{1 - K_\mathrm{e}/2U_\mathrm{p}}}, \tag{1.15}$$

which can also be evaluated numerically. It is clear that, both U_p and T_e increase with the applied laser intensity. As a result R_T^ci and R_L^ci decrease and they become relatively unimportant compared to the ionization by the laser field, as discussed before. In this thesis we neglect all collisional effects so that ionization is due to the laser field and ionization ignition.

1.3 Mie-plasma frequency

If one displaces the electrons in a bulk plasma slightly with respect to the ions the restoring force leads to oscillations of electrons at the so-called plasma frequency [60]. The electron plasma frequency ω_pe is given by the expression $\omega_\mathrm{pe} = \sqrt{4\pi n_\mathrm{e} e^2/m_\mathrm{e}}$. As long as the plasma is neutral we can write $n_\mathrm{e} = \mathcal{Z} n_\mathrm{i}$, the charge density of the ion background $\rho = e n_\mathrm{e}$ and the electron plasma frequency as $\omega_\mathrm{p} = \omega_\mathrm{pe} = \sqrt{4\pi\rho e/m_e}$.

The space charge field $\boldsymbol{E}_\mathrm{sc}$ inside the plasma can be obtained by Gauss' law [61]

$$\oint_A \boldsymbol{E}_\mathrm{sc} \cdot \mathrm{d}\boldsymbol{A} = 4\pi \int_\Gamma \rho \,\mathrm{d}\Gamma \tag{1.16}$$

where A is the surface enclosing the volume Γ of a homogeneous rectangular plasma slab of density ρ. Initially, electron and ion slab overlap. If the electron slab is displaced by $\boldsymbol{x}$, the restoring force $\boldsymbol{F} = -e\boldsymbol{E}_\mathrm{sc}$ on an electron at a distance $\boldsymbol{x}$ is $\boldsymbol{F} = -e\boldsymbol{E}_\mathrm{sc} = -4\pi e^2 n_\mathrm{e} \boldsymbol{x}$ and the equation of motion for the electron thus reads

$$\ddot{\boldsymbol{x}}(t) = -\left(4\pi e^2 n_\mathrm{e}/m_\mathrm{e}\right) \boldsymbol{x} = -\omega_\mathrm{p}^2 \boldsymbol{x}. \tag{1.17}$$

Hence the electrons oscillate with the plasma frequency ω_p [60]. The frequency ω_p sets an important criterion for the laser field impinging on a plasma layer. It determines the penetration depth $\sim c/\omega_\mathrm{p}$ of laser light of frequency ω_l into the plasma [62]. If $\omega_\mathrm{p} > \omega_\mathrm{l}$, which is often the case for solid density plasmas, the plasma is called over-dense. In this case the laser light is reflected. In the opposite situation $\omega_\mathrm{p} < \omega_\mathrm{l}$ the plasma is under-dense and the laser can propagate inside the plasma. The charge density for which $\omega_\mathrm{p} = \omega_\mathrm{l}$ occurs is called critical plasma density ρ_c which relates to the laser frequency as

$$\omega_\mathrm{l}^2 = 4\pi e^2 \rho_\mathrm{c}/m_\mathrm{e}. \tag{1.18}$$

Unlike the plasma slab geometry considered above, cluster plasmas can be often considered spherical. The spherical electron cloud oscillates about the center of the ion cloud. For an electron at $\boldsymbol{x} = r\hat{\boldsymbol{x}}$ from the center of the ion sphere ($r < R$ is the distance from the center of the cluster of radius R) Gauss' law yields $\boldsymbol{E}_\mathrm{sc}(4\pi r^2) = 4\pi e n_\mathrm{e}(4\pi r^3/3)\,\hat{\boldsymbol{x}}$ which leads to the equation of motion of the electron sphere

$$\ddot{\boldsymbol{x}}(t) = -(\omega_\mathrm{p}^2/3)\,\boldsymbol{x}. \tag{1.19}$$

The factor 1/3 appears due to the spherical geometry. The spherical electron cloud oscillates with a frequency $\omega_\mathrm{p}/\sqrt{3}$, which is known as the Mie-plasma (or surface plasmon) frequency

$$\omega_\mathrm{Mie} = \omega_\mathrm{p}/\sqrt{3}. \tag{1.20}$$

It plays a significant role for the efficiency of the laser-cluster energy coupling and for the harmonic radiation from clusters, as will be seen in chapters 5 and 6.

1.4 Cluster heating processes

The electrons and ions, which are produced after the ionization of the cluster atoms, will execute their motion in the combined field of the laser and the space charge due to the ions and the electrons. The laser energy is initially coupled to the electrons which are much lighter than the ions. The massive ions, on the other hand, are less disturbed by the laser field and their dynamics are relatively well understood as the repulsion among them due to the Coulomb field which dominates the laser field.

In the context of laser-cluster interaction the mechanism of electron heating was not well understood. This section describes several mechanisms which were proposed to explain the efficient energy coupling to the cluster electrons.

It should be emphasized that all phenomena of energy absorption, independent of the underlying mechanism(s), must obey Poynting's theorem [62] which requires a phase difference of the electron current density $\boldsymbol{j}_\mathrm{e}$ with respect to the laser field $\boldsymbol{E}_\mathrm{l}$ different from $\pi/2$. Poynting's theorem states that the rate of change of electromagnetic energy density $\mathcal{U}$ in an extended medium (e.g., cluster) is equal to the divergence of Poynting's vector $\boldsymbol{S} = \boldsymbol{E}_\mathrm{l} \times \boldsymbol{B}_\mathrm{l}$. Mathematically it reads,

$$\frac{\partial \mathcal{U}}{\partial t} = -\boldsymbol{\nabla} \cdot \boldsymbol{S} = \boldsymbol{E}_\mathrm{l} \cdot \boldsymbol{\nabla} \times \boldsymbol{B}_\mathrm{l} - \boldsymbol{B}_\mathrm{l} \cdot \boldsymbol{\nabla} \times \boldsymbol{E}_\mathrm{l}. \tag{1.21}$$

Applying Faraday's law $\boldsymbol{\nabla} \times \boldsymbol{E}_\mathrm{l} = -\frac{\partial \boldsymbol{B}_\mathrm{l}}{\partial t}$ and Ampere's law $\boldsymbol{\nabla} \times \boldsymbol{B}_\mathrm{l} = \boldsymbol{j}_\mathrm{e} + \frac{\partial \boldsymbol{E}_\mathrm{l}}{\partial t}$, and averaging over a laser period T one obtains

$$\overline{\dot{\mathcal{U}}} = -\overline{\boldsymbol{\nabla} \cdot \boldsymbol{S}} = \overline{\boldsymbol{j}_\mathrm{e} \cdot \boldsymbol{E}_\mathrm{l}}. \tag{1.22}$$

Note that the integral $\int_0^T \left(\boldsymbol{E}_\mathrm{l} \cdot \frac{\partial \boldsymbol{E}_\mathrm{l}}{\partial t} + \boldsymbol{B}_\mathrm{l} \cdot \frac{\partial \boldsymbol{B}_\mathrm{l}}{\partial t} \right) \mathrm{d}t$ vanishes for sinusoidal fields. Clearly, a phase $\delta = \pi/2$ between $\boldsymbol{j}_\mathrm{e}$ and $\boldsymbol{E}_\mathrm{l}$ yields $\overline{\dot{\mathcal{U}}} = \overline{\boldsymbol{j}_\mathrm{e} \cdot \boldsymbol{E}_\mathrm{l}} = 0$. In this case energy absorption does not occur at all. Therefore $\overline{\boldsymbol{j}_\mathrm{e} \cdot \boldsymbol{E}_\mathrm{l}} \neq 0$, i.e., $\delta \neq \pi/2$ is a necessary criterion for absorption irrespective of the mechanism(s) leading to this required dephasing.

1.4.1 Collisional heating

Collisional heating (CH) or "inverse bremsstrahlung" (IB) heating occurs due to frequent electron-ion collisions. The electron-ion collision frequency ν_ei [60] reads (in atomic units)

$$\nu_\mathrm{ei} = \frac{4\sqrt{2\pi}\mathcal{Z} n_\mathrm{e}}{3T_\mathrm{e}^{3/2}} \ln \Lambda. \tag{1.23}$$

Λ is the standard Coulomb logarithm usually in the range $10-20$, as is known from plasma kinetic theory [60]. The validity of Eq. (1.23) relies on the establishment of an electron

temperature T_e and an electron density n_e, i.e., rapid thermalization of the electrons by frequent collisions among themselves is needed during the laser pulse. In a linearly polarized laser field $E_l = E_0 \cos(\omega_l t)$ a free electron has a quiver energy $E_l^2/2\omega_l^2$. When this electron collides with an ion at a frequency ν_{ei}, the rate of change of energy U can be estimated by [6]

$$\frac{dU}{dt} = \nu_{ei} \frac{E_l^2}{2\omega_l^2}, \tag{1.24}$$

which determines the rate of collisional absorption. Assuming $T_e = U_p$ one obtains $dU/dt \propto \lambda_l^{-1} I_0^{-1/2}$. It implies that at higher laser intensities, and near infrared wavelengths CH plays a nominal role since ν_{ei} decreases rapidly as the temperature rises to higher values, e.g., T_e in the keV regime. At low laser intensities as well as shorter laser wavelength CH has to be taken into account.

1.4.2 Vacuum heating

It was proposed by Brunel [63] that when a linearly polarized intense laser pulse strikes obliquely a metallic surface or a sharply bounded over-dense plasma layer, the laser field pulls the electrons out of the surface into the vacuum and then push them back into the plasma with velocities approximately equal to the quiver velocity E_0/ω_l. The electrons then emerge at the rear side or vanish into the bulk. If the phase of the laser field matches with those of the emerging electrons they may gain more energy from the laser field. Although this mechanism was initially proposed for the case of laser-solid interaction, the applicability of the this mechanism in the case of atomic clusters with a size of only a few nanometer is not well justified. Nevertheless, the terminology "vacuum heating" was used [28, 29, 64] for the case of clusters too.

1.4.3 Resonance heating

Resonance between the laser frequency and the Mie-plasma frequency or the time dependent eigen-frequency of an electron in the anharmonic cluster potential leads to significant heating of electrons. If the resonance is met while the laser is on, resonance heating is the dominant process of energy absorption in clusters.

Nanoplasma model

One of the first phenomenological models used to describe the energy absorption and heating of quasi-free cluster electrons was the nanoplasma model [19] which treats the cluster as a dielectric sphere. This is basically a hydrodynamic (fluid) model which considers absorption of laser energy by electrons predominantly due to electron-ion collisions occurring at a frequency ν_{ei}. The temperature is assumed uniform while the time-dependent charge density $\rho(t)$ is taken into account in the time dependence of the dielectric constant

$\varepsilon(t, \omega_\mathrm{l})$ given by the Drude model

$$\varepsilon(t, \omega_\mathrm{l}) = 1 - \frac{4\pi\rho(t)}{\omega_\mathrm{l}(\omega_\mathrm{l} + \mathrm{i}\nu_\mathrm{ei})} = 1 - \frac{\rho/\rho_\mathrm{c}}{(1 + \nu_\mathrm{ei}^2/\omega_\mathrm{l}^2)} + \mathrm{i}\frac{\rho/\rho_\mathrm{c} \cdot \nu_\mathrm{ei}/\omega_\mathrm{l}}{(1 + \nu_\mathrm{ei}^2/\omega_\mathrm{l}^2)}. \tag{1.25}$$

The field inside the dielectric sphere in terms of the external laser field can be written as

$$E = \frac{3E_\mathrm{l}}{|2 + \varepsilon(t, \omega_\mathrm{l})|}. \tag{1.26}$$

The electrostatic energy density $\mathcal{U}$ of a dielectric medium is $\mathcal{U} = \varepsilon E^2/8\pi$. The heating rate can be obtained by considering the rate of deposition of laser energy in the dielectric sphere. The energy deposited per unit volume in the cluster is

$$\frac{\partial \mathcal{U}}{\partial t} = \frac{1}{4\pi}\boldsymbol{E} \cdot \frac{\partial \boldsymbol{D}}{\partial t} \tag{1.27}$$

where $\boldsymbol{D} = \varepsilon \boldsymbol{E}$ is the induced dipole moment inside the dielectric sphere. After averaging over a laser cycle the average rate of deposited energy density can be written as [19]

$$\frac{\partial \mathcal{U}}{\partial t} = \frac{9\omega_\mathrm{l}}{8\pi}\frac{\mathrm{Im}[\varepsilon]E_0^2}{|2 + \varepsilon(t, \omega_\mathrm{l})|^2}. \tag{1.28}$$

Note that when the electron density inside the cluster is high, i.e., when $\rho \gg 3\rho_\mathrm{c}$ then the field inside the cluster is smaller than the field outside. This shielding results in a decrease of the heating rate. When $\rho = 3\rho_\mathrm{c}$, the linear resonance $\omega_\mathrm{Mie} = \sqrt{4\pi\rho/3} = \omega_\mathrm{l}$ occurs and the denominator $|2 + \varepsilon(t, \omega_\mathrm{l})|$ passes through the minimum, causing enhancement of the heating rate inside the cluster. The relative height and width of the resonance are determined by the collision frequency ν_ei. In the absence of collisions, i.e., ν_ei approaching zero, the width of the resonance vanishes according to the nanoplasma model.

During the first cycles of a laser pulse the cluster charge density rises due to inner ionization, and ω_Mie remains above the laser frequency ω_l (for the optical and infrared wavelengths or longer). As the ionic background expands due to the mutual Coulomb repulsion and the hydrodynamic pressure (described in Sec. 1.5), the charge density decreases, leading to the decrease of the Mie-resonance frequency. Linear resonance $\omega_\mathrm{Mie} = \omega_\mathrm{l}$ is thus met after a longer time (typically > 50 fs) during the expansion.

Hence for a short, few-cycle laser pulse the ionic sphere does not expand sufficiently to meet the linear resonance. In this case linear resonance theory is inapplicable. We shall show that energy absorption is still possible via nonlinear resonance.

Rigid sphere model

Ions being massive, their motion can be neglected in short laser pulses. This applies to the early part of long laser pulses as well. In a first approximation the electrons can also be approximated by a sphere of negative charge which remains rigid during the entire laser pulse. The homogeneously charged electron cloud oscillates back and forth against the positively charged ion cloud driven by the oscillating laser field. Figure 1.3 shows

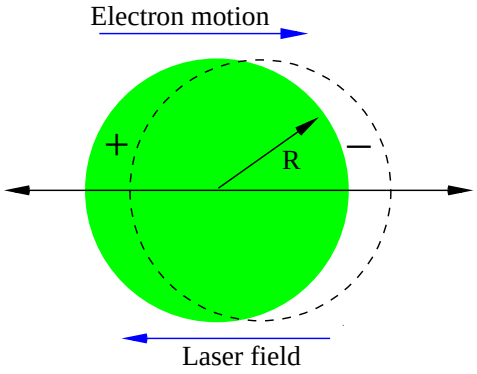

Figure 1.3: The rigid sphere model. The positively charged ion sphere is at rest due to the high inertia. The negatively charged electron sphere oscillates against the ion sphere, driven by a laser field.

schematically the rigid sphere model (RSM). Although the rigid sphere model is a very simple approximation of clusters, it provides significant qualitative understanding. In a first approximation we assume the radius of the electron sphere being equal to the radius of the ion sphere. At a high intensity, an expanded electron sphere [30, 31] may be more realistic. The center of mass of the electron-ion system is located very close to the center of the ion sphere. The equation of motion of the electron center of mass in a linearly polarized laser field, polarized along x, can be written as (in atomic units)

$$\frac{\mathrm{d}^2\bar{r}}{\mathrm{d}\tau^2} + \mathrm{sgn}(x)g(r) = -\frac{E_\mathrm{l}(\tau)}{R\omega_\mathrm{l}^2}, \tag{1.29}$$

where $\bar{r} = x/R$, $r = |\bar{r}|$ is the normalized excursion of the electron sphere and $\tau = \omega_\mathrm{l} t$ is the normalized time. The quantity $E_\mathrm{l}(\tau)/R\omega_\mathrm{l}^2$ is the dimensionless driver amplitude which is the excursion amplitude of a free electron divided by the cluster radius. The dimensionless electrostatic restoring force reads

$$g(r) = \left(\frac{\omega_\mathrm{Mie}}{\omega_\mathrm{l}}\right)^2 \times \begin{cases} r - \frac{9r^2}{16} + \frac{r^4}{32} & 0 \le r \le 2 \\ r^{-2} & r \ge 2. \end{cases} \tag{1.30}$$

The first term in the upper line of $g(r)$ is the linear force when the displacement of the electron sphere is small, the next two terms are nonlinear terms which appear due to the partial overlap of the electron cloud with the ion cloud. The term r^{-2} is the Coulomb force, valid for the complete separation of the electron sphere from the ion sphere. As was observed in Ref. [30] the absorption of laser energy in the RSM is characterized by a threshold driver strength below which absorption is negligible (harmonic regime) and above which absorption is almost constant. Figure 1.4 shows this threshold behavior for $\omega_\mathrm{Mie}/\omega_\mathrm{l} = 3.65$ and an $n = 8$-cycle $\sin^2$-pulse $E_\mathrm{l}(\tau) = E_0 \sin^2(\tau/2n)\cos(\tau)$.

In the RSM the expansion of the cluster is not essential for efficient energy absorption, contrary to the nanoplasma model. Therefore the RSM can be applied to short laser pulses in order to understand the laser energy absorption in this regime. In most part of this thesis we shall assume short laser pulses and often apply the RSM in different contexts.

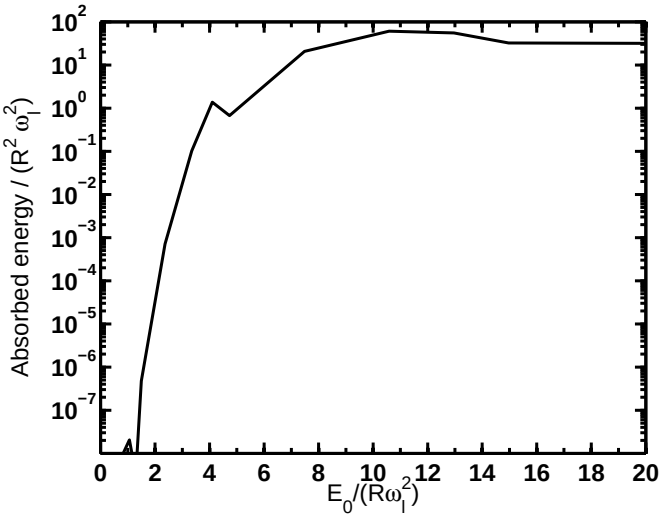

Figure 1.4: Laser absorption vs driver amplitude in the rigid sphere-model (1.29) for $\omega_{\mathrm{Mie}}/\omega_{\mathrm{l}} = 3.65$, $E_{\mathrm{l}}(\tau) = E_0 \sin^2(\tau/2n)\cos(\tau)$, $n = 8$. The nonlinear resonance is passed once the threshold driver amplitude ≈ 2.0 is reached.

1.5 Cluster expansion processes

The expansion of an ionized cluster strongly depends upon the number of electrons removed from the cluster during the laser pulse. Early removal of electrons triggers an early expansion dynamics of the ions. Small clusters retain less electrons than bigger ones which have higher restoring forces on the electrons. If the laser field is not strong enough to remove a large number of electrons from the cluster an almost quasi-neutral plasma sphere is formed which expands hydrodynamically. In general, both hydrodynamic and Coulomb pressure drive the expansion due to which ions gain energy.

1.5.1 Hydrodynamic expansion

In the hydrodynamic description of plasmas [60], electrons and ions are considered charged fluids. Due to binary collisions among the ions, an ion temperature T_{i} builds up. Similarly the temperature T_{e} of the electron fluid builds up due to electron-electron collisions. Since electrons are more mobile than ions, the thermalization of electrons takes place much faster, and T_{e} exceeds T_{i}. If a substantial fraction of the electrons does not leave the slowly moving ion background the interior of the cluster is quasi-neutral. The expansion of such a cluster is known as hydrodynamic expansion. The energy relation [6] (in a.u.)

$$\frac{1}{2} M_{\mathrm{i}} \left(\frac{\mathrm{d}R}{\mathrm{d}t} \right)^2 = \frac{3}{2} T_{\mathrm{i}}, \tag{1.31}$$

of the ions sitting at the cluster boundary gives the rate at which the cluster radius R expands. Equation (1.31) equals the ion kinetic energy to the internal energy. To calculate R, one should determine T_{i} before. The hydrodynamic pressure P_{e} of the quasi-neutral

plasma is determined by

$$P_\mathrm{e} = n_\mathrm{e} T_\mathrm{e}. \tag{1.32}$$

Due to this pressure the electron fluid expands and the internal energy $\frac{3}{2} V n_\mathrm{e} T_\mathrm{e}$ of the electron fluid decreases as the cluster volume $V = 4\pi R^3/3$ grows. The decrease of the internal electron energy due to the increase of the cluster volume $\mathrm{d}V$ is given by

$$-2P_\mathrm{e}\,\mathrm{d}V = 3Vn_\mathrm{e}\,\mathrm{d}T_\mathrm{e}. \tag{1.33}$$

Equations (1.32) and (1.33) yield $-2\,\mathrm{d}R/R = \mathrm{d}T_\mathrm{e}/T_\mathrm{e}$, which gives the temperature

$$T_\mathrm{e} = T_{\mathrm{e}0}\left(R_0/R\right)^2. \tag{1.34}$$

Here R_0 and $T_{\mathrm{e}0}$ are the initial radius of the cluster and the initial electron temperature. Clearly, the electron temperature drops due to the expansion of the hot electron cloud. The energy balance reads [6]

$$-\frac{3}{2} V n_\mathrm{e} \frac{\mathrm{d}T_\mathrm{e}}{\mathrm{d}t} = \frac{3}{2} V n_\mathrm{i} \frac{\mathrm{d}T_\mathrm{i}}{\mathrm{d}t}, \tag{1.35}$$

which simplifies to

$$\frac{\mathrm{d}T_\mathrm{i}}{\mathrm{d}t} = -\frac{n_\mathrm{e}}{n_\mathrm{i}} \frac{\mathrm{d}T_\mathrm{e}}{\mathrm{d}t} = 2\frac{n_\mathrm{e}}{n_\mathrm{i}} \frac{T_{\mathrm{e}0}}{R} \left(\frac{R_0}{R}\right)^2 \frac{\mathrm{d}R}{\mathrm{d}t}. \tag{1.36}$$

If Q number of electrons leave the cluster volume V due to outer ionization, the net electron density becomes $n_\mathrm{e} = n_\mathrm{i}(\mathcal{Z} - Q/n_\mathrm{i}V) = n_\mathrm{i}(\mathcal{Z} - Q/N)$ with $N = n_\mathrm{i}V$ as the total number of ions inside V. Differentiating Eq. (1.31) with respect to t and substituting $\mathrm{d}T_\mathrm{i}/\,\mathrm{d}t$ in Eq. (1.36) one obtains

$$M_\mathrm{i} \frac{\mathrm{d}^2 R}{\mathrm{d}t^2} = \frac{3T_{\mathrm{e}0}(\mathcal{Z} - Q/N)}{R} \left(\frac{R_0}{R}\right)^2. \tag{1.37}$$

Equations (1.36) and (1.37) are difficult to solve analytically, since $\mathcal{Z}$, Q and N are in general time-dependent. The analytical solution is possible for constant $\mathcal{Z}$, Q and N. This situation can be realized after a long time when an initial temperature $T_{\mathrm{e}0}$ is established, no more electrons are produced due to inner ionization and outer ionization is saturated. With these approximations one finds the rate of cluster expansion [6] from the equation

$$\frac{1}{2} M_\mathrm{i} \left(\frac{\mathrm{d}R}{\mathrm{d}t}\right)^2 = \frac{3}{2} T_\mathrm{i} = \frac{3}{2} T_{\mathrm{e}0} \left(\mathcal{Z} - Q/N\right) \left[1 - \left(R_0/R\right)^2\right]. \tag{1.38}$$

Here it is assumed that $\mathrm{d}R/\,\mathrm{d}t = 0$ at the initial time $t = 0$. Equations (1.34) and (1.38) give T_e and T_i as the cluster expands. In the limit of infinite expansion, i.e., $R \to \infty$, the temperature of the ion fluid becomes maximum $T_\mathrm{max} = T_{\mathrm{e}0}\left(\mathcal{Z} - Q/N\right)$ while the electron fluid looses all of its thermal energy and T_e drops to zero. In this limit the ion fluid continues to expand with a constant ion acoustic speed $C_\mathrm{s} = \sqrt{3T_\mathrm{max}/M_\mathrm{i}}$. The solution of Eq. (1.38) is [6]

$$R(t) = R_0 \sqrt{1 + C_\mathrm{s}^2 t^2 / R_0^2}. \tag{1.39}$$

We estimate the typical time required for a deuterium cluster to double the radius. Assuming $\mathcal{Z} = 1$, $M_\mathrm{i} = 2 \times 1836\, m_\mathrm{e}$, $T_{\mathrm{e}0} = 100$ eV, $Q/N = 0.5$, $R_0 = 5$ nm one obtains $T_\mathrm{max} = 50$ eV, $C_\mathrm{s} \approx 84956$ m/s and $t \approx 1.0 \times 10^{-13}$ s.

1.5.2 Coulomb expansion

In an ionized cluster, ions experience mutual Coulomb repulsion due to which they are accelerated. The presence of electrons within the cluster lowers the effective positive charge of an ion and slows down the ion motion. In an ideal case, we can assume all electrons being completely removed at the initial time $t_{\rm in}$ and the ionic background being a homogeneously charged sphere of radius $R(t_{\rm in}) = R_0$ and total charge $Q_{\rm p} = N\mathcal{Z}$. As time progresses the ion cloud expands electrostatically, obeying the equation of motion (in atomic units)

$$NM_{\rm i}\frac{{\rm d}^2R}{{\rm d}t^2} = \frac{Q_{\rm p}^2}{R^2}. \tag{1.40}$$

The solution of Eq. (1.40) with the initial conditions $R(t_{\rm in}) = R_0$ and $\dot{R}(t_{\rm in}) = 0$ reads [6]

$$t = t_{\rm in} + \sqrt{\frac{M_{\rm p}R_0^3}{2Q_{\rm p}^2}}\left(\sqrt{p^2-p} + \ln\left(\sqrt{p} + \sqrt{p-1}\right)\right). \tag{1.41}$$

Here, $p = R(t)/R_0$ is the ratio of the expanding radius to the initial radius and $M_{\rm p} = NM_{\rm i}$ is the total mass of the ion sphere. If we assume that the cluster is already ionized at time $t_{\rm in} = 0$, then the time to double the cluster radius (with $p = 2$) is $t = 1.6232\sqrt{M_{\rm i}R_0^3/N\mathcal{Z}^2}$. Assuming the liquid drop model [6] of a cluster one can express $R_0^3 = r_{\rm W}^3 N$ ($r_{\rm W}$ is the Wigner-Seitz radius) and $t = 1.6232\sqrt{M_{\rm i}r_{\rm W}^3/\mathcal{Z}^2}$. For a deuterium cluster (with $\mathcal{Z} = 1$, $M_{\rm i} = 2\times 1836\, m_{\rm e}$ and $r_{\rm W} = 1.7\times 10^{-10}$ m) one obtains $t \approx 13.6\times 10^{-15}$ s. Thus Coulomb expansion of a cluster is much faster than the hydrodynamic expansion which occurs on the picosecond time scale.

1.6 Summary

In this section we have discussed basic models and ideas which are required for the further understanding of the laser cluster interaction. We have omitted the derivation of the theories and kept our discussion short. More details on the subject are discussed in Refs. [4–6].

Chapter 2

Particle-in-cell simulation

The interaction of intense laser radiation with matter creates a hot and dense plasma of solid-like density. Most of the proposed theoretical models of laser-irradiated clusters assume clusters as homogeneously charged spheres of electrons and ions throughout the laser interaction, which is poorly justified. Theoretical models need validation from "first-principles" numerical simulations. We use the particle-in-cell (PIC) simulation technique, considering the electron and ion dynamics in the self-consistent mean field created by the charged particles themselves in addition to the laser field. In this chapter we discuss necessary details of the PIC method. We present a few test results for the validation of the PIC code which has been developed during the course of this thesis work.

Plasma is a collection of a large number of electrons and ions. In a first approximation one can neglect collisions among the plasma particles and – in the case of small clusters in strong laser fields – also magnetic fields. The kinetic simulation of such a non-relativistic, unmagnetized collisionless plasma is based on the Vlasov equation [62, 65]

$$\frac{\partial f_s}{\partial t} + \boldsymbol{v} \cdot \frac{\partial f_s}{\partial \boldsymbol{x}} + \frac{q_s}{m_s} \boldsymbol{E} \cdot \frac{\partial f_s}{\partial \boldsymbol{v}} = 0. \tag{2.1}$$

Here, $f_s\,(t, \boldsymbol{x}, \boldsymbol{v})$ represents the distribution function of the sth species (either electrons or ions), t is time, $\boldsymbol{x}$ and $\boldsymbol{v}$ describe position and velocity of a particle in the phase space $(\boldsymbol{x}, \boldsymbol{v})$, and $\boldsymbol{E}$ is the electric field acting on the particle. To resolve the entire phase space and to propagate f_s is extremely demanding. Therefore such kind of kinetic modelling is usually limited to two or three phase space dimensions.

Equation (2.1) leads to a set of equations of continuity (for density, momentum, energy and heat flux, upon integration over various moments of f_s in the velocity space) which describes plasma as a macroscopic hydrodynamic fluid [60, 62]. Fluid modelling is useful for the understanding of transport properties of plasmas including the transport of mass, momentum, energy flux and heat flux [60, 62]. Fluid modelling sometimes may not reveal finer details of nonlinear interactions between intense laser light and high density plasmas.

In the absence of any external field, plasma electrons and ions interact among themselves by the mutual Coulomb field. The problem then boils down to the study of the dynamics of the plasma particles in the self-consistent Coulomb field. Kinetic modelling of such kind

is commonly known as "particle simulations" which are popular due to their conceptual simplicity, although computationally still expensive.

Standard particle simulation methods [65, 66] are: (i) Particle-Particle (PP) models, (ii) Particle-in-cell (PIC) models and (iii) Particle-Particle-Particle-in-cell (P^3IC) models. The main difference between these models lies in the computation of the interaction among the particles. The superiority of a particle code depends upon the efficiency and accuracy of the field solution as the number of particles N grows from say, thousands to millions. The PP codes treat the forces of interaction (Coulombic in nature) directly and are commonly known as molecular dynamics (MD) codes. In a system of N particles, one particle interacts with the other $N-1$ particles and there are $N(N-1) \simeq N^2$ number of interactions among all particles in each stage of the force computation. Molecular dynamics simulations of clusters consisting of $N > 1000$ atoms are prohibitive due to the N^2-scaling. The PIC method scales $\sim N\log(N)$ and thus increases the computational efficiency. The P^3IC model is a hybrid approach using both PP and PIC concepts [65,66].

In this work we use the PIC simulation method. We apply the dipole approximation since the cluster size (< 50 nm) is typically many times smaller than the skin depth ($\delta \sim c/\omega_p$) and the laser wavelength ($\lambda_l \sim$ 700-1100 nm). A fully electromagnetic PIC code would require the solution of the full set of Maxwell's equation [65] which is essential when one studies propagation phenomena, e.g., in the case of laser-solid interactions and also for the laser-cluster interaction in the relativistic regime of laser intensities $> 10^{18}\mathrm{Wcm}^{-2}$ where the magnetic component of the Lorentz force is no longer negligible since the electron speed approaches the speed of light. In those cases one certainly needs an electromagnetic PIC code [67].

The computational mesh width Δx and the time step Δt in the PIC simulation must be fine enough to resolve the Debye length and plasma frequency, respectively, for a converged solution. There should be a sufficient number of particles in each computational cell (minimum 8-10 particles per cell) to reduce noise and instabilities.

A PIC simulation consists of the steps shown in the Fig. 2.1: (i) computation of the charge density from the positions of particles, (ii) solution of Poisson's equation to obtain the potential and fields at the positions of particles, (iii) solution of the equation of motion of the particles in the combined field of space charge and external laser to obtain new positions and velocities. In a standard PIC simulation [65, 66] the continuous three-dimensional space is discretized by equally spaced grid points. Therefore an interpolation of the charge density on the grid from the positions of the particles is required. Poisson's equation is solved on the grid from which the electric field on the grid is obtained. Finally, interpolation of the field from the grid to the positions of particles is needed in step (ii) above. In the following sections of this chapter we discuss the steps shown in Fig. 2.1.

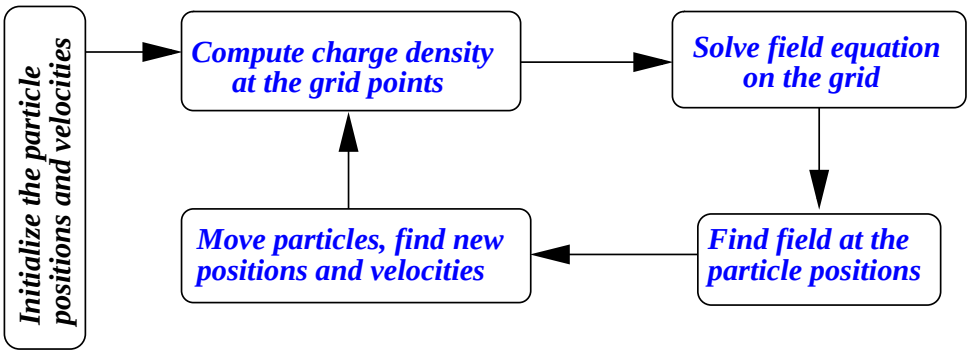

Figure 2.1: Scheme of a particle-in-cell simulation.

2.1 Governing equations

Particle-in-cell simulations are governed by the following set of equations (using atomic units and the dipole approximation)

$$\varrho = \mathcal{Z} n_\mathrm{i} - n_\mathrm{e} \tag{2.2}$$

$$\nabla^2 \phi = -4\pi\varrho \tag{2.3}$$

$$\boldsymbol{E} = -\boldsymbol{\nabla}\phi \tag{2.4}$$

$$\frac{\mathrm{d}\boldsymbol{v}_\mathrm{e}}{\mathrm{d}t} = -\left(\boldsymbol{E} + \boldsymbol{E}_\mathrm{l}\right) \tag{2.5}$$

$$M_\mathrm{i}\frac{\mathrm{d}\boldsymbol{V}_\mathrm{i}}{\mathrm{d}t} = \mathcal{Z}\left(\boldsymbol{E} + \boldsymbol{E}_\mathrm{l}\right) \tag{2.6}$$

$$\frac{\mathrm{d}\boldsymbol{r}_\mathrm{e}}{\mathrm{d}t} = \boldsymbol{v}_\mathrm{e} \tag{2.7}$$

$$\frac{\mathrm{d}\boldsymbol{R}_\mathrm{i}}{\mathrm{d}t} = \boldsymbol{V}_\mathrm{i} \tag{2.8}$$

where n_e is the electron number density, n_i is the number density of ions, $\mathcal{Z}$ is the ion charge, ϱ is the net charge density, ϕ is the electric potential, $\boldsymbol{E}$ is the electric field due to space charge, $\boldsymbol{E}_\mathrm{l}$ is the laser electric field, $\boldsymbol{r}_\mathrm{e}$ and $\boldsymbol{v}_\mathrm{e}$ are position and velocity of a PIC electron, M_i is the ion mass, $\boldsymbol{R}_\mathrm{i}$ and $\boldsymbol{V}_\mathrm{i}$ are the position and the velocity of a PIC ion. Note that one PIC electron or ion may represent several (or a fraction of a) physical electron(s) or ion(s).

2.2 Computation of the charge density

This section describes the computation of the charge density from the coordinates of the particles. We preferred to develop the PIC code in Cartesian coordinates since a laser-irradiated cluster in general does not preserve any symmetry. We divide the simulation volume into a large number of small cubic cells (see Fig. 2.2). Each cell can be identified by integers (j, k, l). One cell corner A with index (j, k, l) has the coordinates $X_j = j\Delta x$,

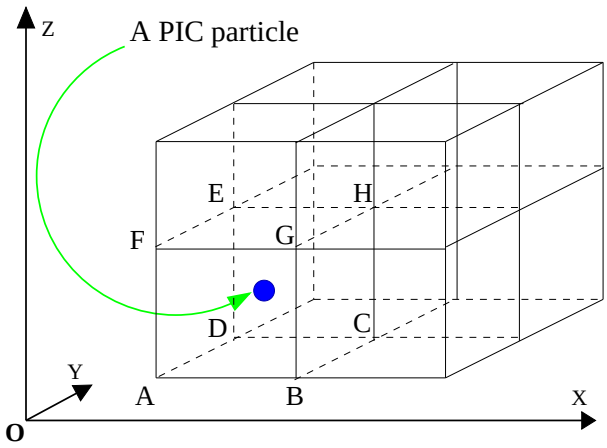

Figure 2.2: The computational grid.

$Y_k = k\Delta y$ and $Z_l = l\Delta z$ with Δx, Δy and Δz the constant grid spacing along X, Y and Z axes such that the volume of each cell is $\Delta V = \Delta x \Delta y \Delta z$. The remaining seven corners B, C, D, E, F, G and H have the coordinates (X_{j+1}, Y_k, Z_l), (X_{j+1}, Y_{k+1}, Z_l), (X_j, Y_{k+1}, Z_l), (X_j, Y_{k+1}, Z_{l+1}), (X_j, Y_k, Z_{l+1}), (X_{j+1}, Y_k, Z_{l+1}) and $(X_{j+1}, Y_{k+1}, Z_{l+1})$, respectively.

Let $\boldsymbol{r}_i(x_i, y_i, z_i, t)$ be the position and $\boldsymbol{v}_i(v_{xi}, v_{yi}, v_{zi}, t)$ be the velocity of the ith PIC particle with respect to the origin (O) of the coordinate system at a given time t. The relative position $\boldsymbol{r}(x, y, z)$ of this particle with respect to the grid point (X_j, Y_k, Z_l) is $x = x_i - X_j$, $y = y_i - Y_k$ and $z = z_i - Z_l$. The relative position $\boldsymbol{r}(x, y, z)$ determines the relative weight of the particle charge density at the grid point (X_j, Y_k, Z_l) and similarly at the other grid points closest to the particle. The noise-level of the PIC simulation depends greatly upon the choice of the interpolation scheme [65, 66] to map the charge density from the particle coordinates to the cell corners.

There are different methods [65, 66] for the particle-to-grid interpolation: (i) Nearest grid point (NGP) weighting, (ii) Particle-in-cell (PIC) or Cloud-in-cell (CIC) weighting and (iii) higher order weighting using quadratic and/or cubic splines. The choice of the interpolation scheme corresponds to different finite shapes of the particles (instead of point like physical particles) [65, 66].

In the NGP method, any particle with position between $X_j \pm \Delta x/2$ is assigned to the grid point X_j. The NGP method is noisy and violates the conservation of energy [65, 66]. Therefore, the NGP scheme is seldom used. In the PIC/CIC method fractions of the particle charge density are assigned to the grid points surrounding the particle. This scheme smoothes out unphysical oscillations of the charge density.

For $X_j \leq x \leq X_{j+1}$, $Y_k \leq y \leq Y_{k+1}$ and $Z_l \leq z \leq Z_{l+1}$, the ith particle lies within the cell (j, k, l) of volume ΔV. The fraction of the charge density at the grid point (j, k, l) is the product $(\Delta x - x)(\Delta y - y)(\Delta z - z)/\Delta x \Delta y \Delta z$ multiplied by the single particle charge density $\eta_i = q_i/\Delta V$ (assuming the charge q_i of the ith particle to uniformly fill the cell volume). The result $\eta_i(\Delta x - x)(\Delta y - y)(\Delta z - z)/\Delta x \Delta y \Delta z$ is then summed up for all computational particles N_c within the cell to obtain the net charge density at the grid

point (j,k,l). Following the above procedure one finds the charge densities at the eight corners of the cell (j,k,l) as

$$\varrho_{j,k,l} = \sum_{i=1}^{Nc} \eta_i \frac{(\Delta x - x)}{\Delta x} \frac{(\Delta y - y)}{\Delta y} \frac{(\Delta z - z)}{\Delta z} \tag{2.9}$$

$$\varrho_{j+1,k,l} = \sum_{i=1}^{Nc} \eta_i \frac{x}{\Delta x} \frac{(\Delta y - y)}{\Delta y} \frac{(\Delta z - z)}{\Delta z} \tag{2.10}$$

$$\varrho_{j+1,k+1,l} = \sum_{i=1}^{Nc} \eta_i \frac{x}{\Delta x} \frac{y}{\Delta y} \frac{(\Delta z - z)}{\Delta z} \tag{2.11}$$

$$\varrho_{j,k+1,l} = \sum_{i=1}^{Nc} \eta_i \frac{(\Delta x - x)}{\Delta x} \frac{y}{\Delta y} \frac{(\Delta z - z)}{\Delta z} \tag{2.12}$$

$$\varrho_{j,k+1,l+1} = \sum_{i=1}^{Nc} \eta_i \frac{(\Delta x - x)}{\Delta x} \frac{y}{\Delta y} \frac{z}{\Delta z} \tag{2.13}$$

$$\varrho_{j,k,l+1} = \sum_{i=1}^{Nc} \eta_i \frac{(\Delta x - x)}{\Delta x} \frac{(\Delta y - y)}{\Delta y} \frac{z}{\Delta z} \tag{2.14}$$

$$\varrho_{j+1,k,l+1} = \sum_{i=1}^{Nc} \eta_i \frac{x}{\Delta x} \frac{(\Delta y - y)}{\Delta y} \frac{z}{\Delta z} \tag{2.15}$$

$$\varrho_{j+1,k+1,l+1} = \sum_{i=1}^{Nc} \eta_i \frac{x}{\Delta x} \frac{y}{\Delta y} \frac{z}{\Delta z}. \tag{2.16}$$

If we take the sum of the charge densities of all eight corners we retrieve η_i, meaning that the charge is locally conserved in the CIC/PIC interpolation scheme. If a charge q_i is placed at the cell center (i.e., $\Delta x - x = \Delta x/2$, $\Delta y - y = \Delta y/2$ and $\Delta z - z = \Delta z/2$) the charge is shared equally among the respective grid points surrounding the particle. η_i is constant for particles of equal charge (e.g., electrons), but particles of different charges (e.g., ions of different charge states) yield different values of η_i. After obtaining the charge density at all grid points, the electric potential can be calculated.

2.3 Solution of Poisson's equation

The computation of the electric field from the charge density requires the solution of Poisson's equation (2.3). The boundary conditions need to be specified. Relevant possibilities are: periodic boundary conditions, Dirichlet boundary conditions or Neumann boundary conditions. A meaningful combination of the above boundary conditions may also be applied, depending upon the physical situation. In the context of laser cluster interaction, periodic boundary conditions are of interest when individual clusters are considered at regular intervals. For an isolated cluster either Dirichlet or Neumann boundary conditions may be applicable.

An efficient solution of the three-dimensional Poisson equation (2.3) is non-trivial. Various methods for solving Poisson's equation have been extensively reviewed in Ref. [66]. This section describes the methods using the fast Fourier transformation (FFT) for solving Poisson's equation with all kinds of boundary conditions.

2.3.1 Fourier transform methods

To solve Poisson's equation (2.3) we consider its finite difference approximation. The central difference approximation of the Poisson equation (2.3) can be written as [68]

$$\frac{\phi(j+1,k,l)-2\phi(j,k,l)+\phi(j-1,k,l)}{(\Delta x)^2}+\frac{\phi(j,k+1,l)-2\phi(j,k,l)+\phi(j,k-1,l)}{(\Delta y)^2} + \frac{\phi(j,k,l+1)-2\phi(j,k,l)+\phi(j,k,l-1)}{(\Delta z)^2}=-\varrho_{jkl}. \quad (2.17)$$

We have absorbed 4π [of Eq. (2.3)] within ϱ_{jkl}. The discrete Fourier transform (DFT) of the three-dimensional charge density ϱ_{jkl} reads [68]

$$\hat{\varrho}_{pqr}=\sum_{j=0}^{J-1}\sum_{k=0}^{K-1}\sum_{l=0}^{L-1}\varrho_{jkl}\exp\left(\frac{2\pi \mathrm{i}pj}{J}\right)\exp\left(\frac{2\pi \mathrm{i}qk}{K}\right)\exp\left(\frac{2\pi \mathrm{i}rl}{L}\right), \quad (2.18)$$

where J, K and L are the number of grid points along the x, y and z-directions respectively. $\hat{\varrho}_{pqr}$ is the inverse Fourier transform (IFT) of ϱ_{jkl} which can be retrieved by the transformation

$$\varrho_{jkl}=\frac{8}{JKL}\sum_{p=0}^{J-1}\sum_{q=0}^{K-1}\sum_{r=0}^{L-1}\hat{\varrho}_{pqr}\exp\left(\frac{-2\pi \mathrm{i}pj}{J}\right)\exp\left(\frac{-2\pi \mathrm{i}qk}{K}\right)\exp\left(\frac{-2\pi \mathrm{i}rl}{L}\right), \quad (2.19)$$

with $8/(JKL)$ as the normalization factor. Analogous expressions similar to Eqns. (2.18)–(2.19) also hold for the potential $\phi_{jkl} \equiv \phi(j,k,l)$ and its inverse transform $\hat{\phi}_{pqr}$ which can be expressed as

$$\hat{\phi}_{pqr}=\sum_{j=0}^{J-1}\sum_{k=0}^{K-1}\sum_{l=0}^{L-1}\phi_{jkl}\exp\left(\frac{2\pi \mathrm{i}pj}{J}\right)\exp\left(\frac{2\pi \mathrm{i}qk}{K}\right)\exp\left(\frac{2\pi \mathrm{i}rl}{L}\right), \quad (2.20)$$

$$\phi_{jkl}=\frac{8}{JKL}\sum_{p=0}^{J-1}\sum_{q=0}^{K-1}\sum_{r=0}^{L-1}\hat{\phi}_{pqr}\exp\left(\frac{-2\pi \mathrm{i}pj}{J}\right)\exp\left(\frac{-2\pi \mathrm{i}qk}{K}\right)\exp\left(\frac{-2\pi \mathrm{i}rl}{L}\right). \quad (2.21)$$

Substituting ϱ_{jkl} and ϕ_{jkl} in Eq. (2.17) we obtain [68]

$$\hat{\phi}_{pqr}=-\frac{\hat{\varrho}_{pqr}\Delta^2}{2\left[\cos\left(\frac{2\pi p}{J}\right)+\cos\left(\frac{2\pi q}{K}\right)+\cos\left(\frac{2\pi r}{L}\right)-3\right]}, \quad (2.22)$$

assuming equal grid spacing $\Delta x = \Delta y = \Delta z = \Delta$ along the x, y and z directions. Equation (2.22) relates the potential with the charge density in Fourier space. The full solution of Poisson's equation can be obtained after taking the inverse transform of Eq. (2.22). However, Eq. (2.22) is valid only for periodic boundary conditions. The periodic boundary conditions are naturally included in Eq. (2.22) due to the periodicity of the exponents in the transforms.

2.3.2 Neumann boundary conditions

For the Neumann boundary condition one specifies the electric field $-\boldsymbol{\nabla}\phi$ at the boundary. If the electric field vanishes at the boundary, the boundary conditions are naturally satisfied by the cosine transform (COSFFT) and the inverse cosine transforms (ICOSFFT). The COSFFT and ICOSFFT of the charge density can be written as

$$\hat{\varrho}_{pqr} = \sum_{j=0}^{J}\sum_{k=0}^{K}\sum_{l=0}^{L} \varrho_{jkl} \cos\left(\frac{\pi p j}{J}\right) \cos\left(\frac{\pi q k}{K}\right) \cos\left(\frac{\pi r l}{L}\right), \tag{2.23}$$

$$\varrho_{jkl} = \frac{8}{JKL}\sum_{p=0}^{J}\sum_{q=0}^{K}\sum_{r=0}^{L} \hat{\varrho}_{pqr} \cos\left(\frac{\pi p j}{J}\right) \cos\left(\frac{\pi q k}{K}\right) \cos\left(\frac{\pi r l}{L}\right). \tag{2.24}$$

Analogous equations for the potential are given by

$$\hat{\phi}_{pqr} = \sum_{j=0}^{J}\sum_{k=0}^{K}\sum_{l=0}^{L} \phi_{jkl} \cos\left(\frac{\pi p j}{J}\right) \cos\left(\frac{\pi q k}{K}\right) \cos\left(\frac{\pi r l}{L}\right), \tag{2.25}$$

$$\phi_{jkl} = \frac{8}{JKL}\sum_{p=0}^{J}\sum_{q=0}^{K}\sum_{r=0}^{L} \hat{\phi}_{pqr} \cos\left(\frac{\pi p j}{J}\right) \cos\left(\frac{\pi q k}{K}\right) \cos\left(\frac{\pi r l}{L}\right). \tag{2.26}$$

Substituting ϱ_{jkl} and ϕ_{jkl} from Eqns. (2.24) and (2.26) in Eq. (2.17) we obtain

$$\hat{\phi}_{pqr} = -\frac{\hat{\varrho}_{pqr}\Delta^2}{2\left[\cos\left(\frac{\pi p}{J}\right) + \cos\left(\frac{\pi q}{K}\right) + \cos\left(\frac{\pi r}{L}\right) - 3\right]}. \tag{2.27}$$

Equation (2.27) can be inverted to obtain the solution of the Poisson equation.

2.3.3 Dirichlet boundary conditions

Dirichlet boundary conditions require the potential ϕ at the boundary. If the potential vanishes at the boundary, the boundary conditions are naturally satisfied by the sine transform (SINFFT) and the inverse sine transforms (ISINFFT) of the potential (charge density). The SINFFT and ISINFFT of the charge density can be written as

$$\hat{\varrho}_{pqr} = \sum_{j=0}^{J}\sum_{k=0}^{K}\sum_{l=0}^{L} \varrho_{jkl} \sin\left(\frac{\pi p j}{J}\right) \sin\left(\frac{\pi q k}{K}\right) \sin\left(\frac{\pi r l}{L}\right), \tag{2.28}$$

$$\varrho_{jkl} = \frac{8}{JKL}\sum_{p=0}^{J}\sum_{q=0}^{K}\sum_{r=0}^{L} \hat{\varrho}_{pqr} \sin\left(\frac{\pi p j}{J}\right) \sin\left(\frac{\pi q k}{K}\right) \sin\left(\frac{\pi r l}{L}\right). \tag{2.29}$$

Similarly the transformation of the potential obeys

$$\hat{\phi}_{pqr} = \sum_{j=0}^{J}\sum_{k=0}^{K}\sum_{l=0}^{L} \phi_{jkl} \sin\left(\frac{\pi p j}{J}\right) \sin\left(\frac{\pi q k}{K}\right) \sin\left(\frac{\pi r l}{L}\right), \tag{2.30}$$

$$\phi_{jkl} = \frac{8}{JKL}\sum_{p=0}^{J}\sum_{q=0}^{K}\sum_{r=0}^{L} \hat{\phi}_{pqr} \sin\left(\frac{\pi p j}{J}\right) \sin\left(\frac{\pi q k}{K}\right) \sin\left(\frac{\pi r l}{L}\right). \tag{2.31}$$

Substituting ϱ_{jkl} and ϕ_{jkl} from Eqns. (2.29) and (2.31) in Eq. (2.17) we obtain

$$\hat{\phi}_{pqr} = -\frac{\hat{\varrho}_{pqr}\Delta^2}{2\left[\cos\left(\frac{\pi p}{J}\right) + \cos\left(\frac{\pi q}{K}\right) + \cos\left(\frac{\pi r}{L}\right) - 3\right]}. \tag{2.32}$$

The algebraic Eqns. (2.22), (2.27) and (2.32) relate the charge density with the potential in Fourier space for periodic, Neumann and Dirichlet boundary conditions, respectively. The three-dimensional numerical routines SINFFT, ISINFFT, COSFFT and ICOSFFT are based on the one-dimensional FFT routines from the Numerical Recipes [68]. We integrated those routines in a three-dimensional Poisson solver for the various boundary conditions mentioned above.

2.3.4 Test of the Poisson solver

We now present a numerical example to verify the accuracy of the Poisson solver. We consider the Poisson equation $\nabla^2\phi = -\varrho$ with $\varrho = 3\sin x \sin y \sin z$ on a $32 \times 32 \times 32$ grid and assume non-zero Dirichlet boundary conditions $\phi(x, y, \pm\pi/2) = \pm 1$, $\phi(x, \pm\pi/2, z) = \pm 1$ and $\phi(\pm\pi/2, y, z) = \pm 1$. Figure 2.3 shows the excellent agreement of the analytical

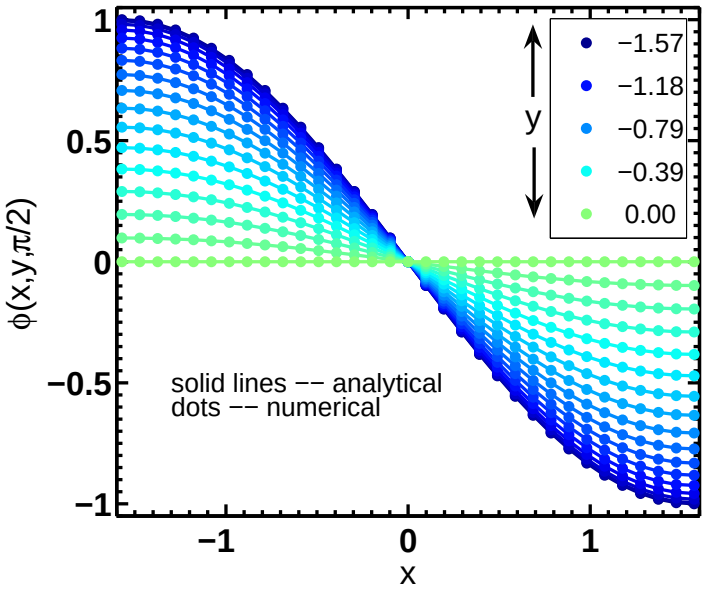

Figure 2.3: Solution of Poisson's equation $\nabla^2\phi = -\varrho$ with $\varrho = 3\sin x \sin y \sin z$ on a $32 \times 32 \times 32$ grid. Dirichlet boundary conditions $\phi(x, y, \pm\pi/2) = \pm 1$, $\phi(x, \pm\pi/2, z) = \pm 1$ and $\phi(\pm\pi/2, y, z) = \pm 1$ are considered. Excellent agreement between the analytical solution $\phi(x, y, z) = \sin x \sin y \sin z$ with the numerical solution is obtained. Different lines correspond to data in different y-planes ($y = -\pi/2$ to 0) for $-\pi/2 \le x \le \pi/2$.

solution $\phi(x, y, z) = \sin x \sin y \sin z$ with the numerical solution. Different lines correspond to the data in different y-planes ($y = -\pi/2$ to 0) as x varies from $-\pi/2$ to $\pi/2$.

2.3.5 Electric field on the grids

After obtaining the potential ϕ from the solution of Poisson's equation the corresponding electric field results from the finite difference representation of the gradient $\boldsymbol{\nabla}\phi$,

$$E^x_{j,k,l} = -\frac{\phi(j+1,k,l) - \phi(j-1,k,l)}{2\Delta x} \tag{2.33}$$

$$E^y_{j,k,l} = -\frac{\phi(j,k+1,l) - \phi(j,k-1,l)}{2\Delta y} \tag{2.34}$$

$$E^z_{j,k,l} = -\frac{\phi(j,k,l+1) - \phi(j,k,l-1)}{2\Delta z}. \tag{2.35}$$

The three-point central difference is erroneous at the boundaries since it requires extrapolation beyond the boundaries. Hence, we use the two-point forward difference (and backward difference) at the boundary points which gives

$$E^x_{j,k,l} = -\frac{\phi(j+1,k,l) - \phi(j,k,l)}{\Delta x} \tag{2.36}$$

$$E^y_{j,k,l} = -\frac{\phi(j,k+1,l) - \phi(j,k,l)}{\Delta y} \tag{2.37}$$

$$E^z_{j,k,l} = -\frac{\phi(j,k,l+1) - \phi(j,k,l)}{\Delta z}. \tag{2.38}$$

The variation of the field along one direction (say along x) at a grid point will also depend on the variation of the field at the neighboring points in the transverse directions (y and z). This is not exhibited in the simple difference schemes above. Such a directional anisotropy in the forces may lead to diffusion of particles [65]. However, we shall find a way to overcome it.

2.4 Field interpolation from the grid to the particle

The accuracy of a PIC code depends on the correct calculation of the forces at the particle positions. Even if one has solved Poisson's equation accurately, the force interpolation may lead to erroneous values due to the directional anisotropy in the difference operator [65]. In one-dimensional PIC simulations it is not a problem. We use an energy conserving scheme where the potential at the position of a particle is obtained by interpolating the potential values from the different grid points surrounding the particle. This can be done reversely to the interpolation of the density from the particles to the grid points (see Sec. 2.2). Then we take the derivative of the potential analytically to obtain the force on the particle. The relative position of the particle at $\boldsymbol{r}(x,y,z)$ within a cell can be obtained by defining variables y_1, y_2 and y_3 as $1 - y_1 = (\Delta x - x)/\Delta x, 1 - y_2 = (\Delta y - y)/\Delta y, 1 - y_3 = (\Delta z - z)/\Delta z$. Their respective derivatives are $y_1' = \mathrm{d}y_1/\,\mathrm{d}x = 1/\Delta x, y_2' = \mathrm{d}y_2/\,\mathrm{d}y = 1/\Delta y, y_3' = \mathrm{d}y_3/\,\mathrm{d}z = 1/\Delta z$. The potential at a particle position is the sum of the weights of the potential at the grid points surrounding the particle, which

we write as

$$\begin{aligned}\phi_{x,y,z} = (1-y_1)(1-y_2)(1-y_3)\ \phi_{j,k,l} \ +\ y_1(1-y_2)(1-y_3)\ \phi_{j+1,k,l} \\ + y_1y_2(1-y_3)\ \phi_{j+1,k+1,l} \ +\ (1-y_1)y_2(1-y_3)\ \phi_{j,k+1,l} \\ + (1-y_1)(1-y_2)y_3\ \phi_{j,k,l+1} \ +\ y_1(1-y_2)y_3\ \phi_{j+1,k,l+1} \\ +y_1y_2y_3\ \phi_{j+1,k+1,l+1} \ +\ (1-y_1)y_2y_3\ \phi_{j,k+1,l+1}.\end{aligned} \tag{2.39}$$

The electric field at the position $\boldsymbol{r}$ of the particle can be obtained by taking the derivative $\boldsymbol{E} \equiv -\boldsymbol{\nabla}\phi$ analytically. The $x-$component $E_x = -\partial\phi/\partial x$ of the electric field reads

$$\begin{aligned}-E_x = \left(-\frac{\mathrm{d}y_1}{\mathrm{d}x}\right)(1-y_2)(1-y_3)\ \phi_{j,k,l} \ +\ \frac{\mathrm{d}y_1}{\mathrm{d}x}(1-y_2)(1-y_3)\ \phi_{j+1,k,l} \\ + \frac{\mathrm{d}y_1}{\mathrm{d}x}y_2(1-y_3)\ \phi_{j+1,k+1,l} \ +\ \left(-\frac{\mathrm{d}y_1}{\mathrm{d}x}\right)y_2(1-y_3)\ \phi_{j,k+1,l} \ + \\ \left(-\frac{\mathrm{d}y_1}{\mathrm{d}x}\right)(1-y_2)y_3\ \phi_{j,k,l+1} \ +\ \frac{\mathrm{d}y_1}{\mathrm{d}x}(1-y_2)y_3\ \phi_{j+1,k,l+1} \\ + \frac{\mathrm{d}y_1}{\mathrm{d}x}y_2y_3\ \phi_{j+1,k+1,l+1} \ +\ \left(-\frac{\mathrm{d}y_1}{\mathrm{d}x}\right)y_2y_3\ \phi_{j,k+1,l+1}.\end{aligned} \tag{2.40}$$

Rearranging the terms and substituting Eq. (2.36) we obtain

$$\begin{aligned}E_x = (1-y_2)(1-y_3)E^x_{j,k,l} \ +\ y_2(1-y_3)E^x_{j,k+1,l} \\ + (1-y_2)y_3E^x_{j,k,l+1} \ +\ y_2y_3E^x_{j,k+1,l+1}.\end{aligned} \tag{2.41}$$

Similarly, the y and z components can be found as

$$\begin{aligned}E_y = (1-y_3)(1-y_1)E^y_{j,k,l} \ +\ y_1(1-y_3)E^y_{j+1,k,l} \\ + (1-y_1)y_3E^y_{j,k,l+1} \ +\ y_1y_3E^y_{j+1,k,l+1},\end{aligned} \tag{2.42}$$

$$\begin{aligned}E_z = (1-y_1)(1-y_2)E^z_{j,k,l} \ +\ y_1(1-y_2)E^z_{j+1,k,l} \\ + (1-y_1)y_2E^z_{j,k+1,l} \ +\ y_1y_2E^z_{j+1,k+1,l}.\end{aligned} \tag{2.43}$$

The field components E_x, E_y and E_z are now free from directional anisotropy.

2.5 Solution of the equation of motion

The motion of a charged particle in the combined field of laser and space charge is discussed now. In principle any method for solving a system of ordinary differential equations [65,66] is applicable as a particle mover. We use a fourth-order Runge-Kutta method.

2.6 Particle boundary conditions

Boundary conditions of two different types occur in PIC simulations: (i) field boundary conditions and (ii) particle boundary conditions. Field boundary conditions were discussed in connection with Poisson's equation. When a particle reaches the boundary of

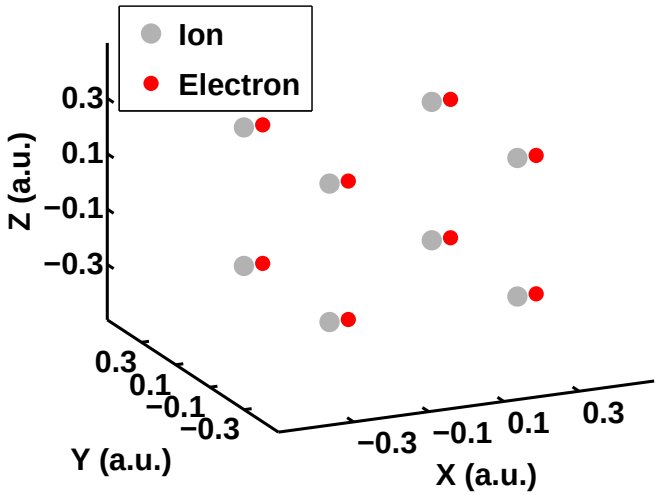

Figure 2.4: Ions and electrons (at time $t = 0$) for the test of the PIC code. Ions are assumed infinitely heavy and at rest. There are eight electrons and ions. Each ionic PIC particle has a charge and mass $q, m = 0.00258478$ a.u. The X-coordinates of the ions are $(-0.25$ and $+0.25)$. Each electron is displaced by $a = 0.05$ a.u. along the $+x$-direction.

the simulation box different situations may arise. It may be sent back (reflecting boundary conditions), it may re-enter from the opposite side of the simulation box (periodic boundary conditions) or it may be removed as soon as it crosses the boundary (absorbing boundaries) leaving the plasma non-neutral. Depending upon the physical situation our PIC code is capable of handling all the particle boundary conditions mentioned above.

2.7 Test of the PIC code

After rigorous testing and verification of each and every part/subroutines (mentioned in the previous sections) we have incorporated them into a full three-dimensional PIC code. In this section, we report the validation of the PIC code with simple examples so that the results can be compared to analytical solutions.

2.7.1 Reproducing the plasma frequency

We assume immobile ions which are located at regular distances in a three dimensional grid as shown in Fig. 2.4. All electrons are given a small perturbation in $+x$-direction at time $t = 0$. The electron-ion system is macroscopically charge neutral. The local charge imbalance will lead to oscillations of the electrons with the plasma frequency determined by the density of the ionic background. An essential verification of any PIC-code is to obtain the correct plasma frequency under small perturbations. Under such conditions the total energy and momentum of the system must be conserved.

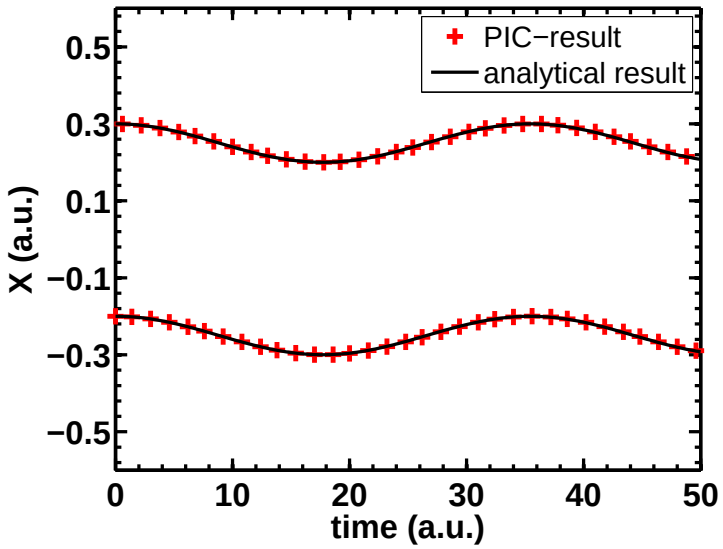

Figure 2.5: Oscillation of electrons with the plasma frequency. Initial positions of the particles are shown in Fig. 2.4. The ionic charge density is $\rho = 0.0025$ corresponding to the plasma frequency $\omega_\mathrm{p} = \sqrt{4\pi\rho} = 0.1772$. The amplitude of oscillation is $a = 0.05$. The charge and mass of each PIC electron is $q = m = 0.00258478$. The excursions $x(t)$ as calculated with the PIC-code matches the analytical result $x(t) = x(0) \pm a\cos(\omega_\mathrm{p} t)$.

The ions are placed at successive grid points (0.5 a.u. apart) with the electrons perturbed by a small amount ($a = 0.05$ a.u.) along the $+x$-direction. Each ionic PIC particle has a charge q and mass m equal to 0.00258478 a.u. We choose an ionic charge density $\rho = 0.0025$ a.u., corresponding to the plasma frequency $\omega_\mathrm{p} = \sqrt{4\pi\rho} = 0.1772$ a.u. The analytical solution for the excursions of the electrons are $x(t) = x(0) \pm a\cos(\omega_\mathrm{p} t)$. Figure 2.5 shows that the excursions $x(t)$ as calculated with the PIC-code matches the analytical result.

2.7.2 Energy conservation

The total analytical kinetic energy K_a of the $N = 8$ electrons in Fig. 2.4 is

$$K_a = \frac{1}{2} m N \dot{x}^2 = \frac{1}{2} m N a^2 \omega_\mathrm{p}^2 \sin^2(\omega_\mathrm{p} t). \tag{2.44}$$

For small displacements of the electrons the force acting on them can be considered proportional to their distances from their parent ions. The total analytical potential energy of all electrons thus is

$$V_a = \frac{1}{2} m N \omega_\mathrm{p}^2 x^2 = \frac{1}{2} m N a^2 \omega_\mathrm{p}^2 \cos^2(\omega_\mathrm{p} t). \tag{2.45}$$

and the total energy reads

$$T_a = K_a + V_a = \frac{1}{2} m N a^2 \omega_\mathrm{p}^2 = \text{const.} \tag{2.46}$$

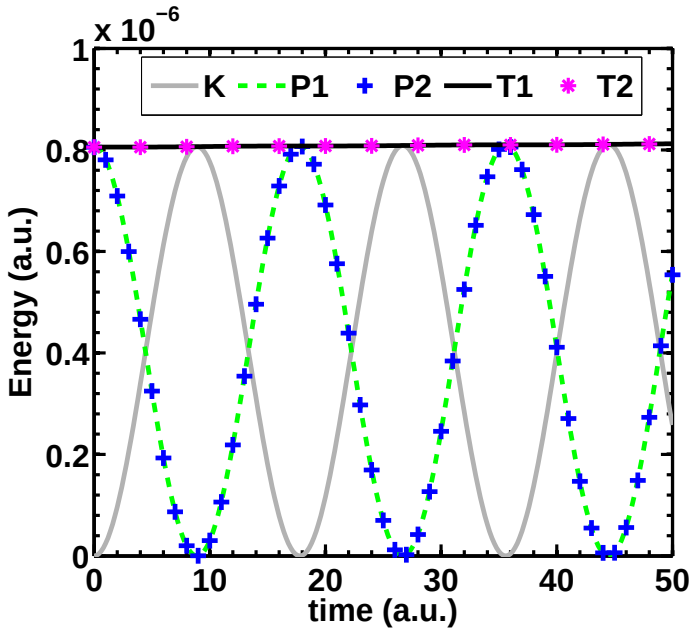

Figure 2.6: Energy test of the PIC code. Kinetic energy K, potential energy P1=$\int E^2\,\mathrm{d}\tau/8\pi$ and P2=$\int \varrho\phi\,\mathrm{d}\tau/2$ vary so that total energy T1 = P1 + K and T2 = P2 + K is conserved.

Figure 2.6 shows the PIC results for kinetic, potential and total energy of the system vs time. In the PIC simulation we compute the potential energy in two different ways. In the first method (P1) we use the definition PE = $\int E^2\,\mathrm{d}\tau/8\pi$, with E being the space charge field and $\mathrm{d}\tau$ being the cell volume. In this case, we first calculate the electric field after the solution of Poisson's equation and then integrate $\int E^2\,\mathrm{d}\tau/8\pi$ numerically over all grid points. In another method (P2), we compute the potential energy PE = $\int \varrho\phi\,\mathrm{d}\tau/2$ without computing the electric field. According to electrostatics these two definitions of the electrostatic energy are equivalent. Numerically they can be different due to the finite difference approximation. Figure 2.6 shows excellent agreement between the two methods.

2.8 Summary

In summary, we have developed a three-dimensional particle-in-cell simulation code to study the interaction of laser light with cluster nanoplasmas. The code development was *essential* to obtain the results presented in this thesis. The validity of the PIC code was illustrated with simple examples for which analytical solutions exist. The fast Fourier transform-based three-dimensional Poisson-solver (with different boundary conditions) may also be useful in other branches of physics.

Chapter 3

Collisionless energy absorption by clusters in short laser pulses

Intense laser-matter interaction provides a route to create energetic particles (e.g., electrons, ions, and photons) using table-top equipment. Clusters, possessing the transparency of gas targets and the high charge density of solid targets, proved to be very efficient absorbers of laser light. Their small size, compared to laser wavelength and skin depth, avoids reflection of the laser beam at the cluster surface as well as the loss of hot electrons into the cold bulk. In fact, almost 100% absorption of the laser light was reported in experiments with rare-gas clusters [7].

Upon irradiation of the rare-gas clusters with intense laser light, electrons first absorb energy and leave their "parent" ions. This is known as inner ionization, meaning that the electrons are still bound to the cluster but not necessarily to their "parent" ions. The total electric field (i.e., laser plus space charge field) inside the cluster leads to inner ionization up to high charge states not possible with the laser field alone (ionization ignition [11,12]). As the laser intensity during the pulse increases, these electrons absorb energy from the laser field and may leave the cluster, leading to the positive charging of the cluster known as outer ionization. Thus outer ionization leads to a non-neutral plasma. With the increasing outer ionization, the restoring force of the ions counteracts ionization ignition so that the latter stops at some point. The net positive charge left behind finally explodes due to the Coulomb repulsion and hydrodynamic pressure, leading to the conversion of electron energy into ion energy. Typically MeV ions and keV electrons [8–10] are measured in experiments.

It is clear from the described scenario that the understanding of the relevant mechanism(s) of laser energy absorption leading to the heating of cluster electrons and outer ionization is of great importance for the development of a complete theoretical description.

Laser energy absorption by electrons proceeds either through resonances (linear or nonlinear) or through non-adiabaticities (all possible types of collisions). All of these processes lead to dephasing of the current density with respect to the laser field, which, according to Poynting's theorem, is a prerequisite for absorption. Collisional absorption via collisions of electrons with ions are of minor importance at near infrared wavelengths

$\simeq 800\,\mathrm{nm}$ or greater [13–16] whereas it is the dominant absorption mechanism at short wavelengths [16–18], not studied in this chapter. The finite size of the clusters suggests that "collisions with the cluster boundary" may be responsible [14] for the energy absorption. However, this viewpoint is misleading, as will be shown in Sec. 3.1.3.

During the expansion of the ionic core, the decreasing charge density $\rho(t)$ leads to the decrease of the Mie-plasma frequency, $\omega_{\mathrm{Mie}}(t) \equiv \sqrt{4\pi\rho(t)/3}$. For very short near infrared laser pulses $\omega_{\mathrm{Mie}}(t)$ cannot meet the linear resonance

$$\omega_{\mathrm{Mie}}(t) = \omega_{\mathrm{l}}, \tag{3.1}$$

unless the cluster has sufficiently expanded (typically after a few hundred femtoseconds). Linear resonance (3.1), well understood in theory, experiments, and simulations [19–27], is thus ruled out for very short pulses or during the early cycles of a long pulse laser-cluster interaction where ion motion is negligible. In this case, nonlinear resonance (NLR), whose origin lies in the anharmonicity of the cluster potential, turns out to be the dominant collisionless absorption mechanism. In fact, for very short linearly polarized (LP) laser pulses, it was clearly shown [69, 70] that essentially *all* electrons that contribute to outer ionization pass through the NLR, which was unequivocally identified as *the* collisionless absorption mechanism in the absence of linear resonance. The eigenfrequency $\omega[\hat{\boldsymbol{r}}(t)]$ of a (laser-) driven oscillator in an anharmonic potential, being dependent on its excursion amplitude $\hat{\boldsymbol{r}}(t)$ (or the energy), may dynamically meet the NLR

$$\omega[\hat{\boldsymbol{r}}(t)] = \omega_{\mathrm{l}}. \tag{3.2}$$

Due to the many-body nature of the interaction, the identification, the separation, and the interpretation of the absorption mechanisms in molecular dynamics or particle-in-cell (PIC) simulations are often difficult. Recently, a method of identification of the NLR in many-body simulations of rare-gas clusters has been proposed [69, 70]. The possible importance of NLR was also mentioned or discussed previously [28–33].

The rigid sphere model (RSM) [30, 31, 34, 35] where electrons and ions are modelled by homogeneously charged rigid spheres oscillating against each other is clearly an oversimplification of a real many-particle system such as a cluster. However, it proves useful for estimating the order of magnitude of the absorbed energy as well as for the calculation of the laser intensity where energy absorption is most efficient, as will be shown in the present work. Moreover, it provides physical understanding and clearly displays NLR [30, 31, 69, 70].

The heating of cluster electrons in circularly polarized laser fields has not yet received much attention, at least theoretically. Experiments with rare-gas clusters show almost no effect on the x-ray emission [36–38] and ion energy distribution [39] when laser light of different ellipticity is used. Theoretically, circular polarization is particularly interesting because the above mentioned "collisions with the cluster boundary" are strongly suppressed in this case. Hence one may expect energy absorption being less efficient. NLR, on the other hand, occurs in both cases, and, in fact, the energy absorption turns out to be equally efficient. To model the electron dynamics in a circularly polarized laser field we extend the RSM to two dimensions. In the rigid-sphere model, the absorbed

energy increases by many orders of magnitude at a certain threshold laser intensity. The particle-in-cell results display maximum fractional absorption around the same intensity. We calculate the threshold intensity and show that it is underestimated by the common over-barrier ionization estimate.

The outline of the present chapter is as follows: in Sec. 3.1.1 we briefly review the NLR and the RSM. In Sec. 3.1.2 the perturbative solution of the RSM is presented. In Sec. 3.1.3 the RSM is extended to circular polarization, where NLR is observed as well. In Sec. 3.1.4 the RSM threshold intensities are calculated. Section 3.2 is devoted to the PIC [65] results for both linear and circular polarization. Finally, we summarize our results in Sec. 3.3.

Throughout this chapter we use $n = 8$-cycle laser pulses of near infrared wavelength $\lambda = 1056\,\mathrm{nm}$ and a fixed cluster radius $R = 3.2\,\mathrm{nm}$ unless stated otherwise. NLR is a robust phenomenon that—qualitatively—is insensitive to cluster and laser parameters.

3.1 Nonlinear resonance in the rigid sphere model

The ion motion can be neglected in the study of energy absorption in very short laser pulses. Thus the ions just form a static, positively charged background of spherical shape. For not too high laser intensity, the collective motion of the electrons can also be approximated by a homogeneous, rigid sphere of negative charge. In the simplest case the radii of ion and electron sphere are assumed to be equal. In a more realistic model the electron cloud expands [30]. However, the method of identification of the NLR used in this work is independent of the degree of electronic expansion. The center of mass of the electron-ion system is, in good approximation, located at the center of the ion sphere. In an oscillating laser field, the homogeneously charged electron sphere oscillates back and forth against the positively charged ion sphere.

3.1.1 NLR in a linearly polarized laser field

We recall the equation motion (from chapter 1) of the electron center of mass in a LP laser field, polarized along x, and rewrite it as

$$\frac{\mathrm{d}^2\bar{r}}{\mathrm{d}\tau^2} + \frac{\bar{r}}{r}g(r) = -\frac{E_\mathrm{l}(\tau)}{R\omega_\mathrm{l}^2}, \tag{3.3}$$

where $\bar{r} = x/R$ is the excursion of the electron sphere, normalized to the cluster radius R, $r = |\bar{r}|$, $\tau = \omega_\mathrm{l} t$ is the normalized time, and the force $g(r)$ is

$$g(r) = \left(\frac{\omega_\mathrm{Mie}}{\omega_\mathrm{l}}\right)^2 \times \begin{cases} r - \frac{9r^2}{16} + \frac{r^4}{32} & 0 \le r \le 2 \\ \frac{1}{r^2} & r \ge 2. \end{cases} \tag{3.4}$$

The nonlinear terms in the upper line of $g(r)$ arise because of the partial overlap of electron and ion sphere. The force is purely Coulombic (the r^{-2} term in the lower line of $g(r)$) if electron and ion sphere are separated. In an earlier work [30] it was shown

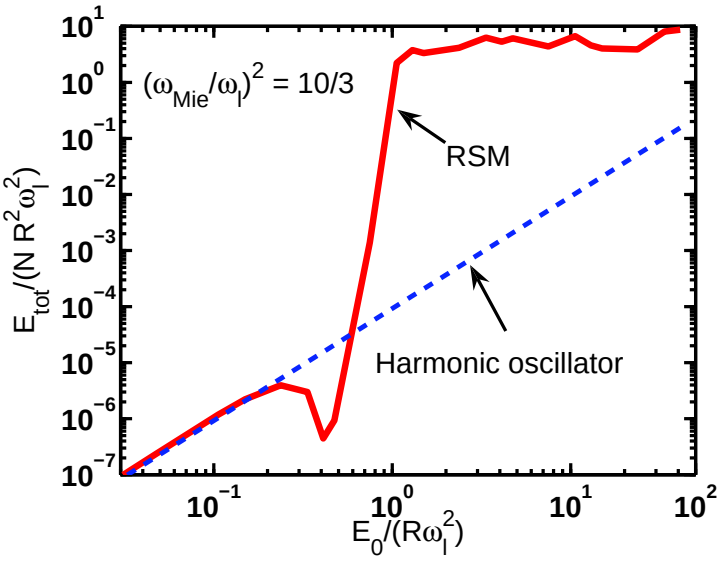

Figure 3.1: Laser energy absorption vs driver amplitude in the rigid sphere-model for $(\omega_{\rm Mie}/\omega_{\rm l})^2 = 10/3$, an $n = 8$ cycle laser field $E_{\rm l}(\tau) = E_0 \sin^2(\tau/2n)\cos(\tau)$, and cluster radius $R = 3.2$ nm. Within a narrow field strength interval (here $\simeq 0.5$–1) the absorbed energy per particle (solid line) increases by many orders of magnitude. The dashed line represents the absorbed energy (3.7) by a purely harmonic oscillator driven by the same laser field.

that absorption of laser energy in the RSM is characterized by a threshold driver strength below which absorption is negligible (harmonic regime) and above which absorption is almost constant. Figure 3.1 shows this threshold behavior for $(\omega_{\rm Mie}/\omega_{\rm l})^2 = 10/3$ and an $n = 8$-cycle $\sin^2$-pulse $E_{\rm l}(\tau) = E_0 \sin^2(\tau/2n)\cos(\tau)$ for $0 < \tau < 2n\pi$. The dashed line is the absorption corresponding to a driven, purely harmonic oscillator

$$\frac{{\rm d}^2\bar{r}}{{\rm d}\tau^2} + \left(\frac{\omega_{\rm Mie}}{\omega_{\rm l}}\right)^2 \bar{r} = -\frac{E_{\rm l}(\tau)}{R\omega_{\rm l}^2} \tag{3.5}$$

in the laser field $E_{\rm l}(\tau)$. The laser energy absorbed by a single electron in a n-cycle laser pulse of period T is

$$\frac{E_{\rm tot}}{N} = -\int_0^{nT} \boldsymbol{v}(t)\cdot\boldsymbol{E}_{\rm l}(t)\ {\rm d}t. \tag{3.6}$$

Solving the harmonic oscillator equation (3.5) analytically for the velocity $v(t)$ and integrating (3.6) one finds for the absorbed energy per electron [30]

$$\frac{E_{\rm tot}}{N} \simeq \frac{\omega_{\rm l}^4\omega_{\rm Mie}^2(\omega_{\rm Mie}^2+3\omega_{\rm l}^2)^2}{4n^4(\omega_{\rm Mie}^2-\omega_{\rm l}^2)^6}\left[1-\cos\left(\omega_{\rm Mie}nT\right)\right]E_0^2 \tag{3.7}$$

where $[\omega_{\rm Mie}^2-(1+1/n)^2\omega_{\rm l}^2]^2[\omega_{\rm Mie}^2-(1-1/n)^2\omega_{\rm l}^2]^2 \simeq (\omega_{\rm Mie}^2-\omega_{\rm l}^2)^4$ (for sufficiently large n) was used. The analytical estimate (3.7) is plotted in Fig. 3.1 together with the absorbed energy obtained from the numerical solution of the anharmonic oscillator equation (3.3). One sees that the absorbed energy jumps by many orders of magnitude to a higher value after crossing a threshold driver strength. The higher the cluster charge density is, the higher

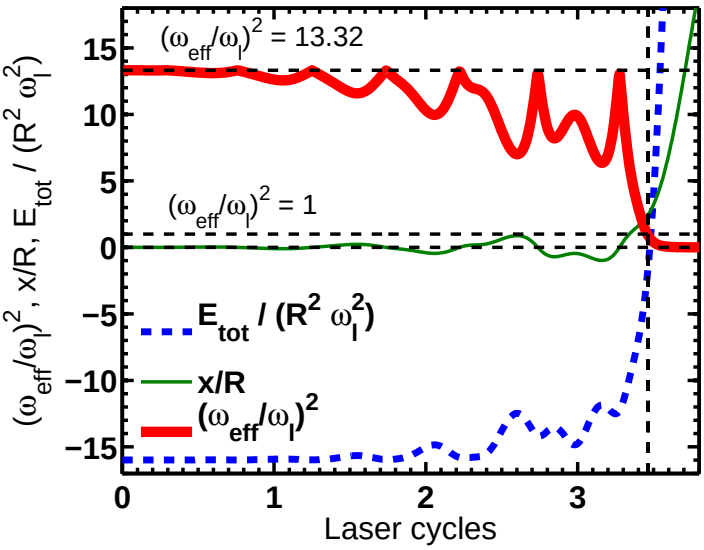

Figure 3.2: Typical behavior of $(\omega_{\rm eff}(\tau)/\omega_{\rm l})^2$ (red, upper solid line) vs laser cycles above the threshold driver strength for $(\omega_{\rm Mie}/\omega_{\rm l})^2 = 40/3$. Here we take $E_0/R\omega_{\rm l}^2 \simeq 7.48$ corresponding to a laser intensity $\simeq 2.5 \times 10^{16}{\rm W/cm^2}$, an $n = 8$-cycle $\sin^2$-pulse $E_{\rm l}(\tau) = E_0 \sin^2(\tau/2n)\cos(\tau)$ of wavelength $\lambda = 1056\,{\rm nm}$, and a cluster radius $R = 3.2\,{\rm nm}$. Excursion x/R (green, middle solid line) and energy of the electron sphere $E_{\rm tot}/R^2\omega_{\rm l}^2$ (blue, lower dashed line) are included in the plot. Outer ionization (i.e., $E_{\rm tot}/R^2\omega_{\rm l}^2 \geq 0$) and occurrence of NLR $[\omega_{\rm eff}(\tau)/\omega_{\rm l}]^2 = 1$ always coincide (dashed vertical line).

is this threshold driver strength. The rigid sphere model shows this behavior of efficient absorption above the threshold driver strength at all cluster charge densities independent of the linear resonance condition $\rho = 3\rho_{\rm c}$, contrary to the nanoplasma model [19]. Since the rigid sphere model does not necessarily require expansion of the cluster for the efficient absorption of laser energy, it permits us to understand the behavior of energy absorption and the underlying mechanism for very short laser pulses.

Equation (3.3) can be formally rewritten as

$$\frac{{\rm d}^2\bar{r}}{{\rm d}\tau^2} + \left[\frac{\omega_{\rm eff}[\hat{r}(\tau)]}{\omega_{\rm l}}\right]^2 \bar{r} = -\frac{E_{\rm l}(\tau)}{R\omega_{\rm l}^2}. \tag{3.8}$$

Equation (3.8) yields the instantaneous, scaled effective frequency squared

$$\left[\frac{\omega_{\rm eff}(\tau)}{\omega_{\rm l}}\right]^2 = \frac{-\frac{E_{\rm l}(\tau)}{R\omega_{\rm l}^2} - \ddot{\bar{r}}(\tau)}{\bar{r}(\tau)} = \frac{g[r(\tau)]}{r(\tau)} \tag{3.9}$$

which passes through unity at the NLR (3.2). The right hand side of (3.9) is the restoring force divided by the excursion of the electronic cloud, which in the case of harmonic motion would be the square of the characteristic frequency. Figure 3.2 shows a typical example of the temporal behavior of $[\omega_{\rm eff}(\tau)/\omega_{\rm l}]^2$ above the threshold driver strength for $(\omega_{\rm Mie}/\omega_{\rm l})^2 = 40/3$. Since $(\omega_{\rm Mie}/\omega_{\rm l})^2 = 13.32$, $[\omega_{\rm eff}(\tau)/\omega_{\rm l}]^2$ starts at this value and drops with increasing driver strength. It passes through unity at the time indicated

by the vertical line, and it is exactly at that time where the electron sphere becomes free (outer ionization). This incidence is clearly visible from the energy of the electron sphere, which passes through zero, and the strongly increasing excursion. Outer ionization and occurrence of NLR happens for all driver strengths above the threshold whereas the resonance is never met below the threshold. Since the amplitude of the excursion of the electronic sphere depends upon the driver strength, the excursion amplitude should also be large enough so that the NLR is passed. The decrease in the effective frequency with the increase of the amplitude of excursion of the electronic sphere in the force field (3.3) can be understood by analyzing its motion in the corresponding anharmonic potential

$$V(r) = {\omega_{\rm Mie}}^2 R^2 \times \begin{cases} \frac{r^2}{2} - \frac{3r^3}{16} + \frac{r^5}{160} & 0 \le r \le 2 \\ \frac{6}{5} - \frac{1}{r} & r \ge 2. \end{cases} \tag{3.10}$$

The period T of oscillation of the electronic sphere in the potential $V(r)$ can be approximated by a perturbation series [71] as

$$T = \frac{1}{\sqrt{2}} \sum_{k=0}^{\infty} \frac{(-1)^k}{k!} \frac{\partial^k}{\partial E_{\rm tot}^k} \oint \frac{[\delta V(r)]^k \, {\rm d}r}{\sqrt{E_{\rm tot} - V_0(r)}}. \tag{3.11}$$

$V_0(r) = \omega_{\rm Mie}^2 R^2 r^2/2$ is the harmonic oscillator potential and $\delta V(r) = \alpha R^3 r^3/3 + \beta R^5 r^5/5$ is the perturbation to the potential with $\alpha = -9\omega_{\rm Mie}^2/16R$ and $\beta = \omega_{\rm Mie}^2/32R^3$. The effective frequency is then $\omega_{\rm eff} = 2\pi/T$. For the excursion $r < 2$ and cluster radius $R = 3.2\,{\rm nm}$ ($\simeq 60.4\,{\rm a.u.}$) we can consider $|\beta/\alpha| \ll 1$ and the approximate potential $\delta V(r) \simeq \alpha R^3 r^3/3$. Corrections up to $k = 6$ yield $T = T_0 + T_1 + \cdots + T_6$. The unperturbed period is $T_0 = 2\pi/\omega_{\rm Mie}$ and the successive corrections are $T_1 = c_1/(3\omega_{\rm Mie}^4)$, $T_2 = c_2/(3\omega_{\rm Mie}^7)$, $T_3 = c_3/(9\omega_{\rm Mie}^{10})$, $T_4 = c_4/(72\omega_{\rm Mie}^{13})$, $T_5 = c_5/(54\omega_{\rm Mie}^{16})$, $T_6 = c_6/(3^6\omega_{\rm Mie}^{19})$ with $c_1 \simeq -8\alpha(2E_{\rm tot})^{1/2}$, $c_2 \simeq 5\pi\alpha^2 E_{\rm tot}$, $c_3 \simeq -28.45\alpha^3(2E_{\rm tot})^{3/2}$, $c_4 \simeq 385\pi\alpha^4 E_{\rm tot}^2$, $c_5 \simeq -318.6\alpha^5(2E_{\rm tot})^{5/2}$ and $c_6 \simeq 97.89 \times 2^9\alpha^6 E_{\rm tot}^3$, respectively.

Neglecting the higher order term of $g(r)$ for $r < 2$, a simpler approximation to the effective frequency can be derived from (3.9) by replacing the excursion r with the excursion amplitude $\hat{r}$:

$$\omega_{\rm eff}(\hat{r}) \simeq \omega_{\rm Mie}\,(1 - 9\hat{r}/16)^{1/2} \simeq \omega_{\rm Mie}\,(1 - 9\hat{r}/32)\,. \tag{3.12}$$

Figure 3.3 shows the effective frequency vs the excursion amplitude $\hat{r}$ of the electronic sphere in the potential (3.10) for various cluster charge densities $\rho/\rho_{\rm c} = 10$–40 as calculated from the numerical solution of (3.3) together with the approximations (3.11) and (3.12). The effective frequency as calculated from (3.11) shows good agreement below the excursion $\hat{r} < 1.5$ and low charge densities (e.g., $\rho/\rho_{\rm c} < 10$). For higher charge densities more corrections [large number of k values in (3.11)] are needed, which are very much cumbersome to calculate. Although (3.12) fits well with the numerical solution, $\omega_{\rm eff}$ becomes negative when $\hat{r} > 32/9$. However, the results using (3.12) agree with the exact ones in Fig. 3.3 up to $\rho/\rho_{\rm c} = 30$ for the excursions of interest, i.e., up to the point where the electronic sphere undergoes NLR. The variation of frequency with the excursion amplitude as shown in Fig. 3.3 explains why a threshold driver strength is required for an appreciable laser energy absorption as well as for the crossing of the NLR in Fig. 3.2: only a driver exceeding a certain threshold field strength will lead to excursions compatible with the NLR condition $\omega_{\rm eff} = \omega_{\rm l}$.

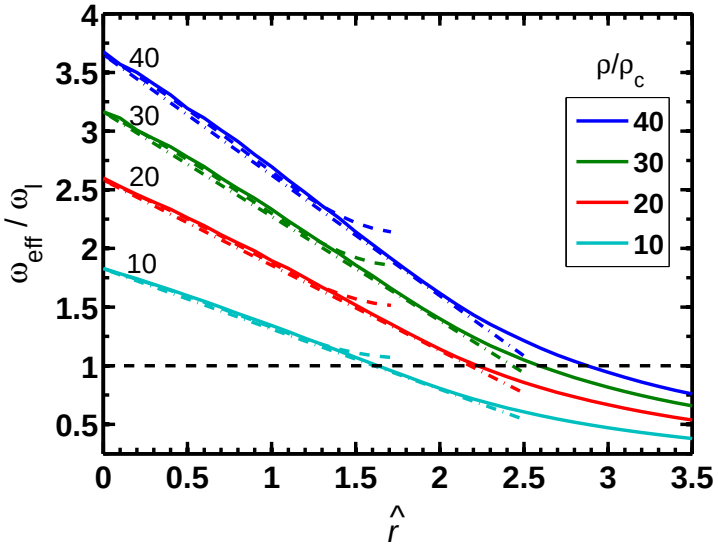

Figure 3.3: Effective frequency $\omega_{\rm eff}/\omega_{\rm l}$ vs the excursion amplitude $\hat{r}$ of the electronic sphere for different cluster charge densities $\rho/\rho_{\rm c} = 10$–40. The solid lines are computed from the numerical solution of (3.3). The dashed lines are the corresponding analytical approximations from (3.11) for k up to 6, and the dashed-dotted lines are from (3.12). For the charge density $\rho/\rho_{\rm c} = 40$ one expects NLR (horizontal dashed line) to occur at the excursion $\hat{r} \simeq 2.88$.

3.1.2 Perturbative solution of the rigid sphere model

Neglecting higher order terms we write (3.3), in the region $r \leq 2$, as

$$\ddot{x} + \omega_{\rm Mie}^2 x + \alpha x^2 = -E_{\rm l}(t). \tag{3.13}$$

We solve (3.13) by the method of perturbation [72]. For analytical tractability of the perturbation method we assume a laser field $E_{\rm l}(t) = E_0 \sin(\omega_{\rm l} t/2n)\cos(\omega_{\rm l} t)$. The complementary solution $x_{\rm cp}$ and the particular integral $x_{\rm pi}$ of Eq. (3.13) satisfy respectively the equations

$$\begin{aligned} \ddot{x}_{\rm cp} + \omega_{\rm Mie}^2 x_{\rm cp} + \alpha x_{\rm cp}^2 &= 0, \\ \ddot{x}_{\rm pi} + \omega_{\rm Mie}^2 x_{\rm pi} + \alpha x_{\rm pi}^2 &= -E_{\rm l}(t). \end{aligned} \tag{3.14}$$

The successive corrections [72] have been taken into account both in the displacement x and in the frequency ω i.e., $x_{\rm cp} = x_{\rm cp}^{(0)} + x_{\rm cp}^{(1)} + x_{\rm cp}^{(2)} + \cdots$ and $\omega = \omega_{\rm Mie} + \omega^{(1)} + \omega^{(2)} + \cdots$. Here, $x_{\rm cp}^{(0)}$, $x_{\rm cp}^{(1)}$ and $x_{\rm cp}^{(2)}$ are the $0^{\rm th}$, $1^{\rm st}$, $2^{\rm nd}$ corrections for the displacement and $\omega_{\rm Mie}$, $\omega^{(1)}$ and $\omega^{(2)}$ are the $0^{\rm th}$, $1^{\rm st}$, $2^{\rm nd}$ corrections for the frequencies, respectively. The detailed solution is given in the appendix A. The successive corrections to the frequency ω are found as $\omega^{(1)} = 0$ and $\omega^{(2)} = -5\alpha^2 a_0^2/(12\omega_{\rm Mie}^3)$ with the amplitude of the oscillations a_0 that depends upon the driver strength. The value of $\omega^{(2)}$ being negative, the effective frequency $\omega = \omega_{\rm Mie} - 5\alpha^2 a_0^2/(12\omega_{\rm Mie}^3)$ decreases as the amplitude a_0 of the oscillations increases with the increasing driver strength. This is in qualitative agreement with the results in Fig. 3.3. The complete solution is found by $x = x_{\rm cp} + x_{\rm pi}$. The velocity of

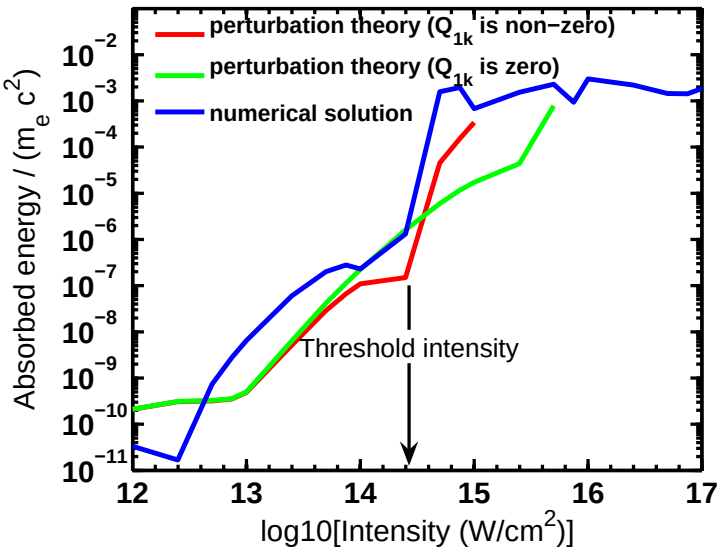

Figure 3.4: Variation of absorbed energy scaled with rest electron energy $m_e c^2$ as a function of laser intensity for cluster of radius $R = 3.2\,\text{nm}$ and charge density $\rho/\rho_c = 10$. We take an $n = 8$-cycle sin-pulse $E_l(t) = E_0 \sin(\omega_l t/2n)\cos(\omega_l t)$ of wavelength $\lambda = 1056\,\text{nm}$. The intensity (shown as threshold intensity) at which the full numerical solution (blue) of RSM jumps is closely justified by the results from the perturbation theory (red). At the threshold intensity the energy absorption is 2-4 order of magnitude higher than below it. After the threshold intensity energy absorption remains almost constant.

the electronic sphere is obtained analytically using $v = \mathrm{d}x/\,\mathrm{d}t$ while the total energy is calculated as $E_{\text{tot}} = mv^2/2 + qV(x)$ with mass m and charge q of the electronic sphere.

Absorption of energy at various laser intensities

We now study the laser energy absorption by pre-ionized clusters using the afore mentioned perturbative solution. Figure 3.4 shows the variation of the absorbed energy scaled with the electron rest energy $m_e c^2$ as a function of the peak laser intensity for the charge density $\rho/\rho_c = 10$ and an $n = 8$-cycle pulse $E_l(t) = E_0 \sin(\omega_l t/2n)\cos(\omega_l t)$ of wavelength $\lambda = 1056$ nm. Energy absorption curves from the numerical (blue) solution of (3.3) and the perturbative (red) approximations show qualitative agreement below the intensity 10^{15} W/cm^2. The disagreement between the two solutions at higher intensities are due to the approximate potential in the perturbative solution. However, both numerical and the perturbative solutions show a sudden 2-4 order of magnitude higher absorption around an identical value of the laser intensity, shown as threshold intensity in Fig. 3.4. This abrupt behavior of absorption about the threshold intensity is due to the term containing $Q_{1k} \propto 1/(\omega_{\text{Mie}}^2 - 4\omega_k^2)^2 \approx 1/\omega_l^2(\omega_{\text{Mie}}^2/\omega_l^2 - 4)^2$ in the perturbative solution (given in appendix A). The energy absorption result from the perturbative solution without the term Q_{1k} is also shown in Fig. 3.4. For the charge density $\rho/\rho_c = 10$ the value of $\omega_{\text{Mie}}^2/\omega_l^2 = 10/3$. Thus the denominator of Q_{1k} becomes smaller and the electronic sphere passes through a resonance, explaining the abrupt absorption of energy. The perturbation

theory approximately predicts the intensity at which the electronic sphere absorbs energy resonantly from the laser field and gives us an understanding towards the collisionless absorption in clusters. As ρ/ρ_c increases the resonance absorption occurs at higher values for the threshold intensity, and further corrections are needed. While it is difficult to predict the threshold intensity from the perturbative solution at higher cluster charge densities, it can be well-approximated by a vanishing barrier approximation (shown in Sec. 3.1.4).

3.1.3 NLR in a circularly polarized laser field

Clusters in a circularly polarized (CP) laser field received less attention in the literature. It is not known *a priori* how the outer ionization and energy absorption by clusters depend on the laser polarization. In laser-atom interaction the laser polarization has dramatic effects: since in CP the free electrons do not return to their parent atom all the atomic effects relying on re-scattering such as high-order harmonic generation, high-order above-threshold ionization, and non-sequential ionization are strongly suppressed. In the context of clusters, the study of the absorption efficiency as a function of the laser polarization can help to discriminate among different absorption mechanisms. For instance, if laser energy absorption was due to "collisions with the cluster boundary" [14] it would be suppressed in CP because the electrons mainly swirl around parallel to the "cluster boundary" rather than crossing (and hence colliding) with it. However, as we will show, the absorption of laser energy is largely independent of the laser polarization, thus ruling out "collisions with the cluster boundary" as a meaningful absorption mechanism.

Two-dimensional rigid sphere model

Let us first extend the RSM to CP. In a CP laser field with electric field components in x- and y-direction, the equation of motion for the electronic sphere in the rigid sphere approximation of a cluster can be written as

$$\left\{ \begin{array}{c} \ddot{r}_x \\ \ddot{r}_y \end{array} \right\} + \frac{g(r)}{r} \left\{ \begin{array}{c} r_x \\ r_y \end{array} \right\} = -\frac{1}{R\omega_l^2} \left\{ \begin{array}{c} E_l^x(\tau) \\ E_l^y(\tau) \end{array} \right\}. \tag{3.15}$$

Here, $r_x = x/R$, $r_y = y/R$, $r = \sqrt{r_x^2 + r_y^2}$, and

$$E_l^x(\tau) = \frac{E_0}{\sqrt{2}} \sin^2(\tau/2n)\cos(\tau), \tag{3.16}$$

$$E_l^y(\tau) = \frac{E_0}{\sqrt{2}} \sin^2(\tau/2n)\sin(\tau). \tag{3.17}$$

One identifies $E_x = g(r)r_x/r$ and $E_y = g(r)r_y/r$ as the two components of the restoring force in (3.15). Note that we have divided the electric field components by a factor $\sqrt{2}$ so that the ponderomotive energy $U_p = E_0^2/4\omega_l^2$, (i.e., the time-averaged quiver energy of a free electron in the laser field) is the same as in the LP case with the same E_0 (otherwise

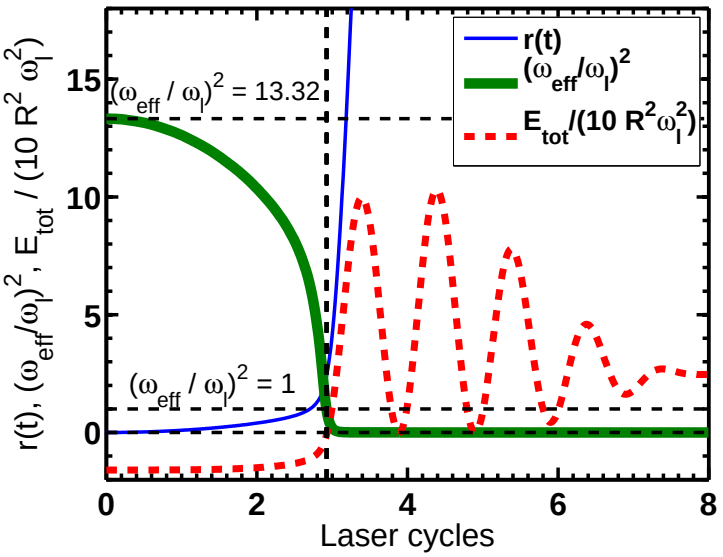

Figure 3.5: Typical behavior of $(\omega_{\rm eff}(\tau)/\omega_{\rm l})^2$ (green, top left solid line) vs laser cycles above the threshold intensity $\simeq 3\times10^{16}{\rm W/cm^2}$ for circular polarization, $(\omega_{\rm Mie}/\omega_{\rm l})^2 = 40/3$, and cluster radius $R = 3.2\,{\rm nm}$. Here, $E_0/R\omega_{\rm l}^2 \simeq 8.2$, corresponding to a laser intensity $\simeq 5\times10^{16}{\rm W/cm^2}$, $n = 8$-cycle $\sin^2$-pulse with components $E_{\rm l}^x(\tau) = E_0\sin^2(\tau/2n)\cos(\tau)/\sqrt{2}$, $E_{\rm l}^y(\tau) = E_0\sin^2(\tau/2n)\sin(\tau)/\sqrt{2}$, and wavelength $\lambda = 1056\,{\rm nm}$. Excursion r (blue, middle left solid line) and energy $E_{\rm tot}/R^2\omega_{\rm l}^2$ (red, dashed line) of the electron sphere are also plotted. The energy $E_{\rm tot}/R^2\omega_{\rm l}^2$ is scaled down by a factor 10 to display within the excursion and the frequency range. Outer ionization (i.e., $E_{\rm tot}/R^2\omega_{\rm l}^2 \geq 0$) and occurrence of NLR $[\omega_{\rm eff}(\tau)/\omega_{\rm l}]^2 = 1$ always coincide (dashed vertical).

$U_{\rm p}$ would be a factor of two higher in the CP case). The square of the effective, time-dependent oscillator frequency in the CP laser field can be written as

$$\left[\frac{\omega_{\rm eff}(\tau)}{\omega_{\rm l}}\right]^2 = \frac{r_x E_x + r_y E_x}{r^2} = \frac{g[r(\tau)]}{r(\tau)}, \tag{3.18}$$

which has the same form as in the LP case (3.9). Earlier, in Fig. 3.2, it was shown that NLR and outer ionization in the RSM only occur when a threshold laser intensity is crossed. The same is true for the occurrence of NLR with CP light. Figure 3.5 shows the temporal behavior of $[\omega_{\rm eff}(\tau)/\omega_{\rm l}]^2$ above the threshold driver strength for an $n = 8$-cycle CP laser pulse of wavelength $\lambda = 1056\,{\rm nm}$. Here the cluster charge density is 40 times over-critical, i.e., $(\omega_{\rm Mie}/\omega_{\rm l})^2 = 13.32$ at which $[\omega_{\rm eff}(\tau)/\omega_{\rm l}]^2$ starts and drops with increasing driver field during the pulse. The NLR $[\omega_{\rm eff}(\tau)/\omega_{\rm l}]^2 = 1$ is passed at the time indicated by the vertical line. As in the LP case in Fig. 3.2, the electron sphere is set free at the time the NLR is passed: the energy of the electron sphere passes through zero, and the excursion sharply increases to a high value. It is also clear from Fig. 3.5 that once the electronic sphere is set free, the frequency drops to zero, and the total absorbed energy remains positive. A zero effective frequency implies an infinite period, i.e, the electron sphere does not return to the ion sphere. The main difference between Fig. 3.5 and Fig. 3.2 is that in the case of the CP laser field the decrease of the effective frequency

is smooth (i.e., no oscillations) since the electric field vector rotates but its absolute value remains constant. As a consequence, the electron sphere spirals out, staying away from the potential center where $\omega_{\text{eff}} = \omega_{\text{Mie}}$. For LP instead, the electron sphere is driven through the origin and hence the effective frequency undergoes oscillations before it drops to the resonance value, as visible in Fig. 3.2. NLR is clearly identified in both cases.

3.1.4 Prediction of the threshold intensity for the NLR

NLR occurs above a threshold driver strength. Beyond this driver strength the rigid electron sphere gains laser energy which is many order of magnitude higher than below the threshold (see Fig. 3.1). In an open potential such as (3.10) the electron sphere is detached from the ion sphere above the threshold driver strength, i.e., appreciable energy absorption and outer ionization occur simultaneously. However, NLR occurs in closed potentials as well [32].

The threshold driver strength for the NLR can be estimated. The dimensionless potential $U(r) = V(r)/(\omega_{\text{Mie}}^2 R^2)$ of the electron sphere in the ionic field can be written as

$$U(r) = \frac{r^2}{2} - \frac{3r^3}{16} + \frac{r^5}{160}, \quad r \leq 2. \tag{3.19}$$

Application of a static electric field E_0 (corresponding to the peak field strength of a low-frequency laser field), suppresses the potential in one direction by the amount $RE_0\, r$. The effective potential seen by the electron sphere is $U_{\text{eff}}(r) = U(r) - \hat{E}_0\, r$ with $\hat{E}_0 = E_0/(\omega_{\text{Mie}}^2 R)$. The potential barrier vanishes if $U'(r_{\text{v}}) - \hat{E}_0 = 0$ and $U''(r_{\text{v}}) = 0$, leading to $r_{\text{v}} = 1$, and the NLR threshold intensity is estimated to be

$$I_{\text{th}}^{\text{VBA}} = E_0^2 = \left(\frac{5}{32}\frac{\rho}{\rho_{\text{c}}}\omega_{\text{l}}^2 R\right)^2. \tag{3.20}$$

We call this the vanishing-barrier-approximation (VBA).

In atomic ionization the so-called over-the-barrier approximation (OBA) or Bethe-rule [52] allows to estimate at which electric field strength a certain atomic charge state dominates. If one applies the OBA to the RSM one obtains the two equations $U_{\text{eff}}(r_{\text{b}}) = 0$ and $U'(r_{\text{b}}) - \hat{E}_0 = 0$ with r_{b} the barrier location. One finds $r_{\text{b}} \simeq 1.613$. This gives the OBA threshold intensity of the NLR

$$I_{\text{th}}^{\text{OBA}} \simeq \left(\frac{10}{83}\frac{\rho}{\rho_{\text{c}}}\omega_{\text{l}}^2 R\right)^2, \tag{3.21}$$

which underestimates the numerically determined threshold intensity, as we will show now.

Figure 3.6 shows the threshold intensity as a function of the cluster charge density $\rho/\rho_{\text{c}} = 10$–$160$ (corresponding to average charge states $\simeq 1 - 16$ for xenon). The numerically determined threshold intensities for LP (3.3) and CP (3.15) laser light show that when the cluster charge density is low, the NLR occurs almost at the same value of

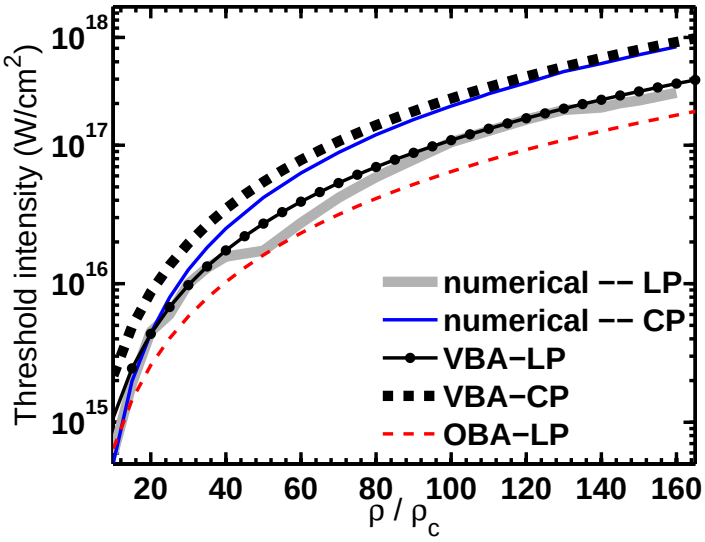

Figure 3.6: NLR threshold intensities in the RSM vs the cluster charge density ρ/ρ_c for linearly (LP) and circularly (CP) polarized laser fields. Results from the full numerical solution of (3.3) with LP (grey, thick solid), (3.15) CP (thin solid), the vanishing barrier approximation (VBA-LP, line with bullets) (3.20), and the VBA corrected for CP (upper thick dashed) are shown (see text for a discussion). The over-the-barrier approximation (OBA) (3.21) (lower thin dashed) underestimates the exact threshold intensities.

the threshold intensity, irrespective of the polarization. As the charge density increases the NLR threshold intensity appears to be higher for CP than for LP. The VBA (3.20) of the threshold intensity is in good agreement with the numerical result for LP whereas the OBA (3.21) underestimates it. This fact might be related to the recently observed "enhanced saturation intensities" in the ionization of finite size systems such as C_{60} (see, e.g., [73, 74] and references therein), indicating that the latter might neither be a many-electron nor a quantum effect but due to the finite size of the target.

The difference of the threshold intensities for LP and CP is due to the definition of the CP field (3.16), (3.17) where a factor $2^{-1/2}$ has been introduced in order to render the ponderomotive potential equal for LP and CP. However, for the threshold intensity it is the electric field (or the intensity) that matters, not U_p. For a given E_0 the laser intensity is $I_0 = E_0^2$ in the LP case but only $I_0/2$ for CP. Therefore, the upper black, dashed line in Fig. 3.6 shows the VBA threshold intensity multiplied by a factor of two, which is in good agreement with the numerical results for the CP laser field at higher charge densities.

So far we have studied the NLR absorption of laser energy in a simplified model system assuming an anharmonic potential generated by the ions in which the homogeneous and rigid electron cloud moves. In reality, the potential builds up during the interaction with the laser pulse because of ionization. The delicate interplay of inner ionization, energy absorption by various mechanisms, and outer ionization can be simulated using methods such as PIC or molecular dynamics. Previous work [69,70], studying LP short laser pulses, showed that NLR (3.2) can be clearly identified in such simulations as well.

3.2 Nonlinear resonance: particle-in-cell results

In this section we present results obtained from three-dimensional PIC simulations. The size of the cluster considered here is much smaller than both the wavelength λ and the skin depth $\lambda_{\text{skin}} \equiv c/\omega_{\text{p}}$ (c is the speed of light in vacuum) so that the propagation of the laser pulse needs not be taken into account, and the dipole approximation $\boldsymbol{E}_{\text{l}}(\boldsymbol{r}, t) \simeq \boldsymbol{E}_{\text{l}}(t)$ can be applied. The size L of the cubic grid on which the charge density and the self-consistent potential $\Phi(\boldsymbol{r}, t)$ are calculated is typically $L \simeq 17R$ with 128^3 grid cells. The number of PIC particles per grid cell in the initial configuration is $\simeq 10$. Because of the short pulse durations studied in this chapter, the ions are fixed, forming a homogeneous background. Electron-ion collisions are neglected in our PIC treatment so that absorption of laser energy can only proceed through collisionless processes.

We present results from parametric studies where pre-ionized clusters of various fixed charge densities are chosen as the initial configuration (corresponding to different degrees of inner ionization) so that the potential of the ionic background is exactly compensated by the electronic charge distribution. The cluster is then exposed to $n = 8$-cycle $\sin^2$-pulses $E_{\text{l}}(t) = E_0 \sin^2(\omega_{\text{l}} t/2n) \cos(\omega_{\text{l}} t)$ of near infrared wavelength $\lambda = 1056\,\text{nm}$, i.e., the total pulse duration is 28 fs. A PIC electron has the same charge to mass ratio as a "real" electron, that is, $e/m = -1$ in atomic units. Each PIC electron moves under the influence of the external laser field and the space charge field $\boldsymbol{E}_{\text{sc}} = -\boldsymbol{\nabla}\Phi(\boldsymbol{r}, t)$ due to the potential $\Phi(\boldsymbol{r}, t)$ that is created by all charges. The equation of motion of the ith PIC electron reads

$$\ddot{\boldsymbol{r}}_i + \boldsymbol{E}_{\text{sc}}(\boldsymbol{r}_i, t) = -\boldsymbol{E}_{\text{l}}(t). \tag{3.22}$$

Each time step the particle charges are mapped to the grid as explained in chapter 2. The potential $\Phi(\boldsymbol{r}, t)$ is calculated by solving Poisson's equation using Dirichlet boundary conditions ($\Phi(t) = 0$ at the boundary is a good approximation for sufficiently big grids; otherwise a multipole expansion of the potential is adopted to specify the boundary values as in chapter 4).

3.2.1 Results for linear polarization

We consider pre-ionized clusters of fixed radius $R = 3.2\,\text{nm}$ (e.g., $\text{Xe}_{N_{\text{i}}}$ with $N_{\text{i}} \simeq 1600$) but of various charge densities ρ/ρ_{c} which varies from 20 to 100. Figure 3.7 shows the absorbed energy per electron in units of the ponderomotive potential $U_{\text{p}} = E_0^2/4\omega_{\text{l}}^2$, i.e., the time-averaged quiver energy of a free electron in the laser field. One sees that the absorbed energy per electron is on the order of U_{p}. However, the absorbed energy is nonlinear in U_{p} and displays a maximum before it drops because of the saturation of outer ionization. The depletion is due to the fact that at a given intensity most (if not all) electrons are removed from the cluster (complete outer ionization). Further inner ionization would be required to generate "fresh" electrons that could continue to absorb energy. The maxima in the PIC absorption curves are located close to the threshold intensity predicted by the RSM (see RSM-result for $\rho/\rho_{\text{c}} = 40$). With increasing charge density the maxima of the absorbed energy (divided by U_{p}) move towards higher laser

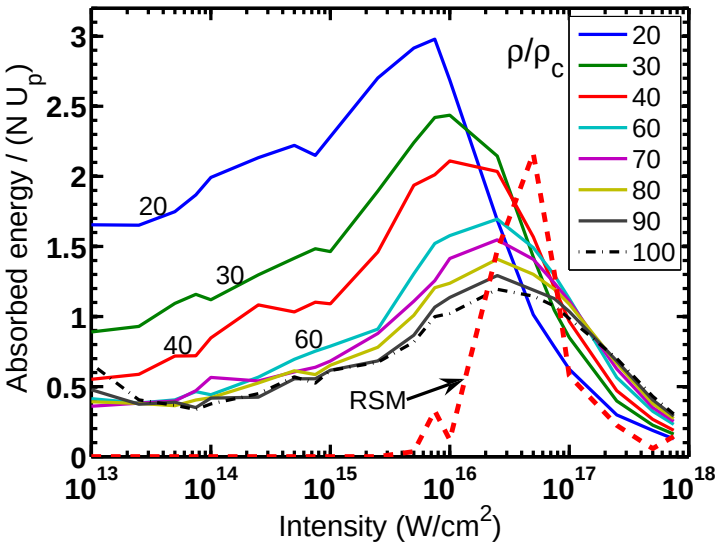

Figure 3.7: PIC results for a Xe_{1600} cluster ($R = 3.2\,\mathrm{nm}$). Total absorbed energy per electron in units of U_p vs laser intensity for charge densities between 20 and 100 times the critical density, corresponding to average charge states between 1.6 and 8. The prediction of the RSM for $\rho/\rho_\mathrm{c} = 40$ is included in the plot (dashed).

intensities while the absorbed energy per electron decreases. The total absorbed energy around the maximum of the PIC absorption curves (RSM as well) is on the order of $2U_\mathrm{p} = 5$–$6\,\mathrm{keV}$, which has been also reported in experiments of intense laser clusters interactions [9].

In PIC simulations no sharp intensity threshold exists since each PIC electron sees its own time-dependent field (space charge field plus the laser field). Therefore sharp jumps (as seen in the RSM, e.g., Fig. 3.1) are absent.

As mentioned earlier, the absorption of energy by a PIC electron depends upon the self-consistent potential which develops during the laser pulse due to outer ionization. As a result different PIC electrons move along different trajectories, "see" a different potential, and thus are set free at different times. Figure 3.8 shows a snapshot of the collective potential $\Phi(\boldsymbol{r}, t)$ at time $\omega_\mathrm{l} t/2\pi = 4.81$ for a cut at $z = 0$ (and various y throughout the cluster). The most lower curve represents the potential for $y = z = 0$. The red circles represent the total energy $E_{\mathrm{tot},i} = \dot{\boldsymbol{r}}_i^2(t)/2 - \Phi(\boldsymbol{r}_i, t)$ of individual PIC electrons located within the simulation box at that time.

One observes that several PIC electrons are accumulated near the left bottom of the potential well at this time. These PIC electrons with $E_{\mathrm{tot},i} < 0$ remain bound since the laser field amplitude is already decreasing from the 4th cycle onward.

The total energy of a PIC electron which leaves the potential well when its excursion becomes $x/R \simeq 2.88$ at the same time is also shown. This excursion approximately satisfies the NLR condition $\omega_\mathrm{eff}/\omega_\mathrm{l} = 1$ for the charge density $\rho/\rho_\mathrm{c} = 40$, as identified in Fig. 3.3 with the RSM analysis. The total energy curve shows how the particle, starting with zero energy at $t = 0$, drops into the potential as the latter builds up owing to outer

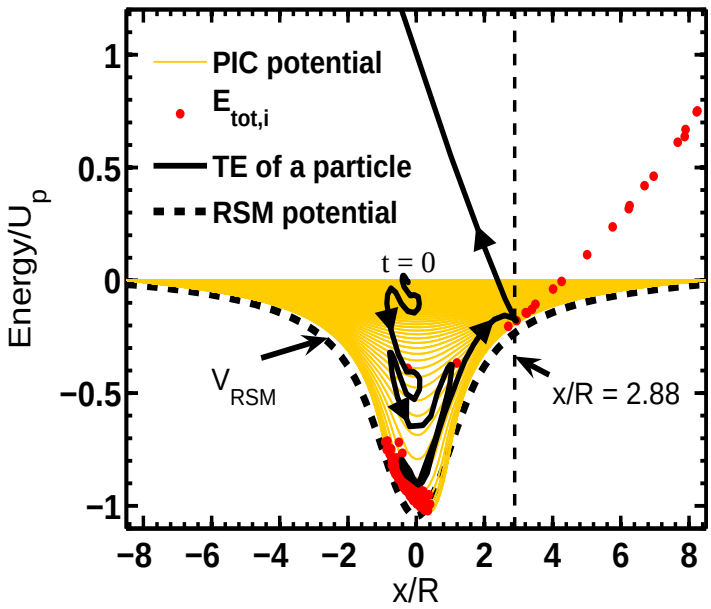

Figure 3.8: Energy and self-consistent potential Φ from the PIC simulation vs the excursion x/R in laser polarization direction. Yellow lines represent cuts of the potential Φ at time $\omega_\mathrm{l} t/2\pi = 4.81$ for different y and $z = 0$. The circles (red) represent the total energy $E_{\mathrm{tot},i}$ of individual PIC electrons located within the simulation box at that time. The total energy (TE) of a PIC electron (black, bold) that is outer ionized when the excursion $x/R \simeq 2.88$ meets the condition $\omega_\mathrm{eff} = \omega_\mathrm{l}$ at the same time (see Fig. 3.3 for the charge density $\rho/\rho_\mathrm{c} = 40$) is shown, arrows indicating the time evolution (starting from $t = 0$). The RSM potential is included (dashed). The peak laser intensity is $I_0 = 2.5 \times 10^{16}$ W/cm^2. Other parameters as in Fig. 3.7.

ionization. At the time of the emission of the PIC particle, the self-consistent potential is already close to the RSM potential (included dashed), i.e., the potential of the ionic background. The NLR is most clearly visible in the case of substantial outer ionization and for those electrons leaving "late". At lower laser intensities or during the early part of a high intensity laser pulse when most of the PIC electrons are inside the cluster, the PIC potential remains much shallower than the RSM potential shown in Fig. 3.8, and the occurrence of NLR (or even linear resonance) can hardly be resolved.

The NLR behavior exhibited by the PIC electron in Fig. 3.8 is not accidental. For the sake of an unequivocal and explicit identification of the NLR we now analyze the motion of all individual PIC electrons in the same way as it has been done with the motion of the electron sphere in the RSM in Sec. 3.1. Recalling (3.22), the equation for the effective, time-dependent oscillator frequency analogous to (3.18) for the i-th PIC electron reads

$$\omega_{\mathrm{eff},i}^2(t) = -\frac{[\boldsymbol{E}_\mathrm{l}(t) + \ddot{\boldsymbol{r}}_i(t)] \cdot \boldsymbol{r}_i(t)}{\boldsymbol{r}_i^2(t)} = \frac{\boldsymbol{E}_\mathrm{sc}(\boldsymbol{r}_i, t) \cdot \boldsymbol{r}_i(t)}{\boldsymbol{r}_i^2(t)}. \tag{3.23}$$

$\boldsymbol{E}_\mathrm{sc}(\boldsymbol{r}_i, t)$ depends on the position of *all* other particles $\neq i$, and the simulation starts with the charge-neutral cluster configuration i.e., $\boldsymbol{E}_\mathrm{sc}(\boldsymbol{r}_i, 0) \equiv \boldsymbol{0}$. Hence, a PIC electron "sees" initially an effective frequency $\omega_{\mathrm{eff},i}(0) = 0$. The laser field disturbs the charge

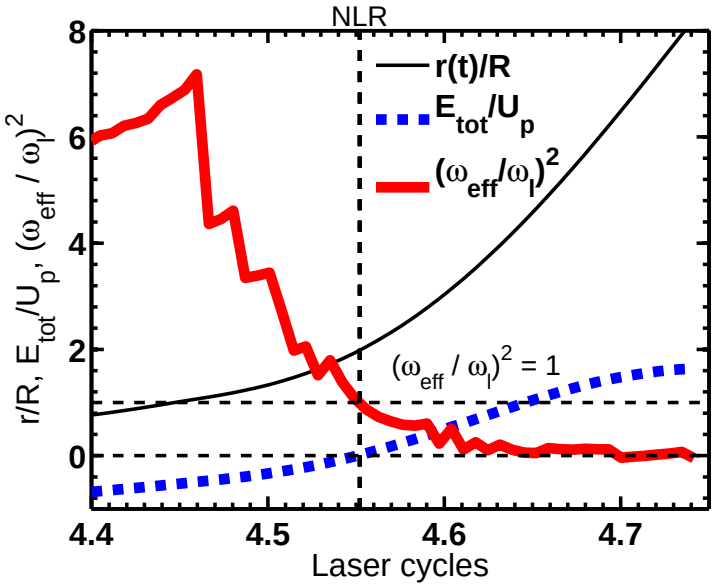

Figure 3.9: Effective frequency squared $(\omega_{\mathrm{eff},i}/\omega_\mathrm{l})^2$, excursion r_i/R, and the total energy $E_{\mathrm{tot},i} = \dot{\boldsymbol{r}}_i^2(t)/2 - \Phi(\boldsymbol{r}_i, t)$ for a PIC electron vs time in laser cycles. The total energy becomes positive only when the NLR is crossed (indicated by the vertical dashed line). This result resembles the RSM result in Fig. 3.2 when NLR is met. The charge density is $\rho/\rho_\mathrm{c} = 40$, the peak laser intensity is $I_0 = 2.5 \times 10^{16}$ W/cm^2. Other parameters as in Fig. 3.7.

equilibrium and $\omega_{\mathrm{eff},i}^2(t)$ becomes different from zero. $\omega_{\mathrm{eff},i}^2(t)$ may be even negative in regions of accumulated electron density (repulsive potential). As the cluster charges up, $(\omega_\mathrm{eff}/\omega_\mathrm{l})^2$ quickly increases beyond unity (where the RSM starts in the first place). The start from $\omega_{\mathrm{eff},i}(0) = 0$, the possibility of negative $\omega_{\mathrm{eff},i}^2(t)$, and the three-dimensionality are the main differences to the RSM analysis above.

Figure 3.9 shows the effective frequency squared, the total energy $E_{\mathrm{tot},i}(t)$, and the excursion r_i/R vs time for a PIC electron that leaves the cluster at $t = 4.55$ laser cycles. We define the time when, for a particular electron, $E_{\mathrm{tot},i}$ becomes > 0 as the ionization time of that electron. It is clearly visible in Fig. 3.9 that the PIC electron escapes only when the resonance line $(\omega_\mathrm{eff}/\omega_\mathrm{l})^2 = 1$ is passed. Figure 3.9 can be well compared with Fig. 3.2 showing ionization of the RSM via NLR.

In the case of PIC simulations the fulfillment of the NLR condition $(\omega_\mathrm{eff}/\omega_\mathrm{l})^2 = 1$ is necessary but not sufficient for ionization. As the potential builds up, the PIC electrons transiently meet the NLR condition, and, in fact, some electrons leave the cluster at that early stage when the potential is still shallow and the laser field is relatively weak. However, as the potential deepens, PIC electrons "dropping" below the energy necessary for NLR to occur, behave from then on similar to the RSM and may finally escape only by climbing up in the potential and hitting the NLR $(\omega_\mathrm{eff}/\omega_\mathrm{l})^2 = 1$. During the 0.4 laser cycles plotted in Fig. 3.9 the $(\omega_\mathrm{eff}/\omega_\mathrm{l})^2$-curve displays artificial, short-time scale fluctuations inherent in PIC simulations [65]. However, we checked that macroscopic observables such as the absorbed energy or the degree of outer ionization are well converged.

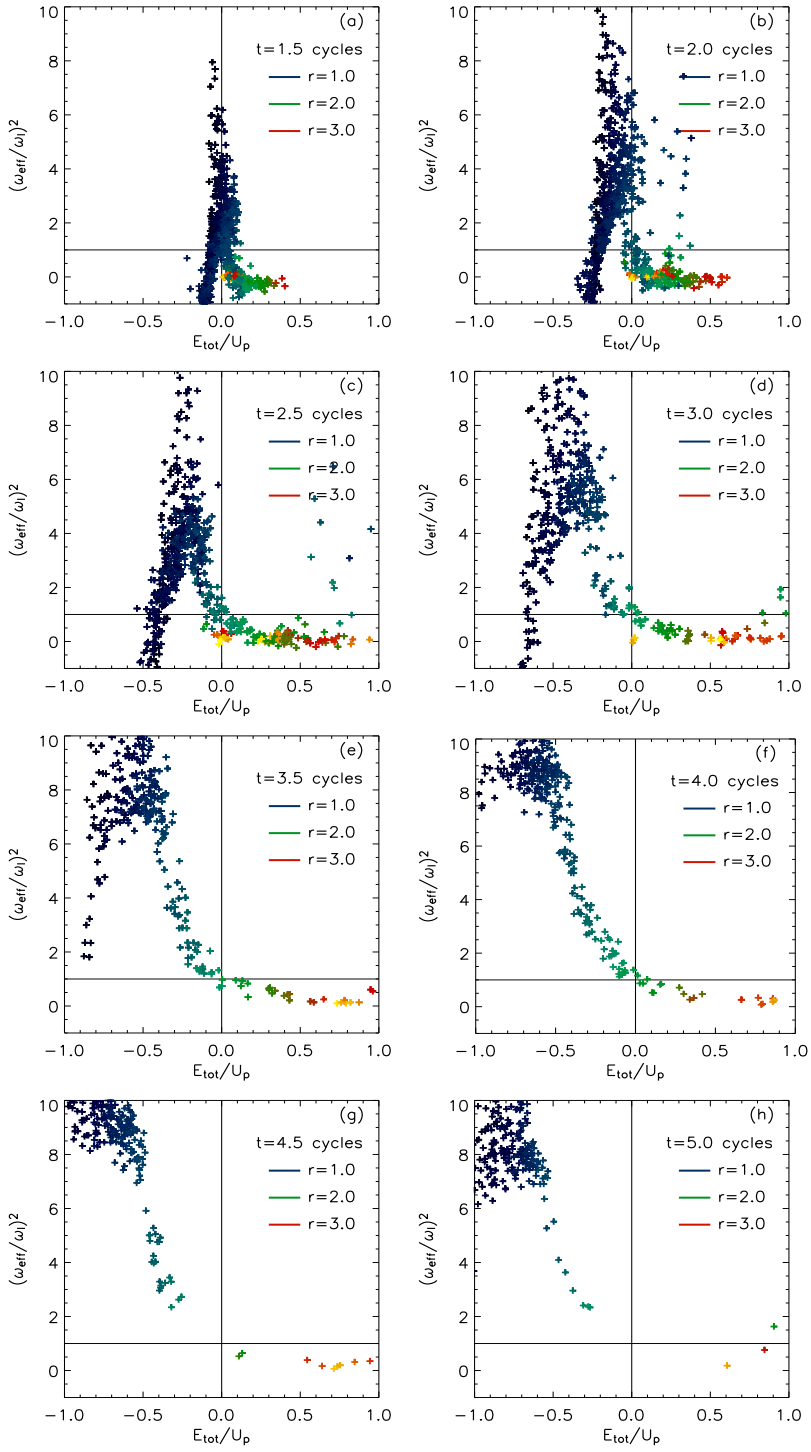

Figure 3.10: Snapshots of PIC electrons in the frequency vs energy-plane at times (a) $t = 1.5$, (b) $t = 2.0$, (c) $t = 2.5$, (d) $t = 3.0$, (e) $t = 3.5$, (f) $t = 4.0$, (g) $t = 4.5$, and (h) $t = 5.0$ laser cycles for LP, laser intensity 2.5×10^{16} Wcm^{-2}, and $(\omega_{\rm Mie}/\omega_{\rm l})^2 = 40/3$. Other parameters as in Fig. 3.9. The radial positions (in units of R) are color-coded. Electrons become free upon crossing the NLR, i.e., $(\omega_{\rm eff}^2/\omega_{\rm l}^2, E_{\rm tot}/U_{\rm p}) = (1, 0)$.

By following the dynamics of the electrons in the effective frequency vs energy-plane we identify the main pathway to outer ionization and efficient absorption. Figure 3.10a–h shows the scaled effective frequencies squared $(\omega_{\rm eff}/\omega_{\rm l})^2$ of the individual PIC electrons vs their energies $E_{\rm tot}(t) = \dot{\boldsymbol{r}}_i^2(t)/2 - \Phi(\boldsymbol{r}_i, t)$ they would have if the driver is switched off instantaneously at $t = 1.5$, 2, 2.5, 3, 3.5, 4, 4.5, and 5 laser cycles, respectively. At the time when, for a particular electron, $E_{\rm tot}$ becomes > 0 the ionization occurs for that electron. The laser intensity is $2.5 \times 10^{16}\,{\rm Wcm}^{-2}$, and the pre-ionized cluster is 40 times over-critical so that $(\omega_{\rm Mie}/\omega_{\rm l})^2 = 40/3$. As is clearly visible in Fig. 3.10, each electron reaches positive energy close to the point $(\omega_{\rm eff}^2/\omega_{\rm l}^2, E_{\rm tot}/U_{\rm p}) = (1, 0)$. The radial position of each electron is color coded, indicating that outer ionization occurs at radii around $2R$. During the early time of the laser pulse (Fig. 3.10a,b) when many electrons are still inside the cluster, $(\omega_{\rm eff}/\omega_{\rm l})^2$ spreads over a wide range, starting from the maximum value $(\omega_{\rm Mie}/\omega_{\rm l})^2$ down to negative values due to the repulsive force exerted by the compressed electronic cloud. Note that negative values in effective frequency occur mainly at early times where most of the electrons are still inside the cluster. Electrons with positive but very small $E_{\rm tot}$ and $\omega_{\rm eff}^2 \simeq 0$ represent low energetic electrons removed earlier during the pulse (see Fig. 3.10a,b). The occurrence of NLR is less clear for these early leaving electrons. As mentioned above, these electrons move in a shallow effective potential with $(\omega_{\rm eff}/\omega_{\rm l})^2 < 1$ when they leave the cluster with ease and with rather low kinetic energy because the laser intensity is still low at the time of their emission. Figures 3.10c–f show that most of the electrons escape from the cluster by passing through the channel $(\omega_{\rm eff}^2/\omega_{\rm l}^2, E_{\rm tot}/U_{\rm p}) = (1, 0)$ at radii around $2R$. It is also visible that more and more electrons are driven to positive frequency before they leave the cluster by passing through $(\omega_{\rm eff}^2/\omega_{\rm l}^2, E_{\rm tot}/U_{\rm p}) = (1, 0)$. This is so because as more and more electrons are freed, the remaining electrons experience predominantly the force by the ionic background, and they move deep into the potential (see their negative values in energy) where they experience the full Mie-frequency $\omega_{\rm Mie}/\omega_{\rm l} = 40/3$. In Fig. 3.10b–d, the few electrons with positive energy but small radii are those driven back to the cluster by the laser field. In Figs 3.10e,f electrons are strongly aligned (no scattered points) since the laser field is approaching its maximum (at $t = 4\,$cycles). After the peak of the laser pulse (Figs 3.10g,h) the restoring force of the ions on almost all electrons dominates the laser force.

One may object that, since the denominator in (3.23) necessarily increases while the numerator decreases for an electron on its way out of the cluster potential, that the passage through a point $(\omega_{\rm eff}^2/\omega_{\rm l}^2, E_{\rm tot}/U_{\rm p}) = (x, 0)$ with x *some* value $< (\omega_{\rm Mie}/\omega_{\rm l})^2$ is rather the consequence of outer ionization than the mechanism behind it. However, NLR only occurs at $x = 1$, and the results in Fig. 3.10 show only little spreading along $(\omega_{\rm eff}/\omega_{\rm l})^2$ at $E_{\rm tot} = 0$. Moreover, the fact that *both* the single electron energies become positive *and* the radii exceed $\simeq 2R$ when $(\omega_{\rm eff}/\omega_{\rm l})^2 = 1$ indicates that NLR is indeed the responsible mechanism behind outer ionization accompanied by efficient absorption of laser energy.

3.2.2 Results for circular polarization

Since many of the features of energy absorption and NLR in a LP laser field are common to the case of CP, we only point out the main differences. Equation (3.23) holds in the

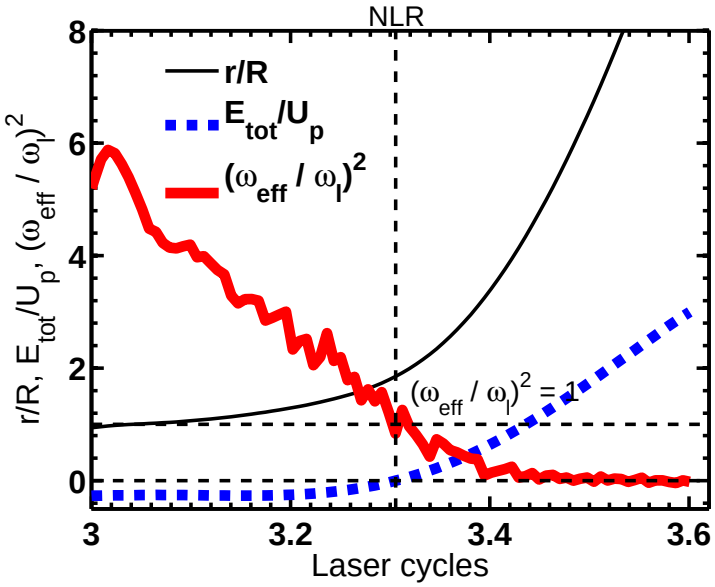

Figure 3.11: Effective frequency squared $(\omega_{\mathrm{eff},i}/\omega_\mathrm{l})^2$, excursion r_i/R, and the total energy $E_{\mathrm{tot},i} = \dot{\boldsymbol{r}}_i^2(t)/2 - \Phi(\boldsymbol{r}_i, t)$ for a PIC electron in a CP field vs time in laser cycles. The total energy becomes positive only when the NLR is crossed (indicated by vertical, dashed line). This result resembles the RSM result in Fig. 3.5. The charge density is $\rho/\rho_\mathrm{c} = 40$, the peak laser intensity is $I_0 = 2.5 \times 10^{16}$ W/cm^2.

CP laser field as well. Figure 3.11 shows the effective frequency squared vs time for one of the PIC electrons, together with the total energy $E_{\mathrm{tot},i}(t)$ and the excursion r_i/R. One can see that the PIC electron is freed (i.e., its total energy becomes positive) only when the resonance line $(\omega_\mathrm{eff}/\omega_\mathrm{l})^2 = 1$ is passed.

Figure 3.12 is the CP analogue of Fig. 3.10. The results are very much similar to the LP case shown in Fig. 3.10 and the arguments made there apply here as well. NLR is clearly observed. The main difference is that the PIC electrons are nicer aligned towards the resonance point, even at early times during the laser pulse (see Fig. 3.12 b, c, d). Almost no scattered particles are visible because the dynamics mainly consist of swirling around the cluster center rather than oscillating through it. The number of electrons returning to the cluster is much less so that the recombination and re-scattering probability is smaller in the case of CP. The same is observed in laser-atom interaction experiments, with important consequences for harmonic generation and non-sequential ionization.

Figure 3.13 shows the average value of the total absorbed energy per electron vs the peak laser intensity for cluster charge densities between $\rho/\rho_\mathrm{c} = 3$–40 in CP and LP laser fields. PIC results are compared with the RSM absorption results. The absorbed energy per electron in Figs. 3.13a–d is plotted in units of $R^2\omega_\mathrm{l}^2$ whereas the same results are shown in Figs. 3.13e–h in units of the ponderomotive energy U_p. The PIC results in Figs. 3.13a–d show that the absorbed energy increases linearly in the log-log representation up to a certain intensity and then tends to saturate due to the saturation of outer ionization. One sees that the saturation in the PIC results occur close to the RSM threshold intensity. Since with increasing charge density the restoring force due to the ions increases, the

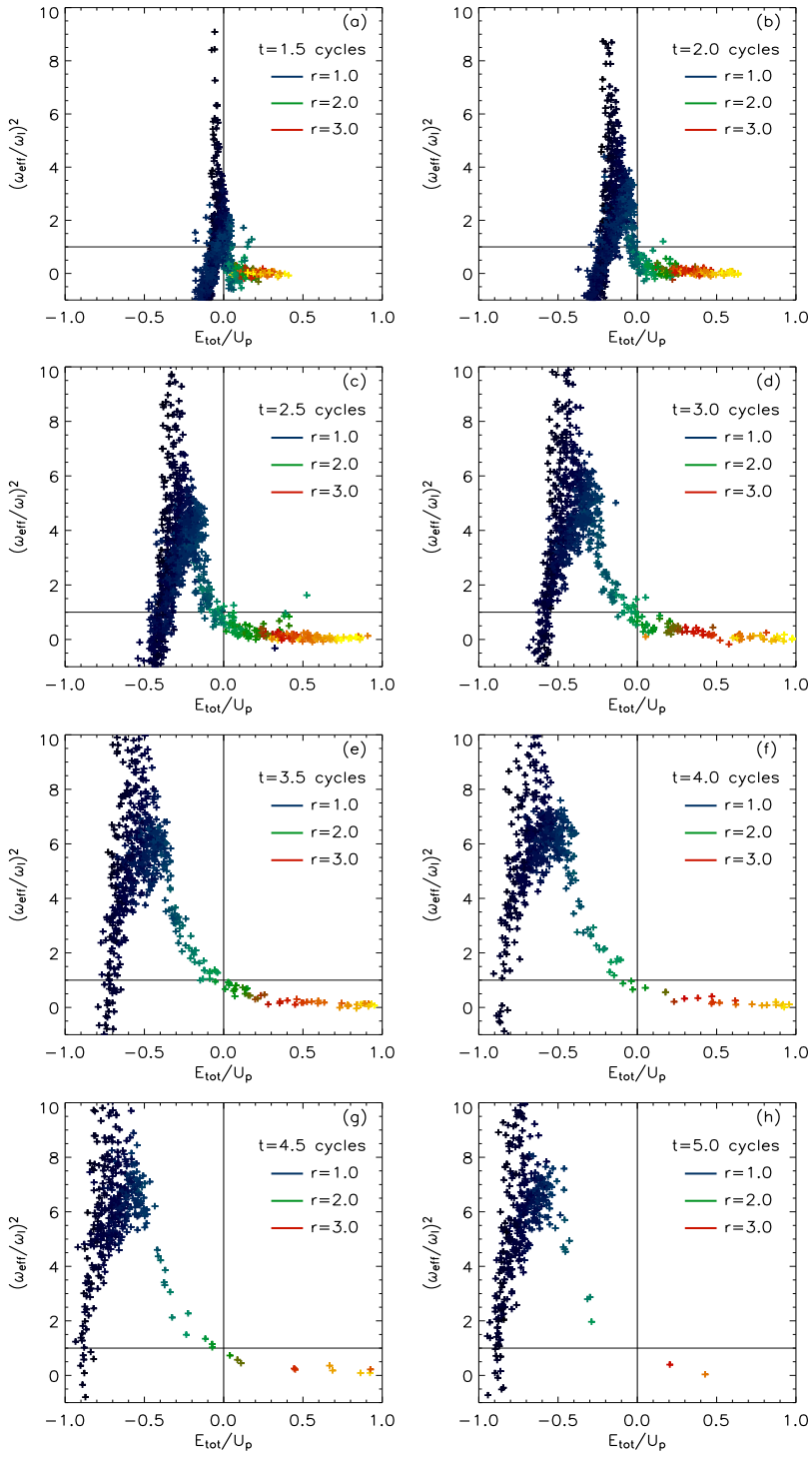

Figure 3.12: Snapshots of PIC electrons in the frequency vs energy-plane for CP at times (a) $t = 1.5$, (b) $t = 2.0$, (c) $t = 2.5$, (d) $t = 3.0$, (e) $t = 3.5$, (f) $t = 4.0$, (g) $t = 4.5$, and (h) $t = 5.0$ laser cycles for a laser intensity $2.5 \times 10^{16}\,\mathrm{Wcm}^{-2}$and $(\omega_{\mathrm{Mie}}/\omega_{\mathrm{l}})^2 = 40/3$. Other parameters as in Fig. 3.7. The radial positions (in units of R) are color-coded. Electrons become free upon crossing the NLR, i.e., $(\omega_{\mathrm{eff}}^2/\omega_{\mathrm{l}}^2, E_{\mathrm{tot}}/U_{\mathrm{p}}) = (1, 0)$.

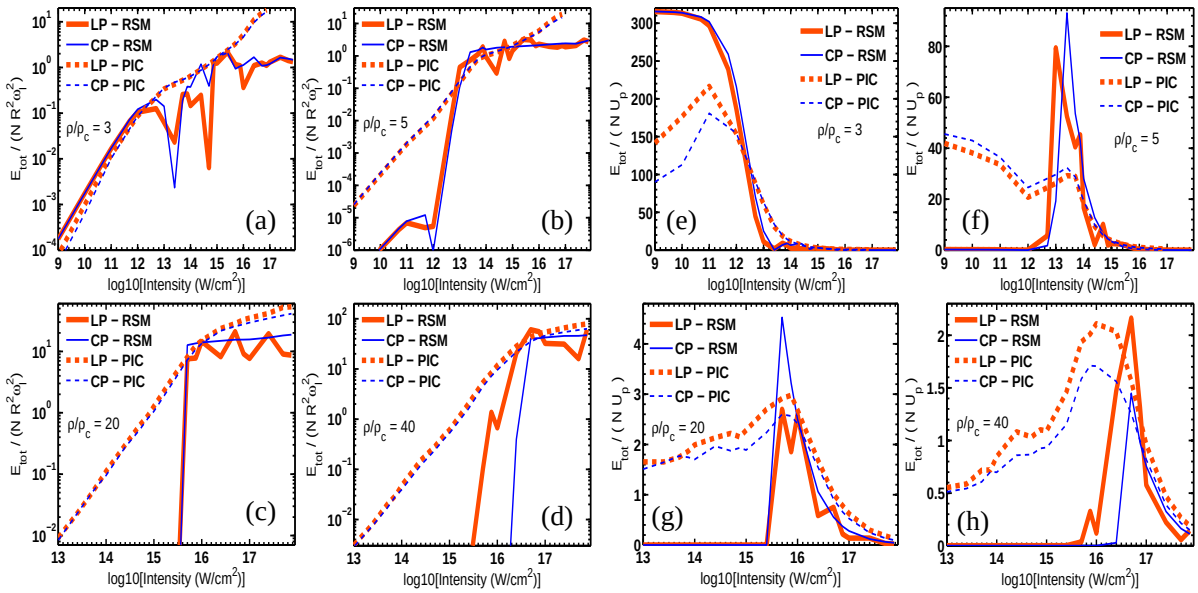

Figure 3.13: Total absorbed energy per electron in units of $R^2\omega_\mathrm{I}^2$ vs laser intensity for charge densities (a) $\rho/\rho_\mathrm{c} = 3$ (linear resonance), (b) $\rho/\rho_\mathrm{c} = 5$, (c) $\rho/\rho_\mathrm{c} = 20$, and (d) $\rho/\rho_\mathrm{c} = 40$. The absorbed energies for LP (red, lighter gray) and CP (blue, darker gray) using PIC (dashed) and the RSM (solid) are shown.

saturation of energy absorption in the RSM and PIC occur at higher laser intensities as the density increases from $\rho/\rho_\mathrm{c} = 3$ to $\rho/\rho_\mathrm{c} = 40$ in Fig. 3.13a–d. When outer ionization and the energy absorption saturate with increasing peak laser intensity, the average absorbed energy per electron divided by U_p (which is proportional to the so-called fractional absorption) starts decreasing in Figs. 3.13e–f. Figures 3.13a,e show that at linear resonance $\rho/\rho_\mathrm{c} = 3$, the absorbed energy is already high at low values of the laser intensity ($< 10^{12}\,\mathrm{Wcm}^{-2}$), and absorption is very efficient as compared to higher charge densities $\rho/\rho_\mathrm{c} = 5$–40, presented in Figs. 3.13b–d and Figs. 3.13f–h. In fact, Fig. 3.13e illustrates that the absorbed energy is on the order of $\sim 100U_\mathrm{p}$ (both in the RSM and in the PIC) before the saturation of outer ionization. However, one should bear in mind that at too low laser intensities inner ionization would not occur in the first place so that in reality there would be no absorption at all. Self-consistent inner ionization is taken into account in chapter 4.

The PIC results in Fig. 3.13 show that the energy absorption in CP and LP laser fields at all intensities and all charge densities are almost equally efficient. Also the outer ionization degrees are very similar for LP and CP, as shown in Fig. 3.14. Recalling that with our definition of the CP laser field the ponderomotive potential is equal for LP and CP while the electric field amplitude is not, we conclude that for the outer ionization degree and the absorbed energy mainly U_p matters and not the electric field amplitude. For the higher charge densities in Fig. 3.14c,d the small difference in the outer ionization degree close to saturation is probably related to the different threshold intensities for LP and CP, as discussed in Sec. 3.1.4.

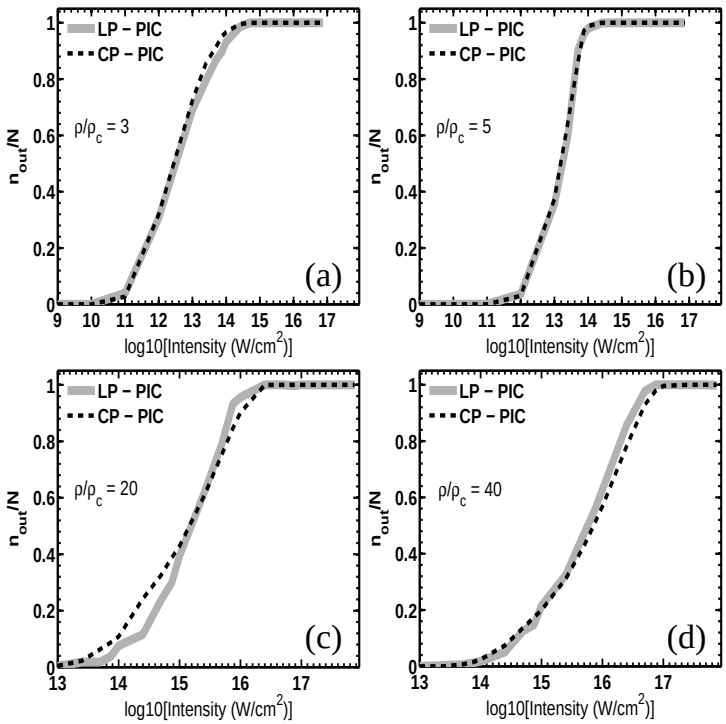

Figure 3.14: PIC results for the outer ionization degree $n_{\rm out}/N$ (where $n_{\rm out}$ is the number of electrons with $r > 2R$) after the laser pulse for linear (solid grey) and circular polarization (dashed black) for different charge densities $\rho/\rho_{\rm c} = 3$ (a), 5 (b), 20 (c), and 40 (d).

3.3 Summary

In summary, two different approaches to study collisionless laser energy absorption by clusters, namely (i) the rigid sphere model and (ii) particle-in-cell simulations, were pursued in this chapter. The goal was to identify the dominant mechanism of energy absorption and outer ionization of the cluster electrons in near infrared, short laser pulses where collisional absorption is known to be inefficient. We showed that the cluster electrons contributing to efficient absorption and outer ionization undergo nonlinear resonance, meaning that the instantaneous frequency of their motion in a time-dependent, anharmonic, effective potential transiently meets the laser frequency. Nonlinear resonance is the only possible absorption mechanism if the laser pulse is too short for the linear resonance to occur (or during the early cluster dynamics in longer pulses) and if electron-ion collisions (inverse bremsstrahlung) are negligible. In order to prove the occurrence of nonlinear resonance we used a method to analyze the results obtained from particle-in-cell simulations, namely the mapping of the system of electrons and ions that interact through their mean field onto a system of nonlinear oscillators.

The occurrence of nonlinear resonance in the particle-in-cell simulations presented in this work resembles the nonlinear resonance in the rigid sphere model. For a given cluster charge density, there is a threshold intensity around which the average electron energy displays a maximum conversion of laser energy. The threshold intensity can be calculated

using the newly introduced vanishing barrier approximation. The common over-barrier approximation—applicable to atoms—fails in the case of finite-size potentials and underestimates the required laser field strength for ionization.

The efficiency of energy absorption from the laser and outer ionization is almost the same for linear and circular polarization. For circular polarization there are much less "collisions with the cluster boundary" than for linear polarization. Hence "collisions with the cluster boundary" do not properly explain energy absorption. Instead, nonlinear resonance is the main absorption mechanism in both cases. To illustrate this, the rigid sphere model has been extended for circularly polarized laser pulses in this work.

In the next few chapters of this thesis we take self-consistent charge state distributions and mobile ions into account. It will be shown that nonlinear resonance clearly persists under these circumstances as well.

Chapter 4

Laser-cluster interaction: ionization ignition, asymmetric Coulomb explosion, and absorption by nonlinear resonance

Atomic clusters are known to absorb incident laser radiation much more efficiently than the atoms in a gas phase. High charge states [7, 8, 37, 39, 75–78] of cluster ions with kinetic energies in the MeV and keV-range [7, 8, 10, 37, 39, 75–80], electrons with keV energies [9, 10, 79, 81, 82], and harmonic radiation [83–85] at the frequencies equal to odd multiples of the incident laser frequency are a few remarkable outcomes of such an efficient laser absorption in experiments with rare-gas clusters.

As explained in chapter 3 for short laser pulses or in the early duration of long pulses linear resonance absorption does not occur. In this case electrons can absorb energy efficiently by meeting the nonlinear resonance (NLR). Using a rigid sphere model [30, 31, 69, 70] absorption was shown to be efficient above a threshold laser intensity. Such an intensity threshold was also seen in PIC results [28, 29, 69, 70]. In fact, experiments [82] with 28 fs 820 nm laser pulses reported nearly 80% laser energy absorption by rare-gas clusters at an intensity $10^{17}\mathrm{Wcm}^{-2}$ while 25% absorption was measured below the intensity $10^{16}\mathrm{Wcm}^{-2}$, confirming the role of NLR.

However, in the earlier PIC simulations of chapter 3, due to the assumption of fixed ionic charges and stationary ions we could not address how inner ionization and the cluster expansion dynamics may effect the NLR. Incorporating the self-consistent evolution of the ionic charges and ion motion in our PIC simulations we show in this chapter that NLR is a *robust phenomenon* which is *insensitive* to the ion dynamics. We present PIC results for Ar_N clusters (N up to 92096 atoms) and deuterium (D_N) clusters (N up to 103536 atoms) irradiated by near infrared, short-pulse (< 23 fs) lasers.

It is known that higher charge states of atoms in clusters are due to ionization ignition. We show that not all laser intensities lead to efficient ionization ignition. There may be "ionization depletion", meaning that cluster atoms deep inside the cluster are ionized

to charge states less than those of atoms in the gas phase because the laser field may be strongly shielded by the space charge field. The charge distribution is symmetric in a plane perpendicular to the polarization axis of a linearly polarized laser pulse but asymmetric in the plane of polarization. Higher charge states occur along the polarization direction than in the transverse directions. We show that such an asymmetry of the charge distribution leads to the asymmetry in the ion kinetic energy seen in cluster experiments [10, 37, 57].

A recent experiment [41] with hydrogen clusters (where the charge state distribution is necessarily homogeneous) reported spatial asymmetry in the ion energy spectra. By PIC simulations of deuterium clusters we show that this asymmetry is *always* present in case of clusters driven by a linearly polarized laser field. The observed asymmetry is independent of the cluster types since the spherical symmetry of the system is broken by the electron motion in a linearly polarized field. In Ref. [41] it was argued that the electron heating mechanism is "vacuum heating". However, the NLR is dominant in this case too.

This chapter is organized as follows: Section 4.1 describes necessary details of the PIC simulation. Section 4.2 illustrates how ionization ignition leads to the creation of higher charge states, asymmetric charge distributions and an asymmetric cluster expansion. Ion and electron energy spectra for argon clusters are reported and the laser energy absorption via NLR is discussed. Section 4.3 shows that asymmetric ion dynamics persist in the case of deuterium clusters as well. Finally, the chapter is summarized in Sec. 4.4.

4.1 Details of the simulation

This section describes necessary details of PIC simulations [65] not yet addressed in this work. A cluster of radius R and N atoms, is placed at the center of a computational box of volume Γ. The latter is divided into cubic grid cells. The atoms are initially placed according to the Wigner-Seitz radius r_{W} [6] such that $R = r_{\mathrm{W}} N^{1/3}$. In the present study R is much smaller than the infrared laser wavelength and the skin depth $\lambda_{\mathrm{skin}} \equiv c/\omega_{\mathrm{p}}$ (c is the speed of light in vacuum and ω_{p} is the plasma frequency). Therefore we neglect the propagation of the laser pulse and assume the dipole approximation $E_{\mathrm{l}}(\boldsymbol{r}, t) \simeq E_{\mathrm{l}}(t)$ for the laser field.

According to the Bethe rule [52] the laser field $E_{\mathrm{l}}(t)$ plus the space charge field $E_{\mathrm{sc}}(\boldsymbol{R}_i, t)$ at the position $\boldsymbol{R}_i$ of an ion, i.e., $E(\boldsymbol{R}_i, t) = |\boldsymbol{E}_{\mathrm{l}}(t) + \boldsymbol{E}_{\mathrm{sc}}(\boldsymbol{R}_i, t)|$ ionizes all ions $\mathrm{X}^{(\mathcal{Z}-1)+}$ to $\mathrm{X}^{\mathcal{Z}+}$, meeting the condition

$$E(\boldsymbol{R}_i, t) = |\boldsymbol{E}_{\mathrm{l}}(t) + \boldsymbol{E}_{\mathrm{sc}}(\boldsymbol{R}_i, t)| \geq I_{\mathrm{p}}^2(\mathcal{Z})/4\mathcal{Z} \tag{4.1}$$

where $\mathcal{Z}$ is the charge number, and $I_{\mathrm{p}}(\mathcal{Z})$ is the ionization potential. Initially, the space charge field $E_{\mathrm{sc}}(\boldsymbol{R}_i, t) = 0$ and all ions assume a charge state $\mathcal{Z} = 1$ solely by the laser field. This is also known as optical field ionization (OFI). After the OFI, the laser field disturbs the charge equilibrium. The charges are mapped to the numerical grid and Poisson's equation is solved for the potential $\Phi_G(x, y, z, t)$ on the grid points with a time dependent monopole boundary condition. Interpolating $\Phi_G(x, y, z, t)$ to the particle positions $\boldsymbol{r}_i$, the potential $\Phi(\boldsymbol{r}_i, t)$ and the space charge field $\boldsymbol{E}_{\mathrm{sc}}(\boldsymbol{r}_i, t) = -\nabla\Phi(\boldsymbol{r}_i, t)$ is computed.

Depending on the cluster size the space charge field $|\boldsymbol{E}_{\rm sc}(\boldsymbol{R}_i,t)|$ at an ion position $\boldsymbol{R}_i$ may soon exceed $E_{\rm l}(t)$, and the total field $E(\boldsymbol{R}_i,t)$ may produce ions of higher charge states ($\mathcal{Z}>1$). We neglect collisional effects which were proved unimportant at long wavelengths in previous works [13]. Mobile ions are considered. New electrons are "born" with the velocities and positions of their parent ions.

As long as a PIC electron is inside the computational box, the field at its location $\boldsymbol{r}_i(t)$ is $\boldsymbol{E}(\boldsymbol{r}_i,t)=\boldsymbol{E}_{\rm l}(t)+\boldsymbol{E}_{\rm sc}(\boldsymbol{r}_i,t)$. Outside the box $\boldsymbol{E}(\boldsymbol{r}_i,t)=\boldsymbol{E}_{\rm l}(t)$ is assumed due to an inappreciable $\boldsymbol{E}_{\rm sc}(\boldsymbol{r}_i,t)$. The equation of motion for a PIC electron reads

$$\ddot{\boldsymbol{r}}_i+\boldsymbol{E}_{\rm sc}(\boldsymbol{r}_i,t)=-\boldsymbol{E}_{\rm l}(t). \tag{4.2}$$

The equation of motion of each PIC ion of mass M reads

$$M\ddot{\boldsymbol{R}}_i-\boldsymbol{E}_{\rm sc}(\boldsymbol{R}_i,t)=\boldsymbol{E}_{\rm l}(t). \tag{4.3}$$

On the boundary $R_{\rm b}$ of the computational box the potential $\Phi_{\rm b}(R_{\rm b},t)$ is close to the monopole potential $\Phi_{\rm b}(R_{\rm b},t)=\int_\Gamma[\rho(x,y,z,t)-\rho_e(x,y,z,t)]\,{\rm d}\Gamma/R_{\rm b}$ which depends on the ionic charge density $\rho(x,y,z,t)$ and the electronic charge density $\rho_e(x,y,z,t)$ within the computational box.

4.2 Results for argon clusters

We present results for argon clusters ($r_{\rm W}=0.24$ nm) in a linearly polarized (along the x-direction), $n=8$ cycle $\sin^2$-laser pulse $E_{\rm l}(t)=E_0\sin^2(\omega_{\rm l}t/2n)\cos(\omega_{\rm l}t)$ of wavelength $\lambda_{\rm l}=800$ nm. The total pulse duration is ≈ 22 fs. Ions of different charge states are self-consistently produced. Simultaneously, the cluster expansion, outer ionization and energy absorption are recorded.

4.2.1 Inner ionization

Figures 4.1a,b show charge states vs positions (in units of the initial radius R) of various ions in the xy and yz-planes through the cluster center for an Ar_N cluster ($N=17256$) of radius $R=6.2\,$nm after a laser pulse of peak intensity $2.5\times10^{14}\mathrm{Wcm}^{-2}$. At this intensity only Ar^+ is expected by OFI. However, one observes ions with charge states $\mathcal{Z}=2,3$ indicating ionization ignition. Just after the OFI, the singly charged ion background leads to a static electric field $N/R^2\approx1.256$ which would be equivalent to a laser intensity $\approx 5.54\times10^{16}\mathrm{Wcm}^{-2}$ capable of producing charge states up to $\mathcal{Z}=8$ (if no electrons were present). Such a "static ionization ignition" would be depleted in the presence of electrons inside the cluster. During the pulse, the displacement of the electron cloud causes local charge imbalances which are maximum at the cluster boundaries along the x-axis and smaller at the cluster poles in the y and z-directions. As a result, $|\boldsymbol{E}_{\rm sc}(\boldsymbol{R}_i,t)|$ transiently becomes higher at the cluster poles along x than at the poles normal to the laser polarization, leading to "dynamical ionization ignition" [12, 15]. This explains the origin of higher ionic charges along the laser polarization (in Fig. 4.1a). The further

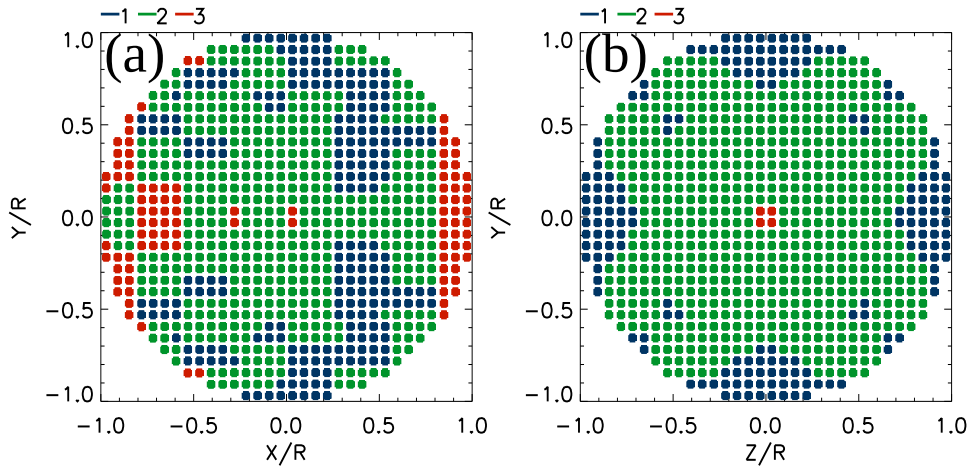

Figure 4.1: Results for an Ar_{17256} cluster of radius $R = 6.2$ nm and an $n = 8$ cycle laser pulse $E_l(t) = E_0 \sin^2(\omega_l t/2n)\cos(\omega_l t)$ of intensity $2.5 \times 10^{14}\mathrm{Wcm}^{-2}$. (a) Ion charge states at various ion positions in the xy-plane nearest to the $z = 0$ plane. Ion positions are in units of the initial radius R. (b) Charge states in the yz-plane nearest to the $x = 0$ plane.

charge asymmetry of a few ions (sitting opposite to each other at $\boldsymbol{R}_i$ and $-\boldsymbol{R}_i$) along the laser polarization axis (in Fig. 4.1a) is due to the unequal field amplitudes $|E_l(t) \pm E^x_{sc}(\boldsymbol{R}_i, t)|$ during the pulse. However $|\boldsymbol{E}_{sc}(\boldsymbol{R}_i, t)|$ is symmetric in the yz-planes, generating a symmetric ion charge distribution in Fig. 4.1b.

Figure 4.2 shows further evidence of ionization ignition (analogous to Fig. 4.1) at an intensity $2.5 \times 10^{15}\mathrm{Wcm}^{-2}$. Fig. 4.2a shows a maximum charge state $\mathcal{Z} = 8$ at the cluster poles along the laser polarization in addition to the charge states $\mathcal{Z} = 7 - 2$ in the cluster interior. Asymmetry of the charge distribution along the laser polarization direction due to the dynamical ionization ignition is also visible. Figure 4.2b shows a symmetric charge distribution (in the yz-plane) of ions as explained before. One does not observe charge states $\mathcal{Z} > 5$ in the yz-plane shown in Fig. 4.2b due to the absence of the laser field components E_{lx}, E_{ly}. In the atomic case, charge states $\mathcal{Z} < 4$ are conceivable at this intensity because of OFI alone. The required ionization energy to produce Ar^{8+} is ≈ 5.272 a.u. so that an order of magnitude higher laser intensity $\approx 2.65 \times 10^{16}\mathrm{Wcm}^{-2}$ would be required. Hence the space charge field together with the laser field (i.e., ionization ignition) must have produced the ions with charges $\mathcal{Z} = 4 - 8$. Ions with even higher $\mathcal{Z}$ values ($\mathcal{Z} = 8$, in this case) are produced at the cluster poles along the laser polarization. As a consequence, they experience a higher Coulomb repulsion force. The highly charged ions along the laser polarization expand faster than the ions having a lower charge in the transverse directions, as is visible in Fig. 4.2. As a result the spherical symmetry of the ionic background is broken. This is the reason for the experimentally observed asymmetric ion expansion [37].

Figure 4.3 shows the maximum charge state $\mathcal{Z}_{max}$, minimum charge state $\mathcal{Z}_{min}$, average charge state $\mathcal{Z}_{av}$ (defined as the total charge of the cluster divided by the number of ions N) and the charge states predicted by OFI [Eq. (4.1) with $E_{sc} = 0$] vs the laser

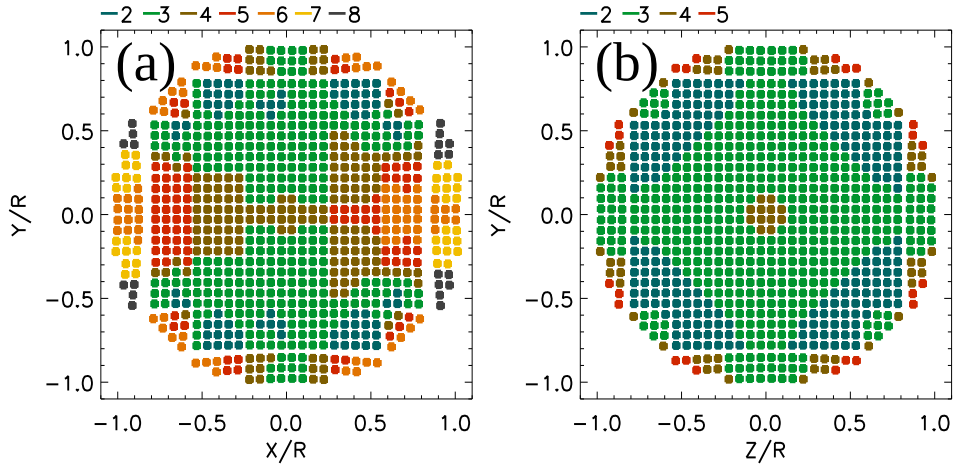

Figure 4.2: Charge distribution of ions at different planes of an Ar_{17256} cluster of radius $R = 6.2$ nm for a laser intensity $2.5 \times 10^{15}\mathrm{Wcm}^{-2}$. (a) Ion charge states in the xy and (b) yz-plane as in Fig. 4.1b. Maximum charge state $\mathcal{Z} = 8$ are seen. Other parameters are the same as in Fig. 4.1.

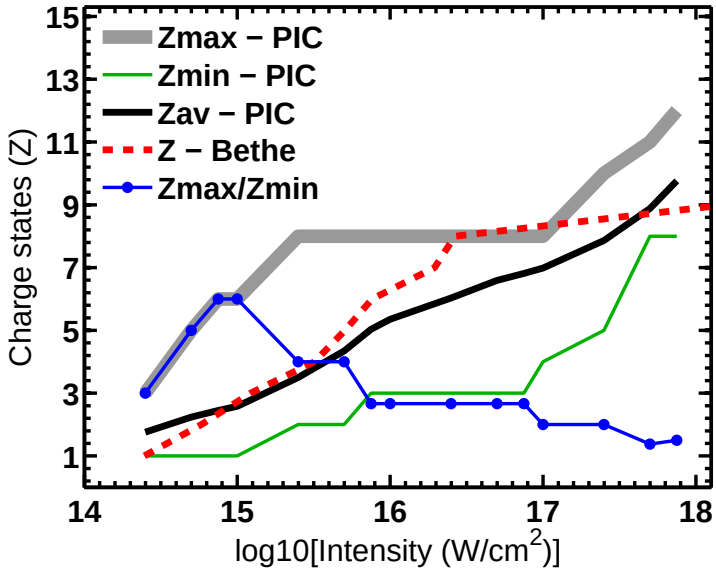

Figure 4.3: Maximum ion charge $\mathcal{Z}_{\mathrm{max}}$ (thick solid), minimum ion charge $\mathcal{Z}_{\mathrm{min}}$ (thin solid), average ion charge $\mathcal{Z}_{\mathrm{av}}$ (bold black) and the ion charge predicted by the Bethe rule [OFI, dashed, Eq. (4.1)] vs peak laser intensities for an Ar_{17256} cluster of radius $R = 6.2$ nm for an $n = 8$ cycle laser pulse $E_{\mathrm{l}}(t) = E_0 \sin^2(\omega_{\mathrm{l}} t/2n)\cos(\omega_{\mathrm{l}} t)$ of wavelength $\lambda_{\mathrm{l}} = 800$ nm.

intensity, at the end of the laser pulse. The ratio $\mathcal{Z}_{\max}/\mathcal{Z}_{\min}$ is also included in the plot. Ionization of the next inner atomic shell (e.g., $\mathcal{Z} > 8$) of argon would require a much higher field strength than those covered in Fig. 4.2. This is possible either by increasing the space charge field with a bigger cluster or by increasing the laser field strength. For the cluster considered above, a further increase of the laser intensity does not increase the highest charge state at the cluster boundary immediately but more and more ions from the cluster boundary to the cluster center achieve higher charge states $\mathcal{Z} \leq 8$. This is clearly visible in Fig. 4.3 between laser intensities $2.5 \times 10^{15}\text{Wcm}^{-2}$ – 10^{17}Wcm^{-2} where $\mathcal{Z}_{\max} = 8$ remains unchanged but $\mathcal{Z}_{\text{av}}$ increases. In the atomic case, one would expect all ions having $\mathcal{Z} = 8$ at an intensity 10^{17}Wcm^{-2}. Instead Fig. 4.3 shows ions with charge states $\mathcal{Z} = 7 - 3$ towards the cluster center. This we call "ionization depletion" because of the space charge field strongly counteracting the laser field. At the higher intensity $2.5 \times 10^{17}\text{Wcm}^{-2}$ the maximum charge state is $\mathcal{Z} = 10$ which would require an order of magnitude higher intensity $\approx 2.1 \times 10^{18}\text{Wcm}^{-2}$ in the atomic case (OFI) and, indeed, $\mathcal{Z}_{\max}$, $\mathcal{Z}_{\min}$ and $\mathcal{Z}_{\text{av}}$ sharply increase after the intensity $2.5 \times 10^{17}\text{Wcm}^{-2}$.

From the above described scenario it is clear that ionization ignition is indeed the mechanism by which cluster ions achieve the charge states higher than in the atomic ionization case at a given laser intensity. Also there are laser intensities at which ionization ignition saturates due to the high binding potential of inner electrons. Close to those saturation intensities ionization depletion is effective. The maximum charge state $\mathcal{Z}_{\max}$ appears at the cluster boundary while the minimum charge state $\mathcal{Z}_{\min}$ appears at the cluster center. The ionization model presented in Ref. [86] shows that the ratio $\mathcal{Z}_{\max}/\mathcal{Z}_{\min}$ lies between $1.5 - 2$ which agrees well with our results above the intensity 10^{16}Wcm^{-2}. However, $\mathcal{Z}_{\max}/\mathcal{Z}_{\min}$ exceeds the limit $1.5 - 2$ below the intensity 10^{16}Wcm^{-2} (as seen in Fig. 4.3) where ionization ignition is very efficient.

4.2.2 Charge states and energy distribution of ions

Figures 4.4a,b show the charge states and kinetic energies carried by different ion populations N_{ion} after laser pulses of different intensities for an Ar_{17256} cluster of radius $R = 6.2$ nm. Figure 4.4a shows a maximum charge $\mathcal{Z}_{\max} = 8$ and a minimum charge $\mathcal{Z}_{\min} = 4$ at an intensity 10^{17}Wcm^{-2} (also visible in Fig. 4.3). Ions with $\mathcal{Z}_{\max} = 8$ are driven with appreciable kinetic energies up to 25 keV while the other ions remain cold. Figure 4.4b shows ions with $\mathcal{Z}_{\max} = 12$ and $\mathcal{Z}_{\min} = 8$ at a higher laser intensity $7.5 \times 10^{17}\text{Wcm}^{-2}$. The ions possess kinetic energies ranging from 40 keV (ions with $\mathcal{Z}_{\min} = 8$) to 210 keV (ions with $\mathcal{Z}_{\max} = 12$). Figure 4.4c is the result (analogous to Fig. 4.4b) for an Ar_{92056} cluster (radius $R = 10.85$ nm) where the maximum ion energy is more than 400 keV (for $\mathcal{Z} = 14$). The higher charge states and the higher kinetic energies of ions for the bigger cluster (Fig. 4.4c) are consequences of enhanced ionization ignition. It should be noted that as the peak laser intensity is increased both OFI and the ion motion start earlier. If the ion dynamics is followed for a longer time all the potential energy of the cluster will ultimately be converted into the kinetic energy of ions and the final kinetic energy of ions will be much higher than those shown in Fig. 4.4a-c. The ion with maximum charge state $\mathcal{Z}_{\max}$ carries maximum energy at a given laser intensity.

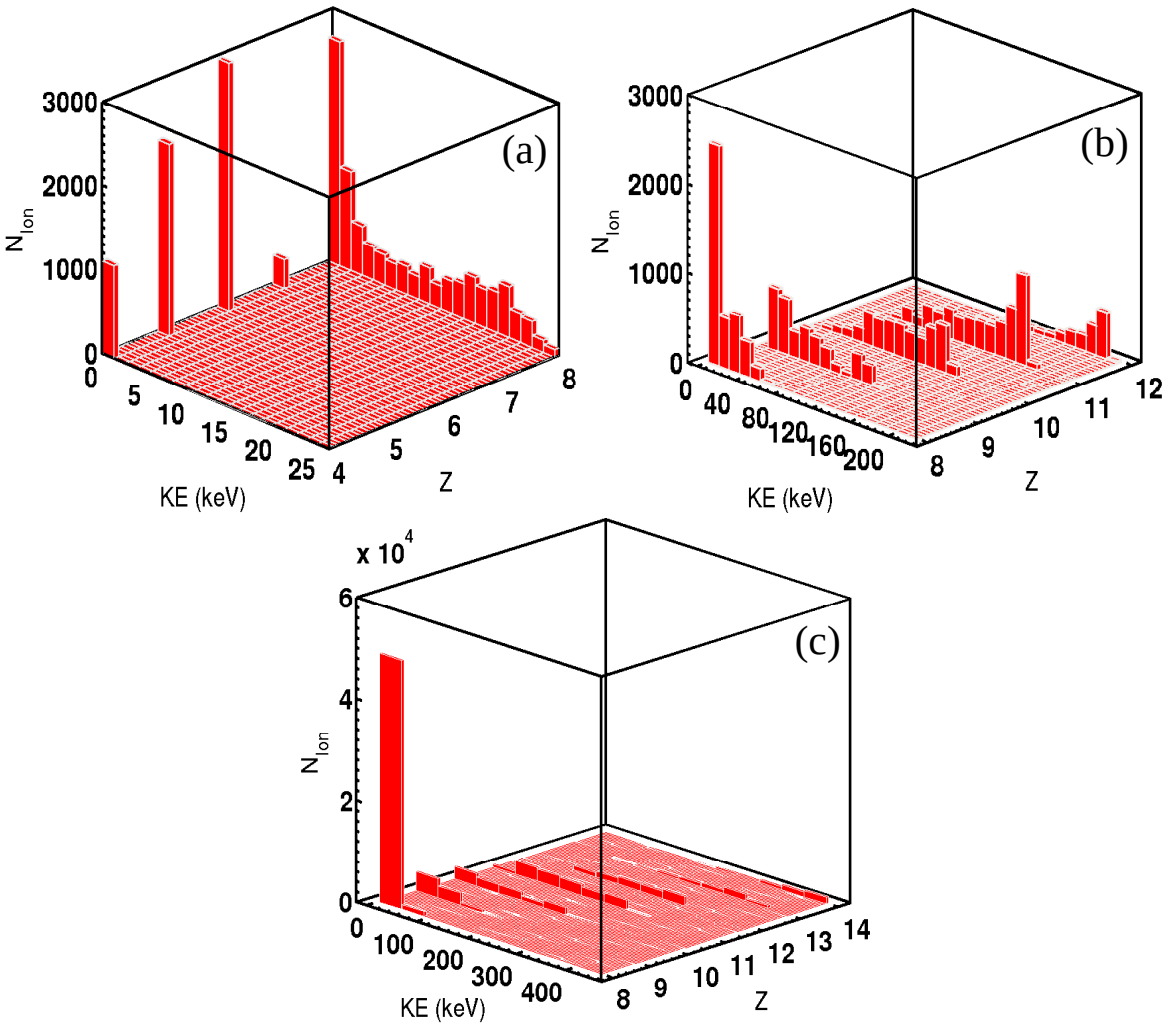

Figure 4.4: Kinetic energy and charge ($\mathcal{Z}$) distribution of ions for an Ar_{17256} cluster ($R = 6.2$ nm) irradiated by intensities (a) 10^{17}Wcm^{-2} (b) 7.5×10^{17}Wcm^{-2}. (c) Result for an Ar_{92096} cluster ($R = 10.85$ nm) at an intensity 7.5×10^{17}Wcm^{-2}. An $n = 8$ cycle pulse $E_l(t) = E_0 \sin^2(\omega_l t/2n)\cos(\omega_l t)$ of wavelength $\lambda_l = 800$ nm is applied in all cases.

Figure 4.5 shows maximum ion energy $K_{\max}$, minimum ion energy $K_{\min}$ and average ion energy $K_{\rm av}$ (defined as the sum of the kinetic energy of all ions divided by the number of ions $N = 17256$) vs peak laser intensities (after the laser pulses) for the Ar_{17256} cluster. $K_{\max}$ varies between $0 - 210$ keV in the intensity range $2.5 \times 10^{14} - 7.5 \times 10^{17}$Wcm^{-2}. The energy is carried mainly by the ions at the boundary of the cluster which also have maximum charge states $\mathcal{Z}_{\max}$. Less mobile ions in the central region of the cluster acquire the minimum energy $K_{\min}$ and also minimum charge state $\mathcal{Z}_{\min}$ (visible in Fig. 4.4). The average energy $K_{\rm av}$ goes up to 100 keV at the intensity 7.5×10^{17}Wcm^{-2} after the pulse.

In Fig. 4.6a-c we plot the distribution of the total kinetic energy, and the x, y and z-components (i.e., $\sum_{i=1}^{N} MV_{ix}^2/2, \sum_{i=1}^{N} MV_{iy}^2/2, \sum_{i=1}^{N} MV_{iz}^2/2$) of the total kinetic energy corresponding to Fig. 4.4a-c. Our purpose is to show the directional asymmetry in the ion energy distribution. In all cases ions moving along the laser polarization (the x-

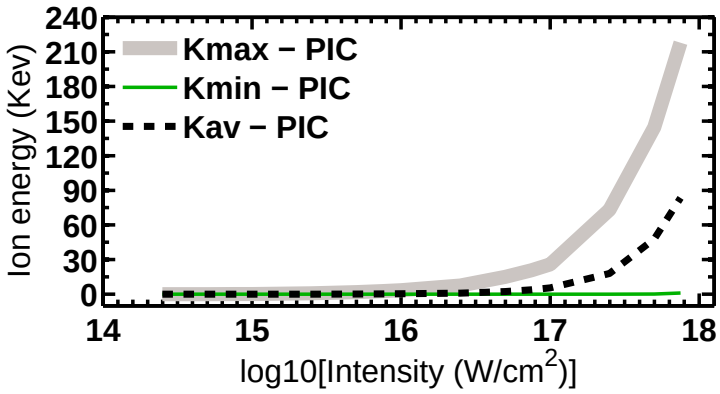

Figure 4.5: Maximum ion energy $K_{\max}$, minimum ion energy $K_{\min}$ and the average ion energy K_{av} immediately after the laser pulse for the Ar_{17256} cluster of Fig. 4.4. Laser pulse is same as in Fig. 4.4.

component) have higher kinetic energies than in the transverse directions. Moreover, y and z-components of energy are exactly the same. For longer laser pulses, a similar asymmetry in the ion energy distribution was reported in the experiments [37,57] with argon clusters, xenon clusters [80], and also in MD simulations of small rare-gas clusters [13] where the asymmetry in the ion charge distribution (as in Fig. 4.2) was made responsible for the asymmetric ion energy distribution. We shall show later that it is not only the charge asymmetry of the ions that is responsible for the energy asymmetry. The asymmetry in the ion energy components exists even for deuterium clusters (presented in Sec. 4.3) where both ion charge asymmetry and ionization ignition are absent. The asymmetric electron motion in a linearly polarized laser field also causes asymmetric ion energy distributions.

4.2.3 Expansion of clusters

The origin of energetic ions as describe in the previous section is a consequence of the cluster expansion that depends upon the charge distribution of the ions as well as the number of electrons that stay inside or in the vicinity of the cluster. The electrons inside lower the net positive charge and slow down the expansion. The asymmetric oscillation of the bound electrons result in a net effective positive charge along the laser polarization different from the transverse directions. The electrons just outside the cluster may also drag ions with them [6]. However, due to the high ion to electron mass ratio this process is not significant.

Figure 4.7a shows the normalized expansion radius R_x/R along the laser polarization, expansion radii $R_y/R, R_z/R$ (i.e., along y and z) normal to the laser polarization direction and the resultant expansion radius $R_{\max}/R = \sqrt{R_x^2 + R_y^2 + R_z^2}/R$ (for the Ar_{17256} cluster) after the pulse of different peak intensities. One sees that the cluster expands along x faster than in the y and z direction. The expansions along y and z are symmetric. These results have a clear correspondence with the results in Fig. 4.5 and 4.6. The maximum kinetic energy $K_{\max}$ in Fig. 4.5 is those of the ions with the maximum excursion $R_{\max}/R$ in Fig. 4.7a.

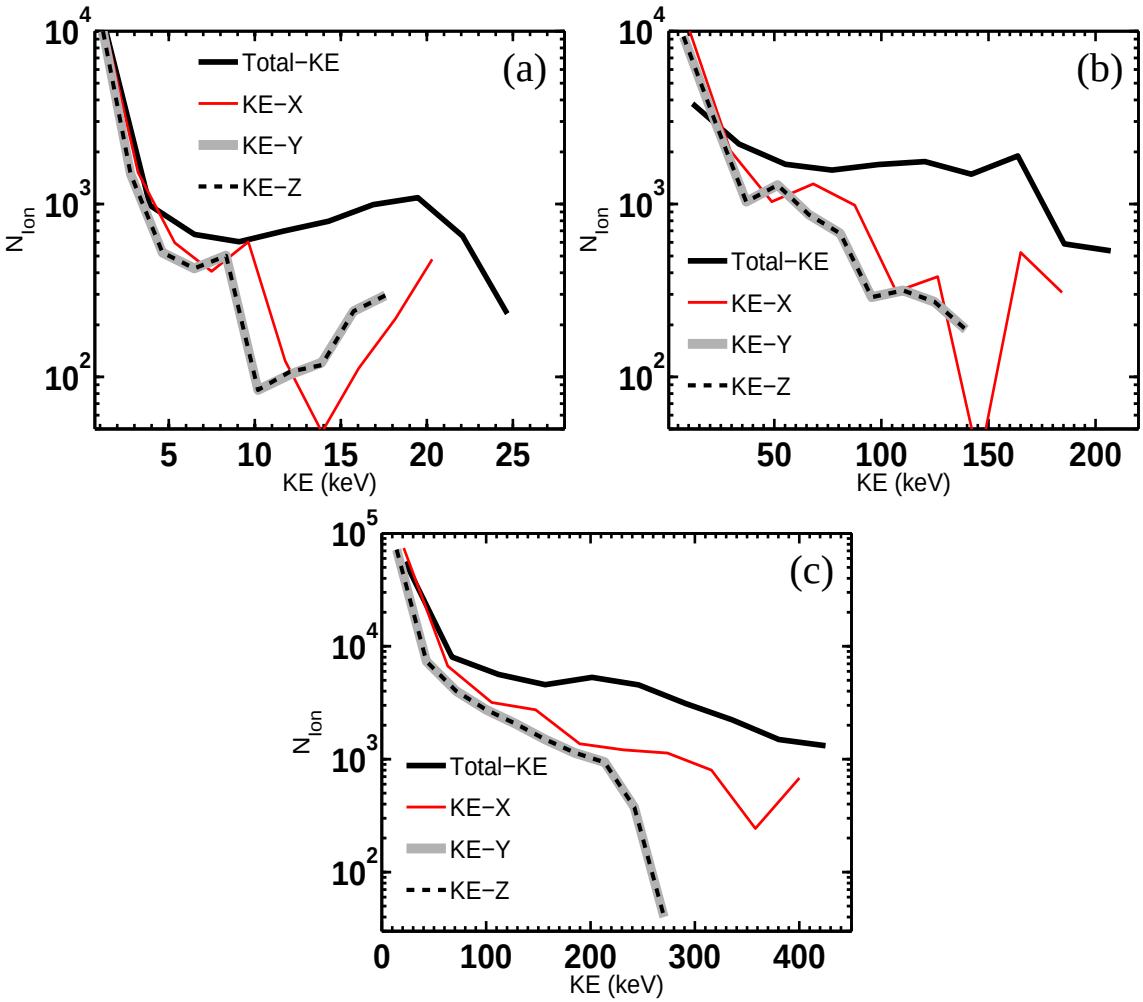

Figure 4.6: Kinetic energy distributions of ions for an Ar_{17256} cluster irradiated by intensities (a) 10^{17}Wcm^{-2} (b) 7.5×10^{17}Wcm^{-2} and (c) an Ar_{92096} cluster at an intensity 7.5×10^{17}Wcm^{-2}. In all cases the x-component of the energy is higher than y and z-components (which are identical). Other parameters are as in Fig. 4.4.

The expansion of a cluster also depends upon the number of electrons inside the cluster. Figure 4.7b shows the normalized electron number N_e/N within different radii R_{max}, $2R_{max}$ and $5R_{max}$ after laser pulses of various intensities. N_e/N within different R_{max} increases with increasing laser intensity due to the inner ionization up to a maximum $N_e/N \approx 4$, then decreases because a larger number of electrons leave the spheres of those radii than produced further by inner ionization. For laser intensities 10^{16}Wcm^{-2} – 7.5×10^{16}Wcm^{-2} one sees $N_e/N \approx 4$ i.e., $N_e \approx 69000$ electrons within the expanded cluster after the laser pulse. In the above range of intensities ionization ignition is not so efficient, which is also clear from Fig. 4.3. At the higher intensity 7.5×10^{17}Wcm^{-2}, N_e/N decreases to the value $N_e/N \approx 1$ i.e., $N_e \approx 17256$ electrons stay inside R_{max}. Almost the same number of electrons stay within R_{max}, $2R_{max}$ and $5R_{max}$. This means that accumulation of electrons in the cluster vicinity does not occur and ions cannot be dragged by electrons.

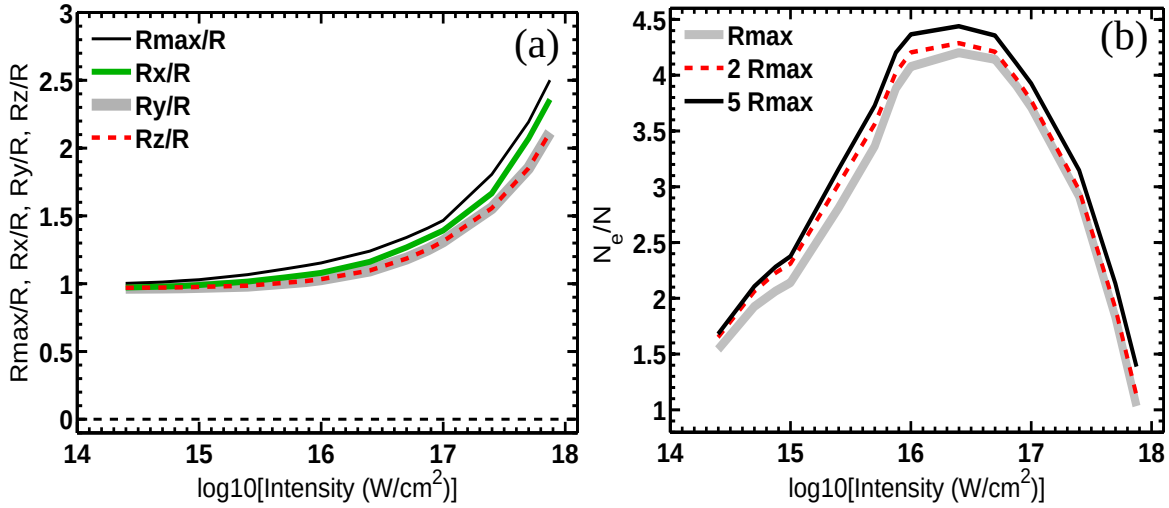

Figure 4.7: (a) Normalized expansion radius R_x/R along the laser polarization, expansion radius $R_y/R, R_z/R$ normal to the laser polarization and the resultant expansion radius $R_{\max}/R = \sqrt{R_x^2 + R_y^2 + R_z^2}/R$ vs the peak laser intensity. (b) Normalized electron number N_e/N within different radii $R_{\max}, 2R_{\max}$ and $5R_{\max}$ vs the peak laser intensity. Data points are plotted after the pulse for an Ar_{17256} cluster. Laser pulse is same as in Fig. 4.1.

From the above results it is clear that the expansion process of a cluster is mainly due to Coulomb expansion. This can be justified by comparing our results with a simplified model [6]. According to this model a homogeneous positively charged sphere with total charge Q_p, initial radius R_0 and mass M_p expands electrostatically as

$$\ddot{R} = \frac{Q_p}{M_p R^2}. \tag{4.4}$$

Here, $R(t)$ is the instantaneous radius. The implicit solution of Eq. (4.4) with the initial conditions $R(t_{in}) = R_0$ and $\dot{R}(t_{in}) = 0$ reads

$$t = t_{in} + \sqrt{\frac{M_p R_0^3}{2Q_p^2}} \left(\sqrt{p^2 - p} + \log(\sqrt{p} + \sqrt{p-1}) \right), \tag{4.5}$$

with t_{in} the initial time and $p = R(t)/R_0$. This model does not consider the presence of electrons within the expanding cluster. Also it assumes that the total positive charge is constant (absence of inner ionization). In a realistic simulation (e.g., PIC or MD) part of the positive ion background may be compensated by the electrons (if not all electrons leave the cluster). During the pulse inner ionization changes the total charge of the ionic background. With increasing peak laser intensity inner ionization as well as the cluster expansion starts at smaller t_{in}. In spite of these differences, Eq. (4.4) is useful to understand the cluster expansion. Equation (4.5) requires two input parameters: the net positive charge Q_p and the initial time t_{in} which are *a priori* unknown. The net positive charge of the cluster depends on the number of electrons N_e inside the cluster. The total ion charge $N\mathcal{Z}_{av}$ (see Fig. 4.3) and the number N_e (see Fig. 4.7) after the laser pulse are

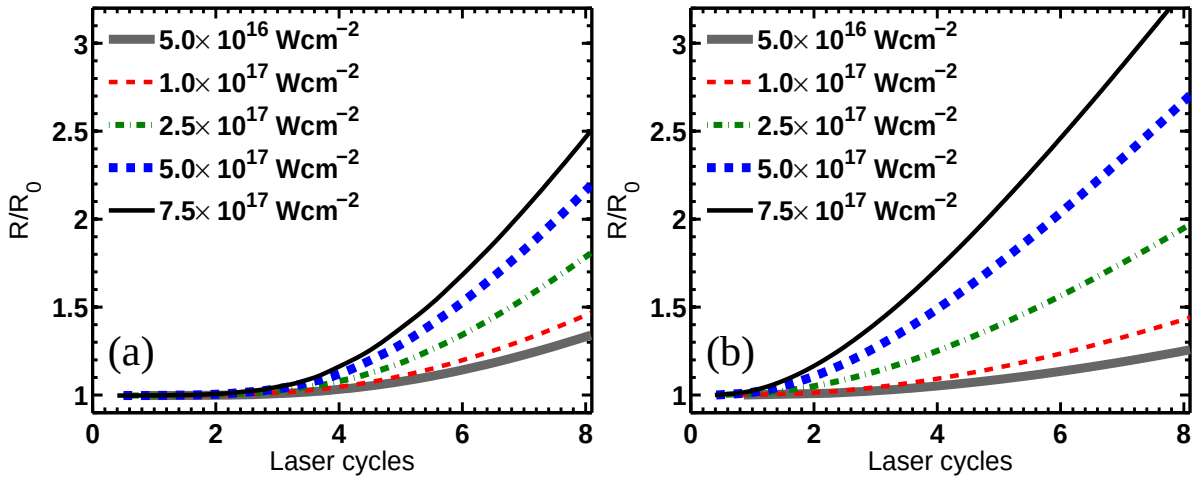

Figure 4.8: Normalized radius $R(t)/R_0$ of the cluster vs time in laser cycles at different peak laser intensities. (a) PIC and (b) model Eq. (4.4) results. Laser pulse and cluster parameters are as in Fig. 4.1.

known from the PIC simulation. We assume $Q_\mathrm{p} = N\mathcal{Z}_\mathrm{av} - Q_\mathrm{e}$ at the initial time t_in. The initial time t_in is adjusted to the time when the first electrons are removed from the cluster atoms.

Figure 4.8 shows the normalized cluster radius $R(t)/R_0$ vs time at different laser intensities. Figure 4.8a is the self-consistent PIC result while Fig. 4.8b is calculated with the model assuming a constant Q_p (in time) that depends only on the laser intensity. The model agrees well with the PIC results at intensities $< 10^{17}\mathrm{Wcm}^{-2}$. This shows that Coulomb expansion is the dominant process. For laser intensities $> 10^{17}\mathrm{Wcm}^{-2}$ expansion is much faster according to the model (4.5) compared to the PIC results shown. This is due to the assumption of the constant value of the total charge Q_p and the absence of inner ionization in the model. Moreover in the case of PIC simulations the cluster expands asymmetrically, and this asymmetry increases at higher laser intensities (as is clear from Fig. 4.7a). From the comparison between the model and the PIC results we conclude that expansion of clusters is mainly due to the Coulomb repulsion between the highly charged ions. Hydrodynamic expansion is not important for the laser and cluster parameters under study.

The expansion of a cluster and the inner ionization at a given laser intensity together define the Mie-resonance frequency $\omega_\mathrm{Mie}(t) = \sqrt{4\pi\rho(t)/3}$ of a cluster as long as the charge density $\rho(t)$ is homogeneous. If $\omega_\mathrm{Mie}(t)$ meets the laser frequency during the expansion the well-known linear resonance occurs at which energy absorption is efficient. At a lower laser intensity and for a short laser pulse, the cluster radius remains close to its initial value $R_0 = R(0)$. With increasing laser intensity the outer layer of a cluster moves faster while the inner core maintains an approximate charge homogeneity. At this point one underestimates the Mie-frequency by the definition $\omega_\mathrm{Mie}(t) \equiv \sqrt{Q(t)/R(t)^3} = \sqrt{4\pi\rho(t)/3}$ with $Q(t)$ the total charge within the expanding radius $R(t) = R_\mathrm{max}(t)$. From PIC simulations we find that the charge homogeneity is almost always satisfied within the initial cluster radius R_0. We therefore define $\omega_\mathrm{Mie}(t) \equiv \sqrt{Q_\mathrm{b}(t)/R_0^3}$ with the total ionic

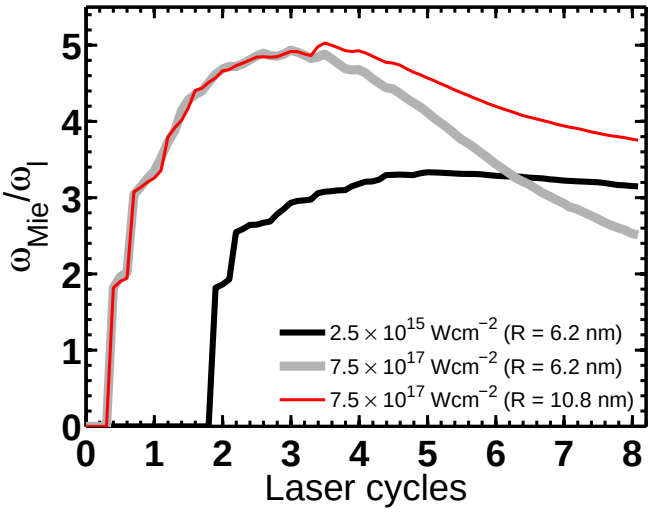

Figure 4.9: Scaled Mie-resonance frequency $\omega_{\rm Mie}/\omega_{\rm l}$ vs time (in units of laser cycles) at different laser intensities 2.5×10^{15}Wcm^{-2}, 7.5×10^{17}Wcm^{-2} for the Ar_{17256} cluster and for the Ar_{92096} cluster at an intensity 7.5×10^{17}Wcm^{-2}. Laser pulse is same as in Fig. 4.1.

charge $Q_{\rm b}(t)$ within R_0 where a deeply bound electron cloud collectively oscillates with $\omega_{\rm Mie}(t)$. This approximation resembles the cold electron core discussed in Ref. [87].

Figure 4.9 shows the calculated and scaled Mie-frequency $\omega_{\rm Mie}(t)/\omega_{\rm l}$ vs time (in units of laser cycles) at different laser intensities 2.5×10^{15}Wcm^{-2}, 7.5×10^{17}Wcm^{-2} for the Ar_{17256} cluster and for the Ar_{92096} cluster at an intensity 7.5×10^{17}Wcm^{-2}. At the intensity 2.5×10^{15}Wcm^{-2} OFI starts near two cycles where $\omega_{\rm Mie}(t)/\omega_{\rm l}$ sharply rises up to the third harmonic of the laser frequency near 3 cycles and reaches a maximum near 5 cycles. After the maximum $\omega_{\rm Mie}(t)/\omega_{\rm l}$ decreases very slowly due to the cluster expansion. At a higher intensity 7.5×10^{17}Wcm^{-2} OFI starts earlier but at the same time for the Ar_{17256} and Ar_{92096} clusters. $\omega_{\rm Mie}(t)/\omega_{\rm l}$ increases up to the fifth harmonic near 3 cycles for both clusters. After that $\omega_{\rm Mie}(t)/\omega_{\rm l}$ decreases much faster for the smaller cluster down to a value above the second harmonic at the end of the 8th cycle. For the bigger cluster $\omega_{\rm Mie}(t)/\omega_{\rm l}$ decreases much slower owing to a slower expansion and reaches just below the fourth harmonic of the laser frequency after the end of the pulse. The slower decrease of $\omega_{\rm Mie}(t)/\omega_{\rm l}$ for the bigger cluster is due to the presence of a large number of electrons inside the cluster. However, Fig. 4.9 clearly shows that linear resonance $\omega_{\rm Mie}(t) = \omega_{\rm l}$ does not occur during the expansion with the short pulses considered in the present study. Nonetheless, a significant fraction of the electrons leave the cluster completely (Fig. 4.7b) by absorbing energy from the laser field. We shall show that energy absorption by electrons is still very efficient *even* in the absence of linear resonance.

4.2.4 Energy absorption by electrons

We shall now discuss the electron dynamics. The enhancement of ionic charge sates and ion kinetic energies presented in the earlier sections are the consequences of electron re-

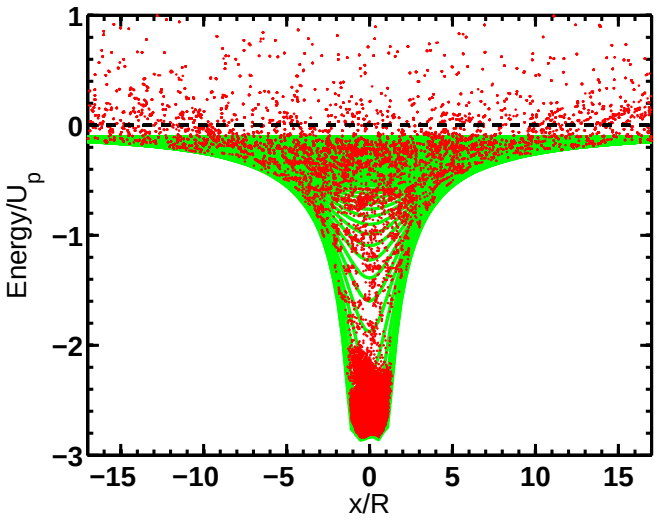

Figure 4.10: Total energy of individual PIC electrons $E_{\rm tot} = \dot{\boldsymbol{r}}_i^2/2 - \Phi_i$ (dots) in units of the ponderomotive energy $U_{\rm p}$ vs their excursions x (in units of R) along the laser polarization direction after a laser pulse of intensity $5.0 \times 10^{16}\mathrm{Wcm}^{-2}$. The dashed line represents $E_{\rm tot} = 0$. Only electrons within the computational box are plotted. The cluster and laser parameters are as in Fig. 4.1. The continuous lines (solid) represent the net effective potential after the pulse in a xy-plane (i.e., for a cut $z = 0$ and various y-values). The lowest line represents the potential in the plane $(y, z) = (0, 0)$.

moval from the cluster. Therefore it is necessary to understand the laser energy absorption by the electrons, leading to subsequent heating and outer ionization. For small clusters we showed in chapter 3 that nonlinear resonance (NLR) is the dominant collisionless absorption mechanism for near-infrared short laser pulses. The ions were assumed immobile with fixed charge states. In the present work we consider mobile ions with self-consistent inner ionization where the linear resonance $\omega_{\rm Mie} = \omega_{\rm l}$ is not met (as seen in Fig. 4.9) during the pulse. We show that NLR is a robust phenomenon also under these more realistic conditions.

Electron energy spectra

In Fig. 4.10, the total energy of individual PIC electrons $E_{\rm tot} = \dot{\boldsymbol{r}}_i^2/2 - \Phi_i$ (kinetic plus potential energy) in units of the ponderomotive energy $U_{\rm p}$ vs their excursion x (in units of R) along the laser polarization direction after a laser pulse of intensity $5.0 \times 10^{16}\mathrm{Wcm}^{-2}$ is plotted. The dashed line represents $E_{\rm tot} = 0$. We only plot the electrons within the computational box. Some of the electrons may have higher energies and larger excursions than plotted in Fig. 4.10. As ionization proceeds a potential builds up and electrons move on different potential curves. The solid lines are the effective potential (due to the expanding ions and electrons) curves after the pulse for a cut $z = 0$ and various y-values. The lowest line represents the potential in a plane $(y, z) = (0, 0)$. One sees that after the pulse many electrons are bound deep inside the potential. They form a spherical electron cloud at the center of the cluster due to which the Coulomb expansion is slowed

down compared to the case where the electrons are completely stripped off. Those tightly bound electrons oscillate with ω_{Mie} in an (almost) harmonic potential. Other electrons are less tightly bound and are located along shallower potential curves. At the boundary of the computational box the potential is negative due to the monopole potential boundary condition. The electrons having energies close to the value $E_{\mathrm{tot}} = 0$ may be regarded as quasi-free electrons. We define an electron as being outer ionized if its energy $E_{\mathrm{tot}} > 0$. Within the simulation box the maximum electron energy is approximately $E_{\mathrm{tot}} \approx U_{\mathrm{p}}$, which is 2.98 keV at the above laser intensity. The electrons with excursions larger than the size of the computational box may have even higher energies.

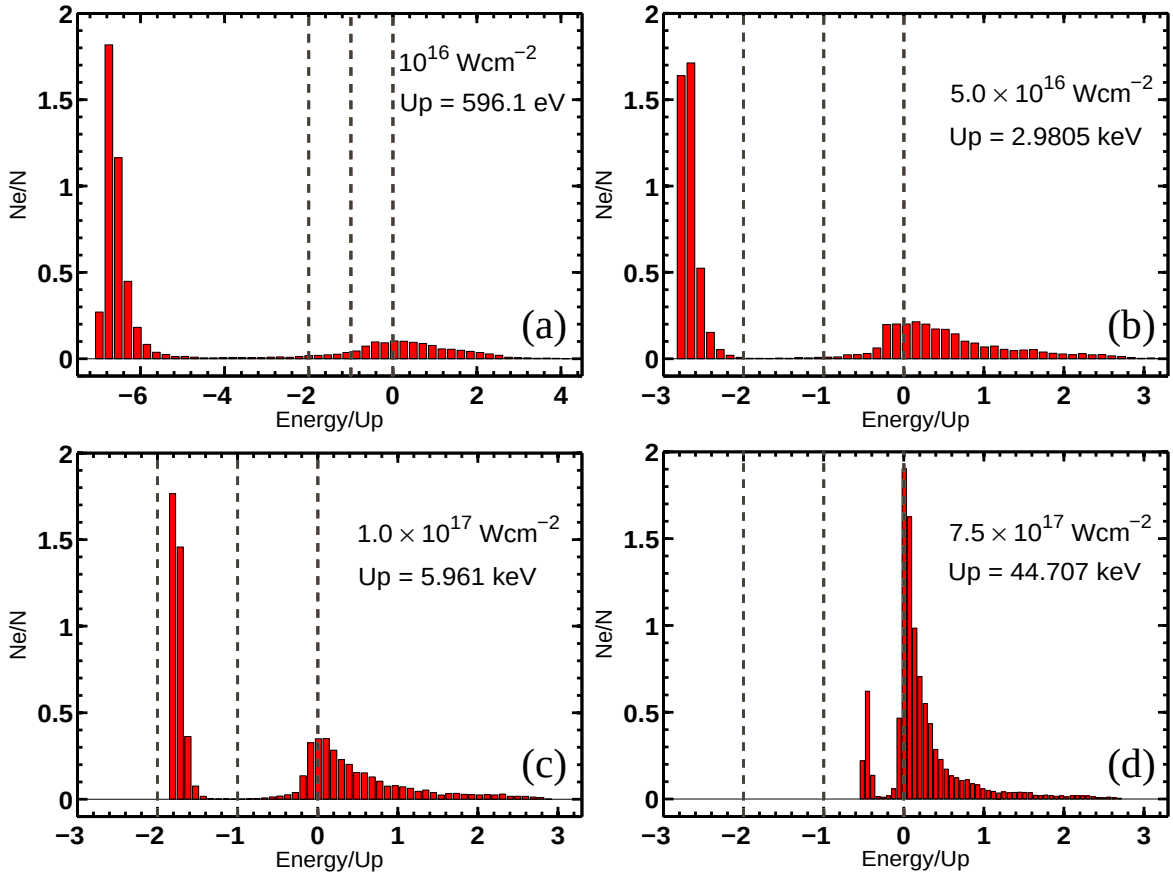

Figure 4.11: Electron energy distribution after the laser pulse of respective laser intensities (a) 1.0×10^{16}, (b) 5.0×10^{16}, (c) 1.0×10^{17} and (d) $7.5\times10^{17}\mathrm{Wcm}^{-2}$ for an Ar_N ($N = 17256$) cluster (with same laser pulse as in Fig. 4.1).

Figure 4.11 shows the electron energy distributions for an Ar_{17256} cluster at laser intensities $1.0\times10^{16}\mathrm{Wcm}^{-2}$, $5.0\times10^{16}\mathrm{Wcm}^{-2}$, $1.0\times10^{17}\mathrm{Wcm}^{-2}$, and $7.5\times10^{17}\mathrm{Wcm}^{-2}$ after the pulse. It is clearly seen that after the laser pulse a large fraction of the electrons has negative energy. Those electrons remain bound inside the potential and stay rather cold (narrow energy distribution). The electrons with $E_{\mathrm{tot}} > 0$ are the outer ionized electrons which are freed from the cluster potential. Those free electrons carry typically keV energies, as measured in experiments. With increasing intensity a higher fraction of electrons gain positive energy (Figs. 4.11c,d) and more electrons are "generated" by increased inner

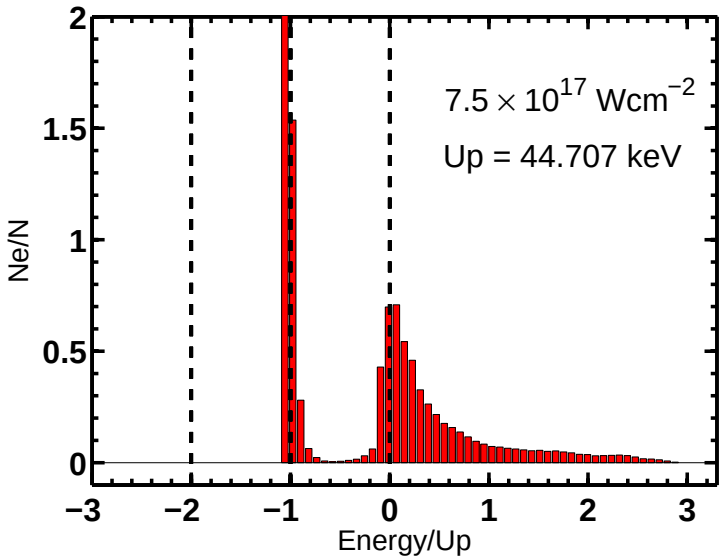

Figure 4.12: Electron energy distribution at $7.5 \times 10^{17}\mathrm{Wcm}^{-2}$ for an Ar_N ($N = 92096$) cluster (laser pulse same as in Fig. 4.1).

ionization. There is also a group of electrons very close to the continuum (i.e., $E_{\mathrm{tot}} = 0$) but still negative total energy. Those electrons are sometimes called *halo*. Figure 4.11 shows maximum electron energies around $3U_{\mathrm{p}}$ corresponding to $2, 10, 20$ and 135 keV at the laser intensities (a) $1.0 \times 10^{16}\mathrm{Wcm}^{-2}$, (b) $5.0 \times 10^{16}\mathrm{Wcm}^{-2}$, (c) $1.0 \times 10^{17}\mathrm{Wcm}^{-2}$, and (d) $7.5 \times 10^{17}\mathrm{Wcm}^{-2}$, respectively.

Figure 4.12 shows electron energy spectra for a bigger Ar_{92096} cluster ($N = 92096$ atoms) at an intensity $7.5 \times 10^{17}\mathrm{Wcm}^{-2}$. In this case the maximum electron energy is also $\simeq 3U_{\mathrm{p}}$, but the electron yield is higher due to the higher number of electrons in the Ar_{92096} cluster. Most of the experiments employing longer laser pulses above 100 fs report electron energies from keV to a few tens of keV. Recent experiments [82] with 28 fs, 820 nm Ti:Shaphire laser pulses reported electrons above 100 keV with argon and xenon clusters. Our simulations confirm these findings.

Mechanism of the energy absorption

In chapter 3 we clearly showed that electrons absorb energy predominantly by NLR. Electrons oscillating at different potential levels (as in Fig. 4.10) during the pulse experience different restoring forces. Therefore each electron "sees" a different effective frequency ω_{eff} and escapes at different times by meeting the NLR. We identify the NLR for all PIC electrons as it was done in chapter 3.

For an Ar_{17256} cluster (as in Fig. 4.11) irradiated with an intensity $5.0 \times 10^{16}\,\mathrm{Wcm}^{-2}$, Fig. 4.13a–h shows $(\omega_{\mathrm{eff}}/\omega_{\mathrm{l}})^2$ of individual PIC electrons vs their energies $E_{\mathrm{tot}}(t) = \dot{\boldsymbol{r}}_i^2(t)/2 - \Phi(\boldsymbol{r}_i, t)$ at times $t = 1.0,\ 2.0,\ 2.5,\ 3.0,\ 4.0,\ 4.5,\ 5.0$ and 6.0 cycles, respectively. At a time when, for a particular electron, E_{tot} becomes > 0 outer ionization occurs for that electron. Fig. 4.13a shows electrons after the OFI. At $t = 2.0, 2.5$-cycles

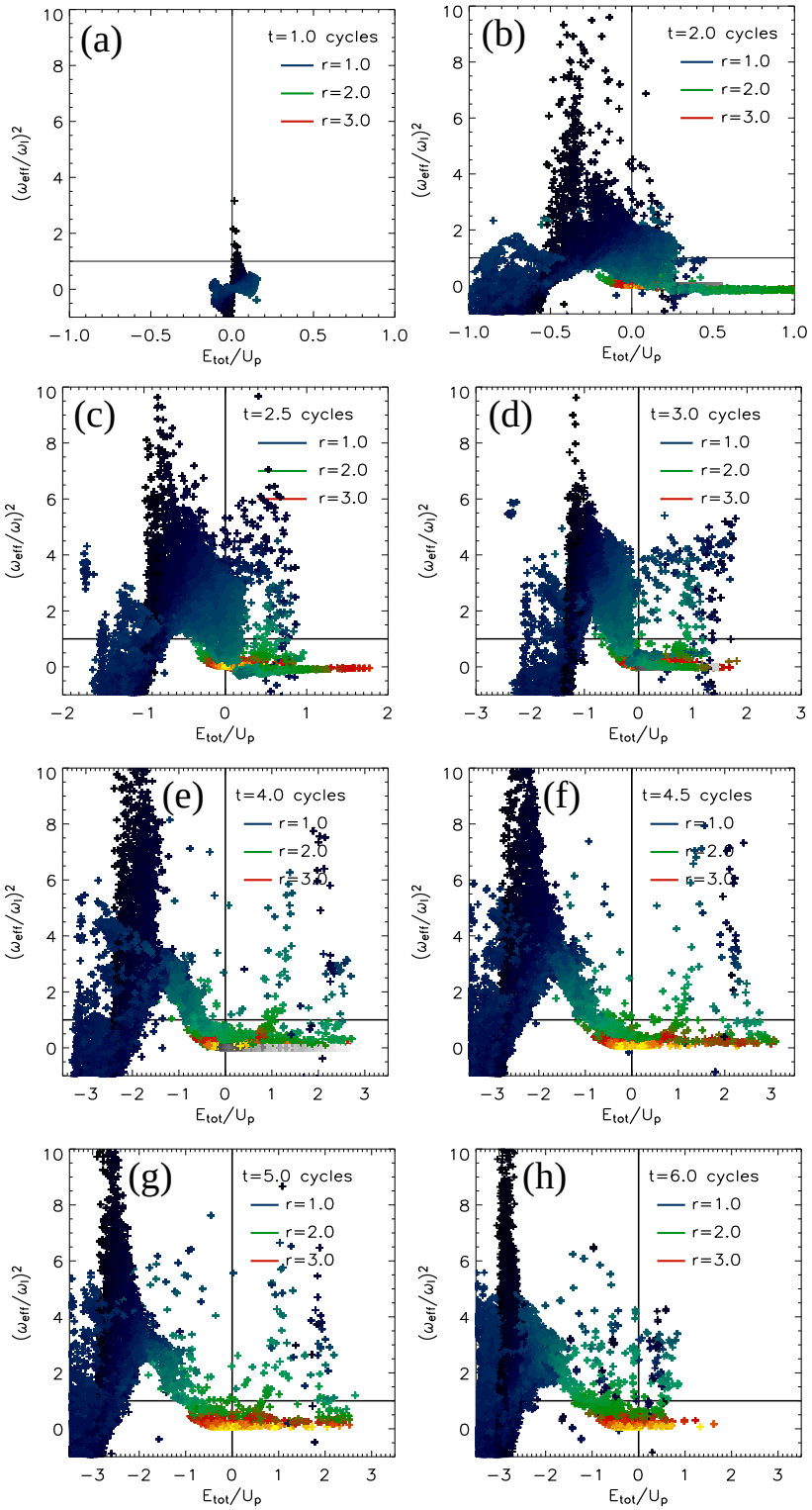

Figure 4.13: Snapshots of PIC electrons in the frequency vs energy-plane at times (a) $t = 1.0$, (b) $t = 2.0$, (c) $t = 2.5$, (d) $t = 3.0$, (e) $t = 4.0$, (f) $t = 4.5$, (g) $t = 5.0$, and (h) $t = 6.0$ laser cycles for laser intensity $5.0 \times 10^{16}\,\mathrm{Wcm}^{-2}$. Other parameters as in Fig. 4.1. The radial positions (in units of R) are color-coded. Electrons become free upon crossing the NLR.

(Figs. 4.13b,c) a large number of electrons is already produced due to inner ionization. NLR is less clear for these early leaving electrons (in Figs. 4.13a,b,c) since they move in a shallow effective potential and leave the cluster with positive but very small $E_{\rm tot}$ and $\omega_{\rm eff}^2 \simeq 0$. In chapter 3, for fixed ionic charge density, immobile ions and zero potential boundary condition it was shown that each electron reaches positive energy close to the point $(\omega_{\rm eff}^2/\omega_{\rm l}^2, E_{\rm tot}/U_{\rm p}) = (1, 0)$. This incidence is also seen in Figs. 4.13b-e. Additionally, $E_{\rm tot}/U_{\rm p}$ of some electrons shifts to negative values when NLR occurs. In fact, NLR actually occurs inside the potential when the energy changes sharply from negative to positive values (as seen in chapter 3) and particles leave the potential within less than one quarter of a laser cycle. For example, if some electrons with excursions between $2R - 5R$ in Fig. 4.10 are sharply pulled out by the NLR, an energy spreading up to $-U_{\rm p}$ is to be expected for those electrons that cross the NLR at different locations between $2R - 5R$. Figures 4.13c–f show that most of the electrons escape from the cluster by passing through the channel $(\omega_{\rm eff}^2/\omega_{\rm l}^2, E_{\rm tot}/U_{\rm p}) = (1, y)$ with $y \in [-U_{\rm p}, 0]$ at radii around $2R - 5R$. It is also visible that more and more electrons are driven to positive frequency before they leave the cluster by passing through $(\omega_{\rm eff}^2/\omega_{\rm l}^2, E_{\rm tot}/U_{\rm p}) = (1, y)$. As more and more electrons are freed, the remaining electrons experience predominantly the force by the ionic background, and they move deep into the potential where they experience a higher Mie-frequency. In Figs. 4.13c-h, the electrons with $E_{\rm tot} > 0$ but small radii are those driven back to the cluster by the laser field. After the peak of the laser pulse (Figs. 4.13g,h) the restoring force of the ions on the electrons dominates the laser force and the electrons move back towards the cluster center where they remain bound (see the highly confined electron cloud in Fig. 4.10). Although there is spreading of single particle energies $E_{\rm tot}$ near the point $(\omega_{\rm eff}^2/\omega_{\rm l}^2, E_{\rm tot}/U_{\rm p}) = (1, 0)$, the passage through the NLR, i.e., $\omega_{\rm eff}^2/\omega_{\rm l}^2 = 1$ is necessary for the outer ionization and the efficient energy absorption by electrons.

4.3 Results for deuterium clusters

Deuterium clusters have drawn considerable attention as a target to obtain highly energetic ions [88–94] that can drive nuclear fusion. Since a deuterium atom has only one electron, ionization ignition for deuterium clusters (as well as hydrogen clusters) cannot happen assuming all atoms being ionized at the same time by the laser field. The smaller Wigner-Seitz radius of a deuterium cluster compared to an argon cluster provides a higher charge density and a higher Mie-frequency than for a singly ionized argon cluster. Table 4.1 exemplifies the above mentioned scenario for a singly ionized argon cluster and a deuterium cluster for a laser wavelength $\lambda_{\rm l} = 800\,{\rm nm}$. The Mie-frequency of a deuterium cluster also drops much faster due to the faster expansion compared to an argon cluster consisting of much heavier nuclei. Therefore the linear resonance during expansion may be met for a deuterium cluster even during short laser pulses. The Mie-resonance with the fundamental laser frequency as well as with its harmonics has a significant effect on the energy absorption as well as harmonic radiation so that deuterium clusters are interesting targets.

Cluster type	Wigner Seitz radius $r_{\rm W}$ (nm)	Number of atoms N	Cluster radius $R = r_{\rm W}N^{1/3}$ (nm)	Atomic density $\rho = \frac{3N}{4\pi R^3}$ ($\rm m^{-3}$)	$\rho/\rho_{\rm c}$	$\omega_{\rm Mie}/\omega_{\rm l}$ $= \sqrt{\rho/3\rho_{\rm c}}$
$\rm Ar_N$	0.24	17256	6.2	1.73×10^{28}	9.9	1.82
$\rm D_N$	0.17	17256	4.39	4.86×10^{28}	27.86	3.05

Table 4.1: Comparison between an argon cluster and a deuterium cluster containing the same number of atom $N = 17256$. The critical density is $\rho_{\rm c} = 1.744 \times 10^{27}\rm m^{-3}$ for a laser pulse of wavelength 800 nm.

A recent experiment [41] with hydrogen clusters reported anisotropy in the ion energy distribution: ions along the direction of polarization of a linearly polarized field acquire higher energy than the ions moving in the directions transverse to the laser polarization. Such an anisotropy was previously reported in experiments [10,37,80] and simulations [13] with high $\mathcal{Z}$ rare-gas clusters where anisotropy of the energy distribution was attributed to the anisotropy of the ionic charges. We have also shown anisotropic ion dynamics for argon clusters previously in this chapter. However, the observed anisotropy in hydrogenic clusters cannot be due to the anisotropy of the ionic charges since there are only singly charged ions. In this case asymmetry in the energy distribution arises due to the asymmetric electron dynamics in the linearly polarized laser field.

We study two deuterium clusters ($\rm D_N$) of different number of atoms ($N = 17256$ and 103536) in the same laser pulse as considered before. The Wigner-Seitz radius of a deuterium cluster is $r_{\rm W} = 0.17$ nm (listed in Table 4.1), yielding respective cluster radii $R = 4.39$ nm and 7.98 nm.

4.3.1 Ion energy spectra

At first we present energy distributions of deuterium ions after laser pulses of different intensities. Figure 4.14 shows the number of deuterium ions vs their kinetic energies at laser intensities 2.5×10^{16}, 5.0×10^{16}, 7.5×10^{16}, and $1.0 \times 10^{17}\rm Wcm^{-2}$, respectively, for the $\rm D_N$ ($N = 17256$) cluster of radius $R = 4.39$ nm. With increasing laser intensity the maximum kinetic energy is seen to increase up to 2.5 keV at the intensity $10^{17}\rm Wcm^{-2}$. The higher the laser intensity is, the earlier sets in inner ionization as well as outer ionization. The latter thus triggers the Coulomb expansion earlier than at a lower laser intensity. As a result the potential energy of the cluster is converted faster to kinetic energy of the ions. Figure 4.14e shows the maximum kinetic energy $K_{\rm max}$, the minimum kinetic energy $K_{\rm min}$ and the average kinetic energy $K_{\rm av}$ for different peak intensities. Although $K_{\rm max}$ is up to 2.5 keV at the highest intensity plotted in Fig. 4.14d, $K_{\rm av}$ is < 1.6 keV. As pointed out before $K_{\rm min}$ is carried by the ions closer to the center. It is noticeable that $K_{\rm min}$ starts increasing at an intensity $\approx 5.0 \times 10^{16}\rm Wcm^{-2}$ due to the outward motion of those ions.

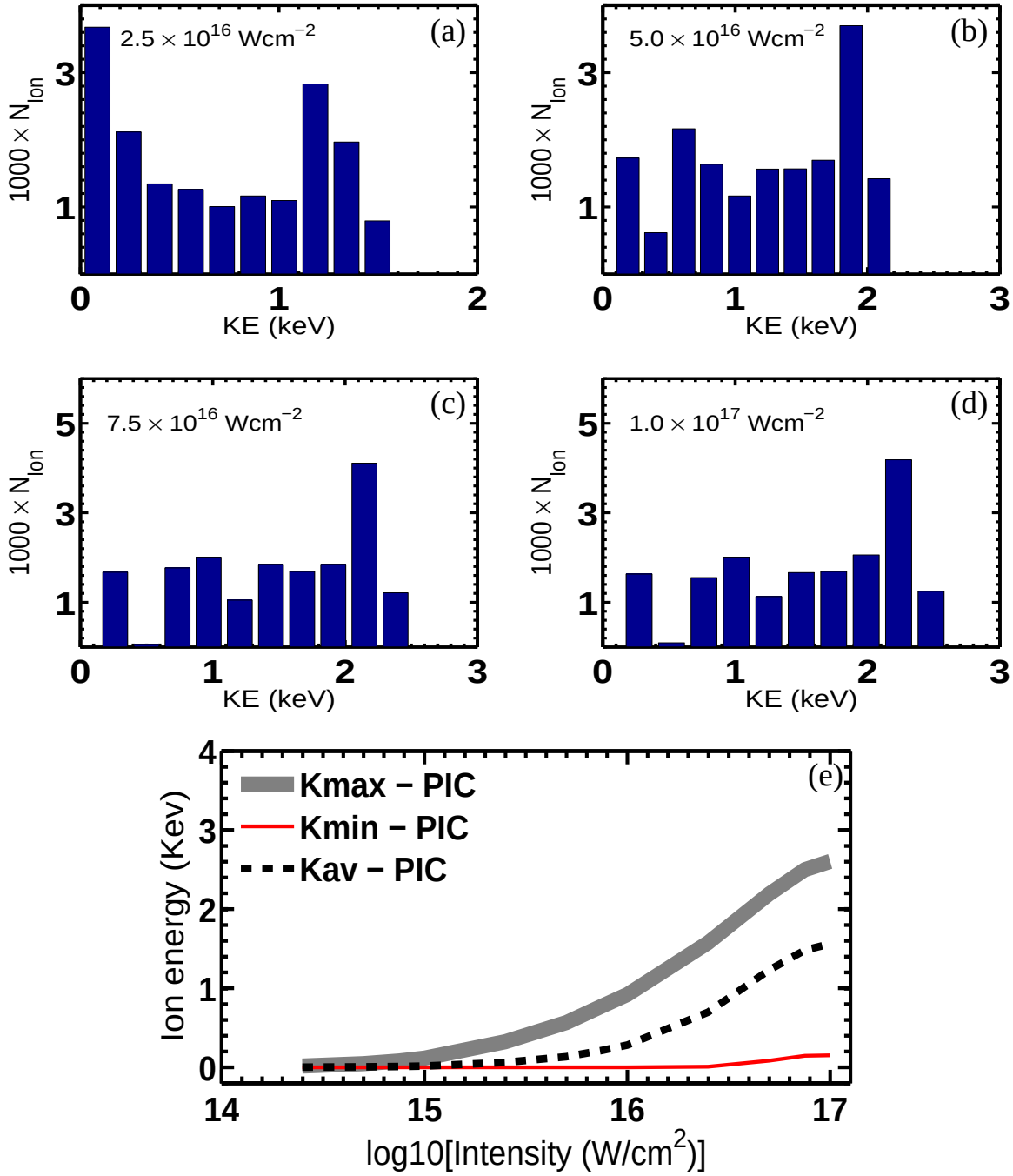

Figure 4.14: Kinetic energy distribution of deuterium ions for a D_{17256} cluster of radius $R = 4.39\,\text{nm}$ and an $n = 8$ cycle laser pulse $E_l(t) = E_0 \sin^2(\omega_l t/2n)\cos(\omega_l t)$ of different intensities (a) 2.5×10^{16}, (b) 5.0×10^{16}, (c) 7.5×10^{16}, and (d) $1.0 \times 10^{17}\text{Wcm}^{-2}$. The bottom figure (e) shows maximum kinetic energy K_{max}, minimum kinetic energy K_{min} and average kinetic energy K_{av} (total kinetic energy of all ions divided by the total number of ions) at different peak laser intensities after the laser pulse.

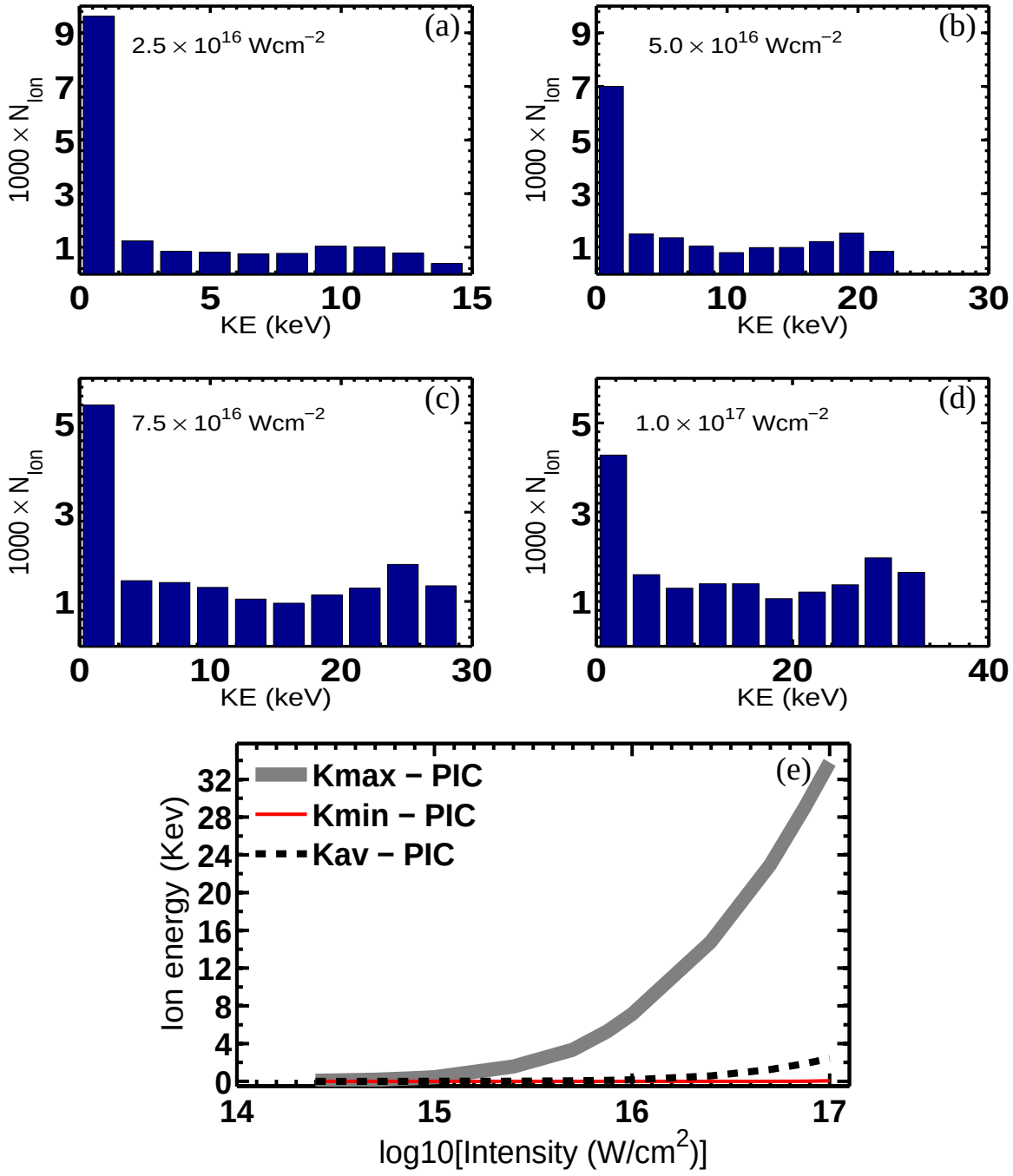

Figure 4.15: Same as Fig. 4.14 but for a bigger D_{103536} cluster ($R = 7.98\,\text{nm}$).

Figure 4.15a-e shows kinetic energy distributions of ions for the bigger deuterium cluster of radius 7.98 nm (number of atoms $N = 103536$) analogous to Fig.4.14a-e. The ions have much higher energies due to the higher potential energy in the bigger cluster. Maximum ion energies up to 34 keV (after the pulse) are seen in Fig. 4.14d. At the laser intensity $10^{17}\mathrm{Wcm}^{-2}$, Fig. 4.15e shows an average kinetic energy about 3 keV although the maximum ion energy is 34 keV. Since at a given laser intensity (e.g., $10^{17}\mathrm{Wcm}^{-2}$) a bigger cluster will retain more bound electrons (as shown below) than smaller ones, the inner core of the bigger cluster expands slower. As a result K_{av} does not grow at the same rate with the cluster size (as evident from Figs. 4.14e and 4.15e). Most of the experiments [88] reported maximum ion kinetic energies up to a few hundred keV or even MeV. However, the average kinetic energy was only a few tens of keV. The average proton energies obtained in experiments and simulations [41, 95–97] with hydrogen clusters of radii $R < 10$ nm was < 10 keV.

The above results can be easily understood considering a simple Coulomb expansion model [95, 96] assuming all electrons being outer ionized by the laser field, leaving a positively charged homogeneous background behind which Coulomb explodes. An ion having an initial radial position r will acquire asymptotically the kinetic energy

$$E_{\mathrm{c}} = 4\pi\rho r^2/3. \tag{4.6}$$

The Coulomb energy of an ion at the cluster surface is maximum and reads

$$E_{\mathrm{max}} = Q_{\mathrm{p}}/R = 4\pi\rho R^2/3 \tag{4.7}$$

(before the expansion). Thus the maximum kinetic energy is proportional to the square of the initial cluster radius. Therefore, the larger the size of a cluster is, the higher is the ion kinetic energy that can be obtained due to the Coulomb explosion, as in the results shown in Figs. 4.14 and 4.15. However, a higher laser intensity must be provided to remove all electrons for this kind of pure Coulomb expansion. Assuming a homogeneous spherical cluster the number of ions within r and $r + \mathrm{d}r$ is $\mathrm{d}N = 4\pi\rho r^2\,\mathrm{d}r$. The average ion kinetic energy E_{av} can be written as

$$E_{\mathrm{av}} = \frac{1}{N}\int E_{\mathrm{c}}\,\mathrm{d}N, \tag{4.8}$$

which yields

$$E_{\mathrm{av}} = \frac{3}{N}\left(\frac{4\pi\rho}{3}\right)^2\int_0^R r^4\,\mathrm{d}r = \frac{3}{5}E_{\mathrm{max}}. \tag{4.9}$$

Thus the average kinetic energy is only 60% of the maximum ion kinetic energy if the entire potential energy is finally transferred to the ions. This is *only* the case if no electrons stay inside the cluster. However, in general not all electrons are removed from the cluster before the explosion starts. Therefore it is necessary to calculate the fraction of electrons removed from the cluster at a given laser intensity.

Figure 4.16 shows the normalized number of electrons N_{e}/N within different radii R (initial radius), R_{max} (expanding radius), $2R_{\mathrm{max}}$ and $5R_{\mathrm{max}}$ after the pulse of various laser intensities. R_{max} is computed as $R_{\mathrm{max}} = \sqrt{R_x^2 + R_y^2 + R_z^2}$ with the expansion radii R_x, R_y and R_z along x, y and z, respectively. With increasing laser intensity N_{e}/N

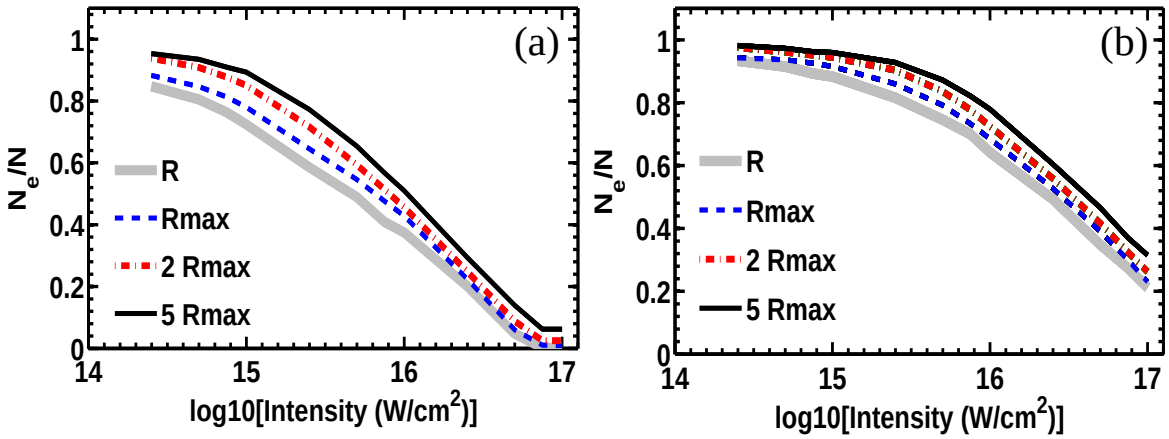

Figure 4.16: Normalized electron number N_e/N within different radii $R_{max}, 2R_{max}$ and $5R_{max}$ vs peak laser intensity for deuterium clusters of radii (a) $R = 4.39\,\text{nm}$ ($N = 17256$) and (b) $R = 7.98\,\text{nm}$ ($N = 103536$) after the laser pulse.

decreases because of outer ionization. At an intensity 10^{17}Wcm^{-2} one sees (in Fig. 4.16a) that almost all electrons are removed from the smaller cluster (see $N_e/N \approx 0$) while $N_e/N \approx 0.2$ (Fig. 4.16b) in the case of the bigger cluster. Hence pure Coulomb explosion in the smaller cluster occurs at an intensity 10^{17}Wcm^{-2} or higher. Instead, the central ions do not move appreciably in the bigger cluster (Fig. 4.15e) and $K_{min} \approx 0$ due to the presence of electrons at the cluster center.

4.3.2 Anisotropy in the expansion

For singly charged hydrogenic clusters one would expect an isotropic expansion. However, the expansion also depends on the number of electrons that stay inside the cluster (as seen in Fig. 4.16) and their dynamics. Bound electrons lower the net positive charge and slow down the expansion. The oscillations of bound electrons in a linearly polarized laser field breaks the spherical symmetry and results in an effective charge distribution along the laser polarization different from the transverse directions.

Figure 4.17a shows the distribution of the x, y and z-components of the kinetic energy shown in Fig. 4.15d for the intensity 10^{17}Wcm^{-2}. Ions have higher kinetic energy along the laser polarization (the x-component) than in the transverse (y, z)-directions. Figure 4.17a shows clearly that asymmetry in the ion energy distribution exists even for hydrogenic clusters where both asymmetric charge states and ionization ignition (as in Fig. 4.2 for argon cluster) are absent. To support this conclusion Fig. 4.17b shows the normalized expansion radii R_x/R, $R_y/R, R_z/R$, and R_{max}/R at different peak laser intensities after the pulse. One sees that the cluster expansion proceeds fastest along x. The maximum kinetic energy in Fig. 4.17a is due to the ions located at maximum radius along the laser polarization in Fig. 4.17b.

The above results show that ions with maximum kinetic energies are emitted along the laser polarization *even* if the charge state distribution is necessarily homogeneous, as it

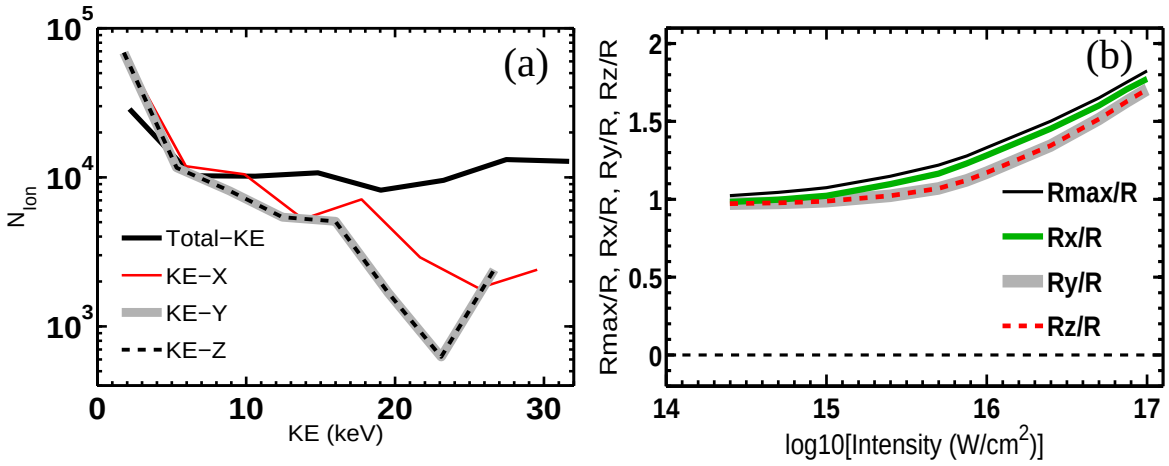

Figure 4.17: (a) Kinetic energy distribution of ions for a D_{103536} cluster ($R = 7.98\,\mathrm{nm}$) after an $n = 8$ cycle laser pulse $E_l(t) = E_0 \sin^2(\omega_l t/2n)\cos(\omega_l t)$ of intensity $10^{17}\mathrm{Wcm}^{-2}$. (b) Normalized expansion radius R_x/R along the laser polarization, expansion radii $R_y/R, R_z/R$ normal to the laser polarization direction (along y and z) and resultant expansion radius $R_{\max}/R = \sqrt{R_x^2 + R_y^2 + R_z^2}/R$ vs the peak laser intensity. Asymmetry in the expansion radii (b) and ion energy components (a) are clearly visible.

is the case in deuterium clusters. A similar asymmetry was seen in experiments with hydrogen clusters [41].

4.4 Summary

The PIC code was improved to take into account the self-consistent inner ionization and the ion dynamics. Energetic electrons and ions in the 100 keV-range, higher charge states of argon ions along the laser polarization than in the transverse directions, and asymmetry in the ion energy distribution (for both deuterium and argon clusters) were shown. Such an asymmetry is independent of the cluster type and arises due to the asymmetric electron motion in a linearly polarized laser field. High charge states of argon clusters were due to ionization ignition. However, ionization ignition saturates when the laser field is shielded by the space charge field so that ionic charges may be lower than expected from laser-atom interaction (ionization depletion). Laser energy absorption was confirmed to originate from NLR also in these more realistic simulations.

Chapter 5

Optimizing the ionization and energy absorption of laser-driven clusters

One of the goals in laser-cluster experiments and simulations is to convert as much laser energy as possible into energetic particles. This can be achieved by optimizing the outer ionization degree, i.e., by removing as many electrons as possible from the cluster in order to generate high charge states so that the asymptotic ion energy (and thus the total absorbed energy) after Coulomb explosion is largest.

One way to increase the charge states and the ion energy is to dope a cluster with atomic/molecular species of low ionization potential [98]. Such hetero-nuclear clusters may yield higher charge states of the species having the higher atomic charge number $\mathcal{Z}$ when doped with low $\mathcal{Z}$ atoms, boosting the energy of the lighter ions [99]. An almost two-fold increase of the highest charge states were obtained experimentally with argon clusters doped with water molecules [100]. Experimental results for xenon and silver clusters embedded in helium droplets were reported in Ref. [20].

The pulse duration and the sign of the chirp of a laser-pulse also affect ion charge states and ion energies [101]. Enhanced inner ionization of rare-gas and metal clusters irradiated by a sequence of dual laser pulses were observed [20, 80] experimentally. In these kinds of experiments one should adjust the delay time between pump and probe pulse such that the cluster expands sufficiently to meet the linear resonance $\omega_{\mathrm{Mie}} = \omega_{\mathrm{l}}$ with the probe pulse. Vlasov simulations [20] and semi-classical simulations [26] of a small Xe_{40} cluster subject to such a pump-probe setup showed an enhancement of the ion charge states. An optimum control multi-pulse simulation has also been performed [27].

In this work we investigate the effect of the laser wavelength by three-dimensional PIC simulations. The goal is to find an optimum wavelength for a fixed laser intensity and a given cluster. At this optimum wavelength (which turns out to be in the ultraviolet (UV) regime for the Xe clusters under consideration) a single ultrashort laser pulse is shown to be much more efficient than the "conventional" dual-pulse pump-probe setup.

Experimental signatures of enhanced x-ray yields and high charge states at short wavelengths [102–104] also suggest a clear impact of the laser wavelength on the laser-cluster interaction. Pump-probe experiments [20, 80], free electron laser (FEL) cluster exper-

iments [105] at the DESY facility, Hamburg, and a recent x-ray laser-cluster experiment [106] down to wavelengths < 100 nm also showed enhanced ionization.

Contrary to our findings recent MD simulations [107] concluded that (i) there is no influence of the laser wavelength on the charging of clusters in the regime $100 - 800$ nm for a laser intensity $\approx 10^{16}\mathrm{Wcm}^{-2}$ and (ii) that linear resonance plays no role, thus threatening the basis of the nanoplasma model [19]. Similar conclusions were reported by the same authors in Refs. [108, 109].

We consider short laser pulses in this work. Most of the earlier works were reported for the long-pulse regime where linear resonance (LR) absorption [19–27] occurs during the expanding phase of a cluster when the Mie-plasma frequency sufficiently drops so that the laser frequency can be met. At the time of LR the space charge field inside the cluster is strongly enhanced, leading to efficient ionization ignition. However, charged clusters in general expand inhomogeneously [39, 41] so that LR is never met everywhere inside the cluster at the same time. As a consequence, charge states and absorbed energy may not be optimized in this case.

The chapter is organized as follows. In Sec. 5.1 we briefly describe the simulation method and discuss the ionization of a cluster by a short laser pulse in Sec. 5.2. In Sec. 5.3 pump-probe simulation results are presented while Sec. 5.4 is devoted to the laser wavelength dependence of the cluster dynamics. A possibility to achieve 100% outer ionization is also discussed in Sec. 5.4 before we summarize the work in Sec. 5.5.

5.1 Details of the simulation

Details of our PIC simulation are already described in chapter 4 (also in Ref. [110]). Namely, we apply the dipole approximation $\boldsymbol{E}_\mathrm{l}(\boldsymbol{r}, t) \simeq \boldsymbol{E}_\mathrm{l}(t)$ and neglect binary collisions between electrons and ions, as in chapter 4. For the inner ionization we apply the Bethe-rule (4.1).

In this work we shall vary the wavelength down to 100 nm at an intensity $5 \times 10^{16}\mathrm{Wcm}^{-2}$, which raises the questions (i) whether such lasers are available and (ii) whether the Bethe-rule (4.1) is applicable. With the development of new generation FEL lasers [111, 112] all over the world the answer to (i) is clearly affirmative. As regards the ionization model (ii), the higher charge states are rather produced by multiphoton ionization than via tunneling or over-the-barrier ionization so that the Bethe-model (where the ionization probability switches from zero to unity once a certain threshold field is reached) may not yield the precise charging dynamics of the clusters at short wavelengths. However, the final charge state distribution should remain unaffected by the details of the ionization model [109] at least qualitatively.

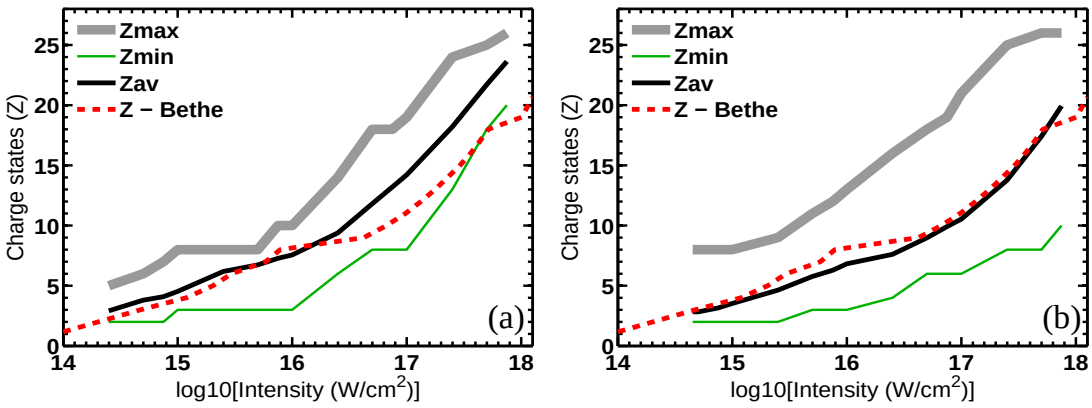

Figure 5.1: Maximum ion charge $\mathcal{Z}_{\max}$ (thick solid), minimum ion charge $\mathcal{Z}_{\min}$ (thin solid), average ion charge $\mathcal{Z}_{\rm av}$ (bold black) and the ion charge predicted by OFI alone (dashed) vs peak laser intensity for (a) a Xe_{2176} cluster of radius $R_0 \approx 3.54$ nm and (b) a Xe_{17256} cluster of radius $R_0 \approx 7$ nm in an $n = 8$ cycle laser pulse $E_{\rm l}(t) = E_0 \sin^2(\omega_{\rm l} t/2n)\cos(\omega_{\rm l} t)$ of wavelength $\lambda_{\rm l} = 800$ nm.

5.2 Ionization of a cluster by a single short pulse

First we study the response of a xenon cluster in a linearly polarized $n = 8$-cycle laser pulse of electric field strength $E_{\rm l}(t) = E_0 \sin^2(\omega_{\rm l} t/2n)\cos(\omega_{\rm l} t)$ and wavelength $\lambda_{\rm l} = 800$ nm. Different ionic charge states are self-consistently produced during the laser pulses of peak intensities $I_0 = E_0^2$ according to the Bethe rule (4.1).

Figure 5.1a shows the maximum charge state $\mathcal{Z}_{\max}$, the minimum charge state $\mathcal{Z}_{\min}$, and the average charge state $\mathcal{Z}_{\rm av}$ (defined as the total charge of the cluster divided by the number of atoms N) and the charge state predicted by the OFI ("Z-Bethe" curve) vs peak laser intensity for a Xe_N cluster ($N = 2176$) of initial radius $R_0 \approx 3.54$ nm after the pulse (i.e., after ≈ 22 fs). The maximum charge state $\mathcal{Z}_{\max}$ varies from $\mathcal{Z} = 5$ to $\mathcal{Z} = 26$ as the laser intensity increases from $2.5 \times 10^{14}\mathrm{Wcm}^{-2}$ to $7.5 \times 10^{17}\mathrm{Wcm}^{-2}$. The higher value of $\mathcal{Z}_{\max}$ above the value predicted by the OFI is clearly due to ionization ignition. Those maximum charge states $\mathcal{Z}_{\max}$ are mainly acquired by the ions at the cluster periphery where the space charge field is highest. Inside the cluster the total field falls below the ionization thresholds due to the decreasing space charge produced by the ionic background as well as due to the screening of the laser field by the cluster electrons. The ions close to the cluster center have minimum charge states $\mathcal{Z}_{\min} = 2 - 20$ at laser intensities between $2.5 \times 10^{14}\mathrm{Wcm}^{-2} - 7.5 \times 10^{17}\mathrm{Wcm}^{-2}$. The value of $\mathcal{Z}_{\min}$ remains much lower than predicted by the OFI for almost all laser intensities $< 5.0 \times 10^{17}\mathrm{Wcm}^{-2}$. The average charge $\mathcal{Z}_{\rm av}$ remains close to (but slightly higher than) the OFI predicted values at intensities $< 7.5 \times 10^{15}\mathrm{Wcm}^{-2}$. Also $\mathcal{Z}_{\max} = 8$ and $\mathcal{Z}_{\min} = 3$ do not change between the intensities $10^{15}\mathrm{Wcm}^{-2} - 7.5 \times 10^{15}\mathrm{Wcm}^{-2}$ but $\mathcal{Z}_{\rm av}$ increases slowly as more ions from the cluster center towards the periphery acquire higher charge states $3 \rightarrow 8$. The value of $\mathcal{Z}_{\max}$ remains constant, $\mathcal{Z} = 8$, due to the removal of all electrons from the $5s^2p^6$ shell of the Xe atoms close to the cluster boundary. As the intensity $\approx 7.5 \times 10^{15}\mathrm{Wcm}^{-2}$ is approached the laser field is strongly shielded from the central part of the cluster, and

outer ionization as well as ionization ignition tend to saturate. As a consequence $\mathcal{Z}_{\rm av}$ grows slowly between the intensities $\approx 5\times10^{15}{\rm Wcm}^{-2} - 10^{16}{\rm Wcm}^{-2}$. Unless a threshold intensity $\approx 10^{16}{\rm Wcm}^{-2}$ is crossed further electrons from the cluster cannot be removed, which was already seen in previous model and numerical calculations [28–31, 69, 70]. At higher intensities $> 10^{16}{\rm Wcm}^{-2}$ outer ionization and ionization ignition increases again, leading to an increase of $\mathcal{Z}_{\rm av}$ beyond the values predicted by the OFI due to the strong increase of both $\mathcal{Z}_{\rm max}$ and $\mathcal{Z}_{\rm min}$.

It is commonly believed that ionization ignition becomes increasingly pronounced with increasing cluster size. Figure 5.1b shows $\mathcal{Z}_{\rm max}$, $\mathcal{Z}_{\rm min}$, $\mathcal{Z}_{\rm av}$, and the charge states predicted by the OFI vs the peak laser intensities for a bigger Xe_N cluster ($N = 17256$) of initial radius $R_0 \approx 7$ nm. For the same laser pulse $\mathcal{Z}_{\rm max}$ now varies between $8-26$ and exceeds the charge states predicted by the OFI. Below the intensity $10^{17}{\rm Wcm}^{-2}$ $\mathcal{Z}_{\rm max}$ is higher by a factor of ≈ 2 compared to the OFI value ("Z-Bethe" curve). Although $\mathcal{Z}_{\rm max}$ remains much higher, the average ion charge $\mathcal{Z}_{\rm av}$ (in Fig. 5.1b) is below the charge states predicted by the OFI for most of the laser intensities. Most of the ions closer to the cluster center acquire charge states $\mathcal{Z}_{\rm min} = 2-10$ which are even lower than for the smaller cluster (Fig. 5.1a) at the corresponding intensities. Hence, ionization ignition is indeed responsible for the highest charge states $\mathcal{Z}_{\rm max}$ which increase with the cluster size (as seen in Fig. 5.1). However, exactly because of the same mechanism a bigger cluster will capture more electrons (whose outer ionization would require much higher laser intensities than in the case of a smaller cluster). The presence of more electrons in the central region will screen the laser field more efficiently. As a result both $\mathcal{Z}_{\rm av}$ as well as $\mathcal{Z}_{\rm min}$ (in Fig. 5.1b) drop below the corresponding values for the smaller cluster (Fig. 5.1a).

We conclude that an increasing cluster size (and thus increased ionization ignition of, at least, the ions located close to the cluster boundary) does not always lead to a higher average charge state. Our aim is to increase not only the highest charge states but also the average ion charge beyond the OFI predicted value through the charging of more ions in the central part of the cluster. In the following sections we study several approaches to achieve this goal.

5.3 Ionization by delayed pulses: a pump-probe simulation

In this section we illustrate the "pump-probe" method frequently employed in laser-cluster experiments. In this method an initial pump-pulse ionizes the cluster. The cluster expands freely before, after a delay time, a probe-pulse hits the expanding cluster. The interaction of this probe pulse with the cluster will sensitively depend on the cluster size and thus on the delay time. We revisit such a scenario in our current work since it will allow us to compare the efficiency of laser energy absorption for such a standard pump-probe method with the single UV pulse scenario which will be introduced in Sec. 5.4.

The laser field profile is of the form $E_{\rm l}(t) = E_0 \sin^2(\pi t/nT)\cos(\omega_{\rm l} t)$ for both pump and probe pulse. The time period T is chosen with respect to the wavelength 800 nm. For, say,

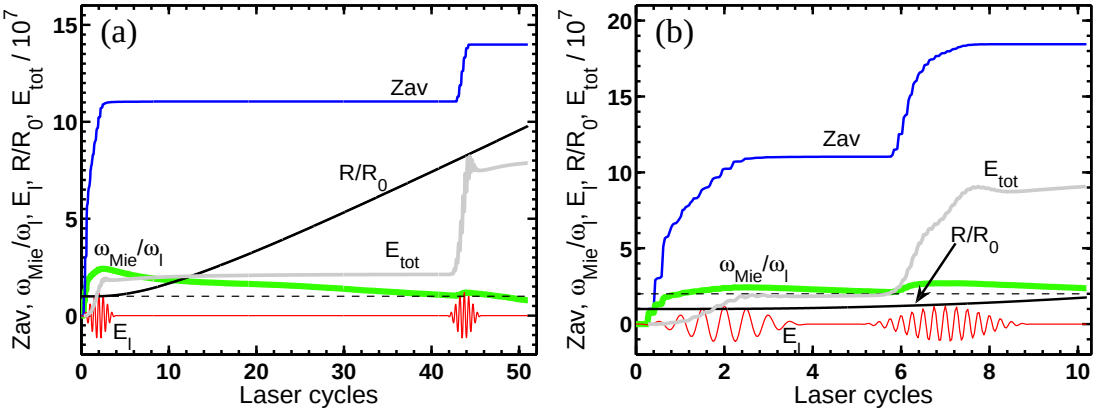

Figure 5.2: Average ion charge $\mathcal{Z}_{\rm av}$, scaled Mie-frequency $\omega_{\rm Mie}/\omega_{\rm l}$, laser field $E_{\rm l}$, normalized cluster expansion radius R/R_0 and total absorbed energy $E_{\rm tot}$ vs time (in 800 nm laser cycles) for a Xe_{17256} cluster of radius $R_0 \approx 7$ nm. The peak intensity 5×10^{16}Wcm^{-2} is the same for (a) pump of wavelength 400 nm (probe, 400 nm) and (b) pump of wavelength 400 nm (probe, 200 nm). The laser field is of the form $E_{\rm l}(t) = E_0 \sin^2(\pi t/nT)\cos(\omega_{\rm l} t)$ with $n = 4$ and one laser cycle T corresponding to the wavelength 800 nm. A minor increase in $E_{\rm tot}$ after the pulses is an artifact of PIC simulations.

$n = 4$ the product nT determines the total pulse duration ≈ 11 fs. The pulse envelope and intensity are kept the same for all cases under study, i.e., the laser energy in all pulses is the same too.

Figure 5.2a shows the results for the Xe_{17256} cluster of initial radius $R_0 \approx 7$ nm at an intensity 5×10^{16}Wcm^{-2} when both the pump and the probe pulse have the same wavelength 400 nm. The average charge $\mathcal{Z}_{\rm av}$, the scaled Mie-frequency $\omega_{\rm Mie}/\omega_{\rm l}$, the total absorbed energy $E_{\rm tot}$ (electrostatic field energy plus the kinetic energy of electrons and ions), the normalized cluster radius $R(t)/R_0$, and the laser fields are plotted vs time (in units of the period T). During the first four laser cycles of the pump-pulse the average charge state rises to $\mathcal{Z}_{\rm av} \approx 11$, the frequency $\omega_{\rm Mie}/\omega_{\rm l} \approx 2.5$ and $E_{\rm tot} \approx 2.0 \times 10^7$ while the cluster expansion is insignificant. The total energy $E_{\rm tot} \approx 2.0 \times 10^7$ corresponds to the average ion energy $E_{\rm tot}/N \approx 31.4$ keV. After the pump-pulse the cluster evolves freely and $\mathcal{Z}_{\rm av}$, $E_{\rm tot}$ remain unchanged but $\omega_{\rm Mie}/\omega_{\rm l}$ drops due to the expansion. Note that the cluster radius $R(t)$ (defining the cluster boundary) corresponds to the distance of the most energetic ions from the cluster center. At the boundary, however, the cluster potential is anharmonic. Hence using $R(t)$ for the calculation of the Mie-frequency $\omega_{\rm Mie}(t) = \sqrt{N\mathcal{Z}_{\rm av}/R^3(t)}$ the latter is underestimated. Instead we use the definition $\omega_{\rm Mie}(t) = \sqrt{Q_{\rm b}(t)/R_0^3}$ (as in Sec. 4.2.3) where $Q_{\rm b}(t)$ is the total ionic charge within the *initial* cluster radius R_0 where the cluster potential is close to harmonic at all times.

After 44 laser cycles $\omega_{\rm Mie}$ approaches the linear resonance (dashed line) with respect to the fundamental 400 nm, i.e., $\omega_{\rm Mie}/\omega_{\rm l} = 1$. The probe pulse of wavelength 400 nm is applied with a delay of ≈ 42 laser cycles such that the peak of the pulse approximately coincides with the resonance time. Due to the linear resonance the average charge and the absorbed energy rises abruptly up to the value $\mathcal{Z}_{\rm av} = 14$ and $E_{\rm tot} \approx 7.5 \times 10^7$, respectively. Such a pump-probe simulation clearly illustrates that the linear resonance indeed plays a role

in the cluster dynamics. More energy is absorbed, leading to higher charge states. These results are in agreement with hydrodynamic and Vlasov simulations [20, 80]. However, linear resonance is met only after a relatively long time when the cluster has already expanded significantly (as seen $R(t)/R_0 \approx 8$ in Fig. 5.2a). Ionization ignition and laser energy absorption in such a low density plasma is expected to be less efficient compared to the case where linear resonance occurs *before* the cluster expands significantly.

While keeping the 400 nm pump as above we now assume a probe wavelength of 200 nm for the purpose of hitting the linear resonance at an earlier time when the cluster is more compact. The energy in the probe pulse is the same as in Fig. 5.2a. Figure 5.2b shows the result analogous to Fig. 5.2a. The average charge and the absorbed energy now increase up to $\mathcal{Z}_{\rm av} = 18.5$ and $E_{\rm tot} \approx 9 \times 10^7$ which are higher than in Fig. 5.2a after the probe. With the pulse energies being the same in both cases a higher efficiency of energy absorption in the second scheme (Fig. 5.2b) is obvious. The reason is the smaller cluster size at the time of linear resonance ($R(t)/R_0 < 1.5$) and the higher space charge field related to it. Similar findings from experiments have been reported in Ref. [80]. In passing we note that the average charge $\mathcal{Z}_{\rm av} \approx 11$ in Fig. 5.2 due to the pump (at 400 nm) exceeds $\mathcal{Z}_{\rm av} \approx 8$ in Fig. 5.1b (at 800 nm) for the same cluster and the same laser intensity $5.0 \times 10^{16}\mathrm{Wcm}^{-2}$ despite the higher pulse-energy in Fig. 5.1b because of the twice longer pulse.

In the following section we study the wavelength dependence of the average charge states and the laser energy absorption.

5.4 Ionization at different wavelengths

Whether the average charge state and the absorbed energy for a given cluster increases with decreasing laser wavelength was not known. One could expect that for a certain wavelength the linear resonance during the initial ionization stage when the Mie-frequency rises from zero to its maximum value becomes important. For long wavelengths this early resonance is passed so quickly due to the rapid charging of the cluster that any indication of a resonance is washed out. We will show that this is not the case at shorter wavelengths.

We assume the same laser field profile $E_{\rm l}(t) = E_0 \sin^2(\pi t/nT)\cos(\omega_{\rm l} t)$ as in Sec. 5.2 with the same pulse duration, pulse energy, and intensity $5.0 \times 10^{16}\mathrm{Wcm}^{-2}$. We only vary the laser wavelengths in the range $800 - 100$ nm.

Figure 5.3a shows the average charge state $\mathcal{Z}_{\rm av}$ and total absorbed energy $E_{\rm tot}$ vs the laser wavelength for the Xe_{17256} cluster of radius $R_0 \approx 7$ nm after $t = 1, 2, 3, 4$-laser cycles at 800 nm. The value of $\mathcal{Z}_{\rm av}$ increases in time (in Fig. 5.3a) for all wavelengths. Ionization mostly occurs before $t = 2$ cycles when the peak of the pulse is reached. After that the space charge field is high enough to generate further charge states between $2 - 3$ cycles. $\mathcal{Z}_{\rm av}$ does not change anymore between $3 - 4$ cycles, indicating a saturation of inner ionization. The average charge state $\mathcal{Z}_{\rm av}$ increases from $\mathcal{Z} = 8$ to a maximum value $\mathcal{Z}_{\rm av} \approx 25$ as the laser wavelength is decreased from the infrared 800 nm down to the UV wavelength 125 nm. It means that the sub-shells $4s^2p^6d^{10}5s^2p^6$ of almost all atoms are

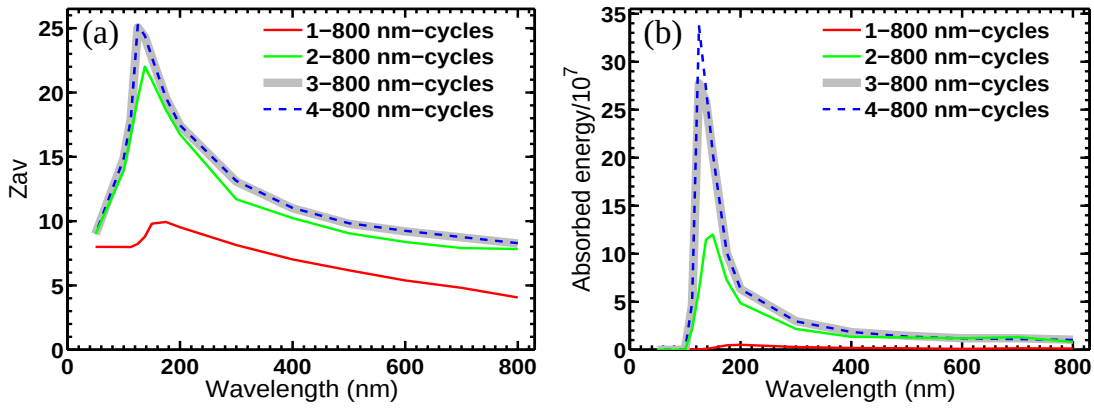

Figure 5.3: Average ion charge $\mathcal{Z}_{\rm av}$ (a) and total absorbed energy $E_{\rm tot}$ (b) vs laser wavelength after $1, 2, 3$ and 4 laser cycles (at 800 nm) for a Xe_{17256} cluster of radius $R_0 \approx$ 7 nm. Other parameters as in Fig. 5.2.

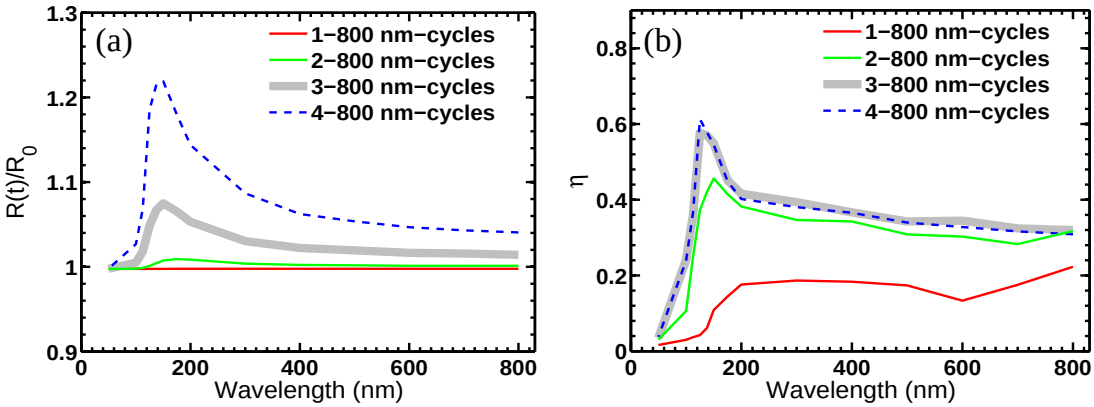

Figure 5.4: Normalized cluster expansion radius R/R_0 (a) and outer ionization degree η (b) vs laser wavelength, corresponding to Fig. 5.3.

empty at 125 nm. A further decrease of the wavelength causes $\mathcal{Z}_{\rm av}$ to decrease gradually to a smaller value $\mathcal{Z}_{\rm av} \approx 9$ at 50 nm.

Figure 5.3b shows a similar qualitative behavior of the absorbed energy both in the time domain and in the wavelength domain. The energy $E_{\rm tot}$ is maximum at the same wavelength $\lambda_{\rm l} = 125$ nm. Although the laser-pulse energy is the same in all cases the increased absorption at 125 nm, leading to a marked increase of the average charge up to a value $\mathcal{Z}_{\rm av} \approx 25$ clearly shows that wavelength effects are undoubtedly important. One may compare the absorbed energy and the average charge with the dual-pulse simulation results in Fig. 5.2. The absorbed energy $E_{\rm tot} \approx 34 \times 10^7$ and the average charge $\mathcal{Z} \approx 25$ are much higher in the present case around the laser wavelength 125 nm compared to the respective values $E_{\rm tot} \approx 9 \times 10^7$ and $\mathcal{Z}_{\rm av} \approx 18.5$ in Fig. 5.2b. The absorption is ≈ 3.78 times higher than in Fig. 5.2b. Moreover, in the dual-pulse case the total laser-pulse energy was twice higher. Therefore, the absorption efficiency is augmented further by a factor of two.

In Fig. 5.4 we plot the normalized expansion radius $R(t)/R_0$ (Fig. 5.4a) and the outer

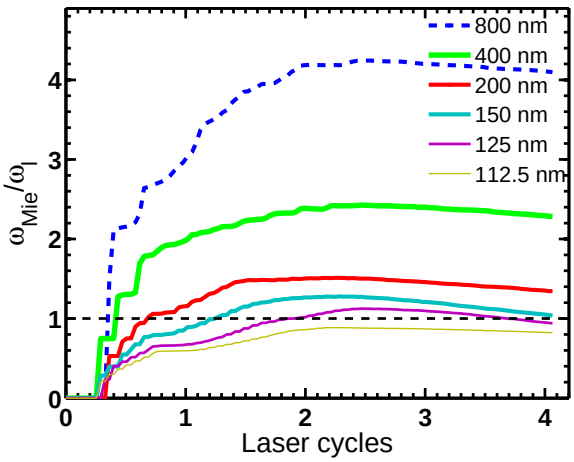

Figure 5.5: Scaled Mie-frequency $\omega_{\rm Mie}/\omega_{\rm l}$ vs time (in 800 nm cycles) for wavelengths $\lambda_{\rm l} = 800 - 112.5$ nm and the laser and cluster parameters of Fig. 5.3.

ionization degree η (number of total electrons outside $R(t)$ divided by the total number of electrons produced, $N\mathcal{Z}_{\rm av}(t)$, in Fig. 5.4b) vs the laser wavelength corresponding to the results in Fig. 5.3. The radius $R(t)$ and the outer ionization degree $\eta(t)$ go hand in hand with the absorbed energy $E_{\rm tot}(t)$ and the charge $\mathcal{Z}_{\rm av}(t)$. After four cycles the cluster has expanded very little, $R(4T)/R_0 \approx 1.225$ at $\lambda_{\rm l} \approx 125$ nm, although the average charge $\mathcal{Z}_{\rm av} \approx 25$ is very high compared to Fig. 5.2. With such an insignificant expansion the space charge field can be considered optimized, leading to maximum ionization ignition. The ignition field (i.e., the space charge field due to the ionic background) under the assumption that all electrons are removed reads $E_{\rm ig}(t) \approx N\mathcal{Z}_{\rm av}(t)/R(t)^2$. Using $R(t)$ from Fig. 5.4a and $\mathcal{Z}_{\rm av}(t)$ from Fig. 5.3a, one obtains at 125 nm $E_{\rm ig}(2T) \approx 20.0$, $E_{\rm ig}(3T) \approx 21.0$ and $E_{\rm ig}(4T) \approx 16.2$, if all electrons are removed (i.e., $\eta = 1$). The expected ignition field is maximum ≈ 21 near the pulse peak around $2-3$-cycles, thereafter decreases to $E_{\rm ig}(4T) \approx 16.2$ due to an expansion $R(4T)/R_0 \approx 1.225$ and no further creation of charge states. Note that the peak laser field is only $E_0 \approx 1.19$. Therefore the enhanced ionization is certainly due to the ignition field. However, at $\lambda_{\rm l} \approx 125$ nm $\eta \approx 0.6$ in Fig. 5.4b, meaning that 40% of the electrons are still inside the cluster. The presence of these electrons lowers $E_{\rm ig}$ compared to the above ideal case of $\eta = 100\%$ outer ionization, and one may argue that $E_{\rm ig}$ is not yet optimized. However, even if $\eta = 100\%$ outer ionization is achieved for the above laser field intensity the maximum total field is ≈ 22 which is still insufficient to produce a higher average charge $\mathcal{Z}_{\rm av} = 27$ (requiring a threshold field $\gtrapprox 24$ according to OFI). Hence the average charge state is optimized. This will be shown explicitly at the end of this section where we actually achieve $\eta \approx 100\%$ for this cluster.

The above results clearly show that there exists a certain wavelength at which the laser-cluster coupling is very efficient. Such a nonlinear dependence of the absorbed energy and average charge state on the laser wavelength indicates a resonance around 125 nm in Fig. 5.3 and 5.4. To investigate this further, we plot in Fig. 5.5 the scaled Mie-frequency $\omega_{\rm Mie}(t)/\omega_{\rm l}$ vs time. The dashed line indicates the linear resonance. Charging of the cluster starts around 0.3 cycles for all wavelengths by OFI, leading to an abrupt increase of $\omega_{\rm Mie}(t)/\omega_{\rm l}$ for the longer wavelengths while for the shorter ones the increase proceeds

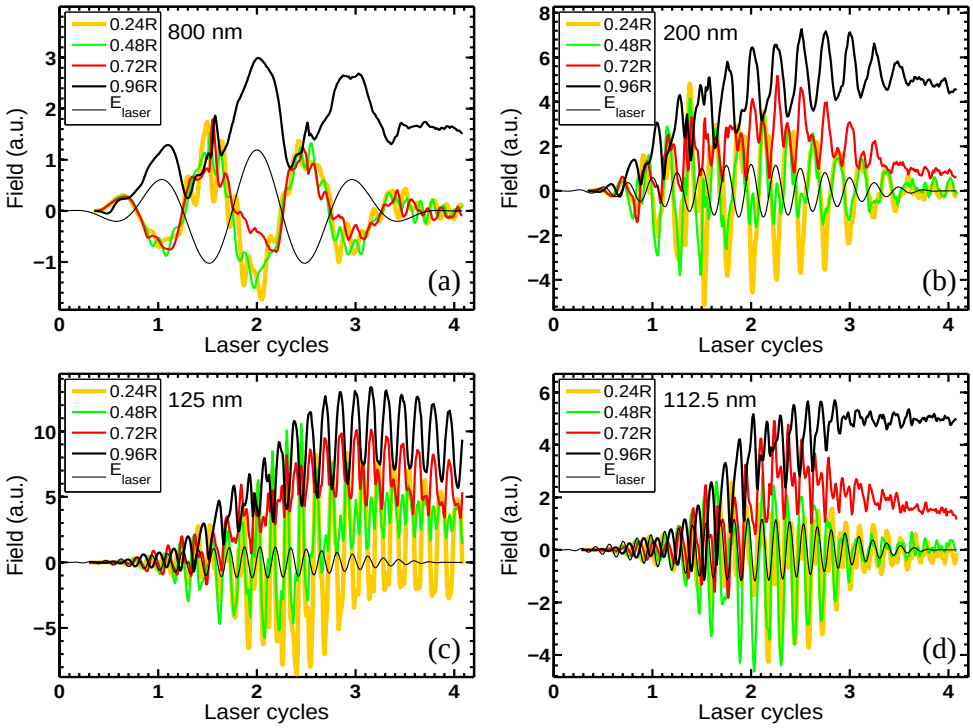

Figure 5.6: The x-component of the space charge field at radial distances $0.24R_0, 0.48R_0, 0.72R_0$, and $0.96R_0$ inside a Xe_{17256} cluster of radius $R_0 \approx 7$ nm and the laser field $E_l(t) = E_0 \sin^2(\pi t/nT)\cos(\omega_l t)$ of peak intensity $5 \times 10^{16}\mathrm{Wcm}^{-2}$ vs time (in periods corresponding to 800 nm) at (a) $\lambda_l = 800$, (b) $\lambda_l = 200$, (c) $\lambda_l = 125$, and (d) $\lambda_l = 112.5$ nm.

slower. As a result the plasma is overdense during the entire pulse for the long wavelengths but stays close to the linear resonance for the shorter wavelengths. The more time is spent near the linear resonance, the higher is the energy absorption and the average charge state, as seen in Fig. 5.3. At the wavelength 125 nm the resonance is met at the peak of the pulse so that the energy absorption is particularly efficient.

We now discuss the time evolution of the space charge field E^x_{sc} (along the laser polarization) at different positions inside the cluster to further illustrate the resonance at short wavelengths, leading to efficient ionization ignition and the generation of high charge states. Figure 5.6 shows the space charge field E^x_{sc} and the laser field E_l vs time at radial positions $0.24R_0$, $0.48R_0$, $0.72R_0$ and $0.96R_0$ for four different wavelengths. Figure 5.7 shows the corresponding phases with respect to the driving laser field.

At the long wavelength 800 nm, E^x_{sc} inside the cluster at radii $0.24R_0$, $0.48R_0$, $0.72R_0$ mostly oscillates with a phase $\delta \approx \pi$ while $\delta \approx 0$ at the boundary (i.e., at $0.96R_0$). This is clearly what one expects from an overdense plasma: screening of the laser field in the cluster interior but an opposite behavior outside the electron cloud. The oscillation of the space charge field arises due to the oscillations of the bound electrons inside the cluster. These electrons form approximately a sphere which is smaller than the cluster due to outer ionization. If the electron cloud was rigid and did not cross the cluster boundary the phase should be exactly π and 0 inside and outside, respectively, if the plasma is

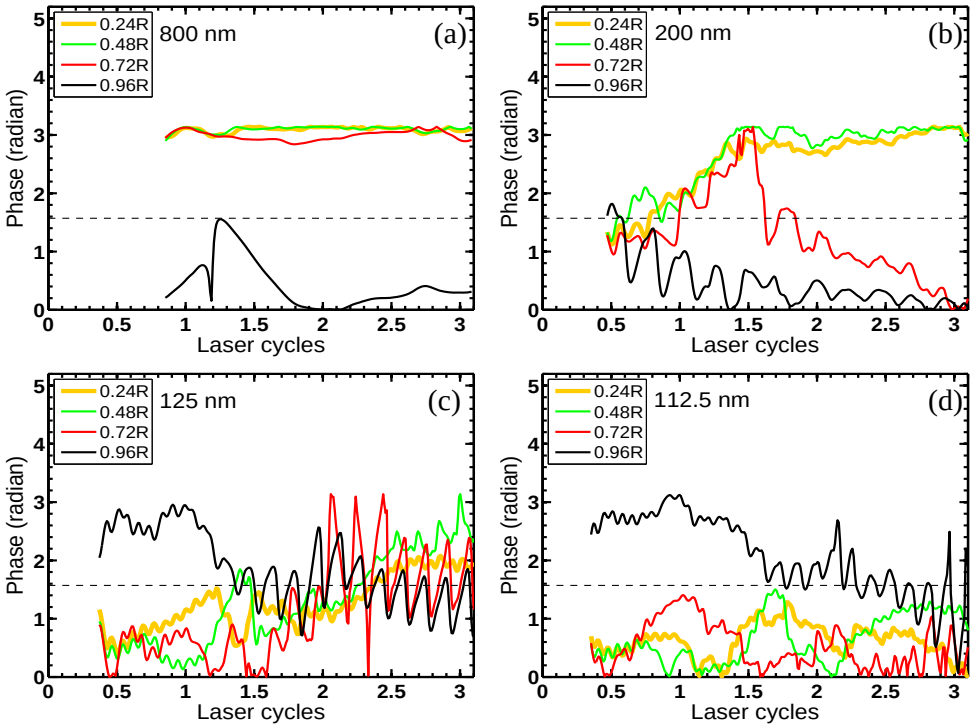

Figure 5.7: Phase of the space charge field with respect to the laser field at different radial distances corresponding to Fig. 5.6 vs time corresponding to Fig. 5.6.

overdense, and opposite in the underdense case. In reality, the bound electron population changes and the electron sphere is neither rigid nor has it a sharp boundary, resulting in phase distortions and deviations from the idealized case, as seen in Fig. 5.7a.

Figure 5.6 confirms explicitly that the total field at the boundary is highest and therefore leads to the highest ionic charge states while $E^x_{\rm sc}(t)$ almost nullifies the laser field in the strongly overdense regime. The maximum value of the total field at the peak of the pulse is ≈ 4.0 a.u. (x-component only) which is sufficient to produce charge states up to $\mathcal{Z} \approx 18$ (also seen in Fig. 5.1b). An additional contribution (up to a factor $\sqrt{3}$) to the total field comes from the y and z-components of the space charge field.

At 200 nm the amplitude of $E^x_{\rm sc}$ around $t = 1.5$ cycles at $0.24R_0$ increases up to 5 a.u. which, after addition to the laser field, is sufficient to produce charge states $\mathcal{Z} = 18$ even inside the cluster. After ≈ 1.75 cycles $E^x_{\rm sc}$ at $0.72R_0$ behaves similarly to that at $0.96R_0$, i.e., the laser and space charge fields at $0.96R_0$ and $0.72R_0$ are now approximately in phase. Figure 5.6b shows that the total field $\approx 4-8$ between $0.96R_0$ and $0.72R_0$, producing charge states $\mathcal{Z} \approx 18 - 23$. However, due to the screening of the laser field inside the cluster, many atoms there have only charge states $\mathcal{Z} < 18$ so that the average charge state is $\mathcal{Z}_{\rm av} \approx 18$ in Fig. 5.3. From Fig. 5.7b it is seen that before $t = 1.75$ cycles the phase of $E^x_{\rm sc}$ at $0.72R_0$ approximately follows the phase at the smaller radii $0.24R_0$ and $0.48R_0$ since the plasma is evolving from under to overdense. Then, with increasing outer ionization and thus shrinking electron sphere, $E^x_{\rm sc}$ at $0.72R_0$ drops and approaches the behavior for $0.96R_0$.

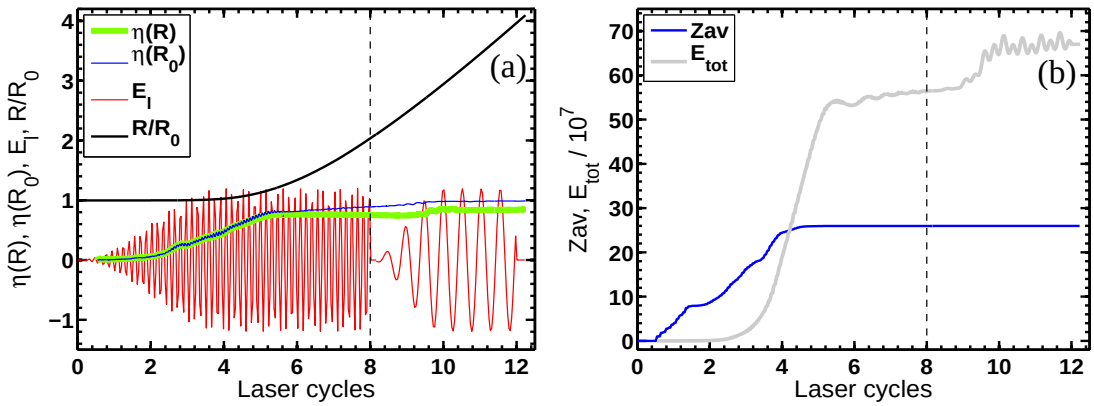

Figure 5.8: Variation of (a) normalized cluster radius R/R_0, degree of outer ionization $\eta(R), \eta(R_0)$ within R and R_0, laser field E_l (b) average ion charge $\mathcal{Z}_{\rm av}$ and total absorbed energy $E_{\rm tot}$ in time (in units of the laser period T corresponding to 800 nm) for the Xe_{17256} cluster of Fig. 5.3. The two laser pulses of wavelength 125 and 415 nm, respectively, are included in (a). The peak intensity is the same as in Fig. 5.3 for both pulses.

At the resonant wavelength 125 nm violent oscillations of the electron cloud are driven, leading to a particularly high total field everywhere inside the cluster and an average charge state $\mathcal{Z}_{\rm av} \approx 25$ in Fig. 5.3. Higher charge states $\mathcal{Z} > 26$ are not produced because of the high threshold field ≈ 24 necessary to crack the M-shell. One may argue that the presence of 40% electrons inside the cluster (in Fig. 5.4b) will deplete the field inside significantly. However, one should keep in mind that at resonance the electron cloud oscillates with a large excursion (infinite if any damping mechanism was absent), exposing a substantial part of the naked ionic background, leading to an enhanced "dynamical ionization ignition" [12] which can produce higher charge states than expected from the laser field alone even inside the cluster. Finally, after $t = 3$ cycles $E^x_{\rm sc}$ at the boundary drops due to the cluster expansion. As expected, the phases plotted in Fig. 5.7c fluctuate around $\pi/2$ throughout the cluster once the resonance condition is met.

At 112.5 nm the plasma remains underdense. Figure 5.6d shows that the space charge field amplitudes drop compared to those in Fig. 5.6c, yielding less ionization ignition and absorbed energy, similar to the 200 nm-case.

Even in the optimal 125 nm case presented so far only 60% of the generated electrons were removed from the cluster (visible in Fig. 5.4b). Therefore outer ionization and ionization ignition was certainly not optimized. We argued that even if the remaining 40% electrons were removed, the average charge state would not be significantly increased as compared to that shown in Fig. 5.3a. To prove that, we performed PIC simulations for the same cluster and the same peak intensity but now employing two consecutive pulses (shown in Fig. 5.8). The first pulse of resonant wavelength 125 nm with respect to the still compact cluster is ramped up over four 800 nm-cycles and held constant afterwards up to 8 cycles (the details of how the pulse is ramped down do not matter; therefore it is simply switched off abruptly). At $t = 8$ cycles a second pulse is switched on (over 2 cycles) whose frequency is resonant with the Mie-frequency around $t = 10$ cycles.

After the first pulse the cluster doubled its radius, and the outer ionization degree amounts to $\eta(R) \approx 0.8$ so that 20% electrons are still inside the cluster of radius $R(t)$ while $\approx 10\%$ are inside a sphere of radius R_0. The average charge $\mathcal{Z}_{\mathrm{av}}$ in Fig. 5.8b does not change significantly compared to Fig. 5.3a although the pulse energy per unit area $\int_0^{8T} E_{\mathrm{l}}^2(t)\,\mathrm{d}t$ is $\approx 3-4$ times higher.

The purpose of the second pulse shown in Fig. 5.8b is the removal of the residual electrons. Although almost 95% outer ionization within the expanding radius R and 99% within R_0 are achieved, no higher charge states are created. The absorbed energy also does not rise significantly so that the higher input energy invested into the two pulses does not pay off. Hence a single, short UV-pulse of wavelength 125 nm turns out to be optimal with respect to fractional energy absorption and generation of a high average charge state under the conditions considered.

5.5 Summary

In summary, we studied the interaction of xenon clusters with intense short laser pulses using a three-dimensional PIC code. Our aim was to optimize for a given cluster the laser energy absorption and the generation of high average charge states. The latter will then lead to energetic ions upon Coulomb explosion. We showed that for a given laser intensity an optimal laser wavelength exists that, under the typical conditions studied in this work, lies in the UV regime. Energy absorption is optimized when resonance is met during an early stage of the dynamics when the cluster is still compact. The conventional, long-pulse linear resonance during the expansion of the cluster is less efficient.

Chapter 6

Harmonic generation from laser-irradiated clusters

While the energy absorption by cluster nanoplasmas has been widely studied both in experiments and theory, much less attention has been paid to the laser harmonic emission from such systems. Meanwhile, it is known from the physics of intense laser-*atom* interaction that the effects of multiphoton absorption, leading to so-called above threshold ionization and high order harmonic generation, are intimately related and can be described as different channels of the highly nonlinear laser-atom coupling. In intense fields, the laser-cluster coupling is also known to be highly nonlinear. In fact, nonlinear resonance has been shown in chapter 3 and Refs. [29–31, 69, 70, 113] to be of particular importance for the energy transfer from the laser pulse to the electrons of the nanoplasma and the subsequent outer ionization. Most naturally the question arises whether laser-driven clusters can be an efficient source of high-order harmonics as well. Up to now, very few experimental results on harmonic generation (HG) from cluster targets have been published. In Refs. [83–85] HG from rare-gas clusters irradiated by infrared pulses of moderate intensity ($\simeq 10^{13} - 10^{14}\mathrm{W/cm^2}$) was measured. It was shown that under such conditions harmonics can be generated up to higher orders and with higher saturation intensities than in a gas jet. However, the effects observed in Refs. [83–85] should be attributed to standard atomic HG modified by the fact that in clusters the atoms are disposed closer to each other while the physical origin of HG remains the same as in a gas jet. Only very recently, first experimental observations of the third harmonic (TH) generation from argon clusters subject to a strong laser field were reported in Ref. [114] where resonant enhancement of the TH yield, occurring when $\omega_{\mathrm{Mie}} \to 3\omega_{\mathrm{l}}$, has been demonstrated using a pump-probe setup. The enhancement of the single-cluster response studied in theory before [35, 87, 115, 116] is, however, modified in the experiment by phase matching effects. The latter point complicates experimental studies of nanoplasma radiation while in computations one can first examine the single-cluster response and may include propagation effects in a second step.

In this chapter, we concentrate on the single-cluster radiation in a short, intense laser pulse. The questions we address here are: (i) can a substantial resonant enhancement of low-order harmonics be achieved and controlled and (ii) should any significant signal of

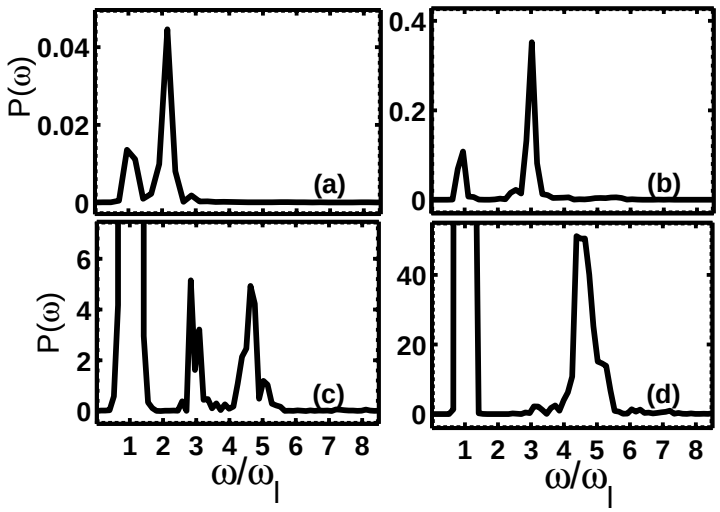

Figure 6.1: Normalized harmonic power $P(\omega) = |A(\omega)/N|^2$ vs harmonic order for an Ar_{17256} cluster at laser intensities $2.5 \times 10^{14}\mathrm{Wcm}^{-2}$ (a), $2.5 \times 10^{15}\mathrm{Wcm}^{-2}$ (b), and $7.5 \times 10^{17}\mathrm{Wcm}^{-2}$ (c). The spectrum (d) is for an Ar_{92096} cluster at the intensity $7.5 \times 10^{17}\mathrm{Wcm}^{-2}$.

high-order harmonics be expected from laser-driven nanoplasmas at such conditions. We study HG by three-dimensional PIC simulations for large Ar_N clusters (with the number of atoms $N \approx 10^4$–10^5 and radii $R_0 \approx 6$–$10\,\mathrm{nm}$) irradiated by linearly polarized, $n = 8$ cycle $\sin^2$-laser pulses with an electric field $\boldsymbol{E}_\mathrm{l}(t) = \boldsymbol{E}_0 \sin^2(\omega_\mathrm{l} t/2n)\cos(\omega_\mathrm{l} t)$ and wavelength $\lambda = 800$ nm. Previous PIC simulations of HG from laser-driven clusters [29, 87] were performed for two-dimensional (rod-like) clusters. Details of our PIC simulations were already mentioned in chapter 4.

6.1 Particle-in-cell results

Because of azimuthal symmetry the total dipole acceleration $A(t)$ is along the polarization direction of the laser pulse (x-axis). Its Fourier transformed amplitude $A(\omega)$ yields the dipole radiation power at the frequency ω. Figure 6.1 shows the normalized harmonic power $P(\omega) = |A(\omega)/N|^2$ vs the harmonic order at various laser intensities. The spectra (a)-(c) are the results for an Ar_{17256} cluster ($R_0 = 6.2$ nm) while the spectrum (d) corresponds to an Ar_{92096} cluster ($R_0 = 10.9$ nm). At the intensity $2.5 \times 10^{14}\mathrm{Wcm}^{-2}$ one observes a pronounced second harmonic. Upon increasing the laser intensity the third harmonic power also increases and becomes comparable to the fundamental at higher laser intensities (b). Increasing the intensity further, the fifth harmonic appears in the spectrum (c). For the same intensity but a bigger cluster, the third harmonic is strongly suppressed as compared to the fifth harmonic (d).

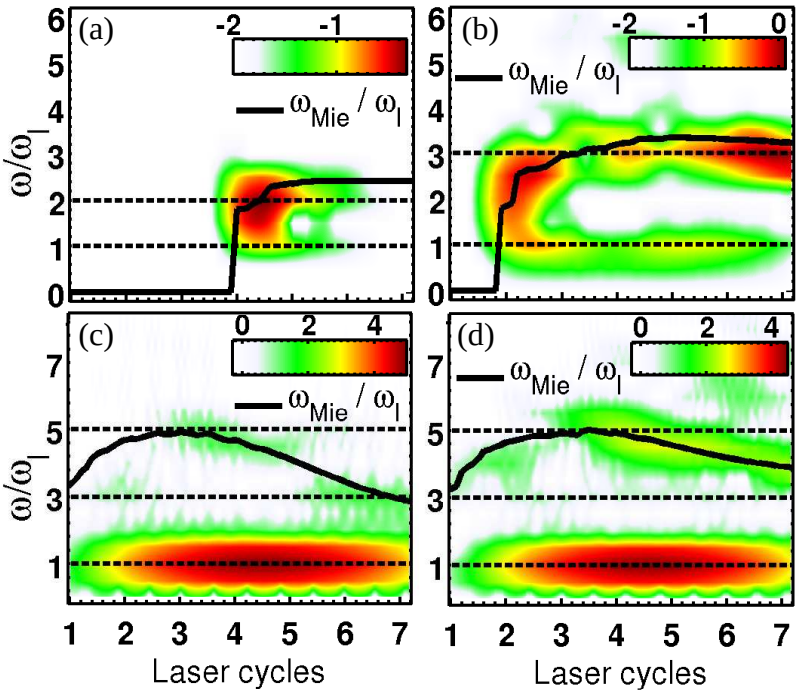

Figure 6.2: Time-frequency diagrams corresponding to the spectra of Fig. 6.1 with the normalized power $\log_{10} P$.

6.1.1 Time-frequency analysis

The enhancements of particular harmonics are due to the resonance between their frequencies and the Mie-frequency of the expanding nanoplasma [35]. To show this we retrieve the temporal information of the radiation by a time-frequency (TF) analysis of the spectra in Fig. 6.1. Figure 6.2 shows the respective TF diagrams. The scaled Mie-frequency $\omega_{\mathrm{Mie}}(t)/\omega_{\mathrm{l}}$ vs time is included in the plots. Note that a Mie-frequency can only be defined unambiguously as long as the ionic background remains homogeneously charged. From the simulations we find that the charge homogeneity is well satisfied within the initial cluster radius R_0 while in the outer regions of the expanding cluster this is not the case. We therefore define, as in chapter 4,

$$\omega_{\mathrm{Mie}}(t) = \sqrt{Q_{\mathrm{b}}(t)/R_0^3}$$

with $Q_{\mathrm{b}}(t)$ the total ionic charge inside the sphere of radius R_0 within which the cloud of well-bound electrons oscillates.

At the intensity $2.5 \times 10^{14}\mathrm{Wcm}^{-2}$ (Fig. 6.2a, corresponding to Fig. 6.1a) the laser field yields only Ar^+ ions. This first ionization by the laser field alone gives rise to an abrupt jump of $\omega_{\mathrm{Mie}}(t)/\omega_{\mathrm{l}}$ up to the value $\omega_{\mathrm{Mie}}/\omega_{\mathrm{l}} \approx 1.8$, followed by a slower increase above this value due to ionization ignition [11, 12] and finally ends with a plateau. The cluster expansion is so slow that $\omega_{\mathrm{Mie}}(t)/\omega_{\mathrm{l}}$ does not drop within the time interval plotted. The second harmonic power peaks when $\omega_{\mathrm{Mie}}(t)/\omega_{\mathrm{l}} = 2$ is met. This is because the electron dynamics contain oscillations both at the driving frequency and at the eigenfrequency,

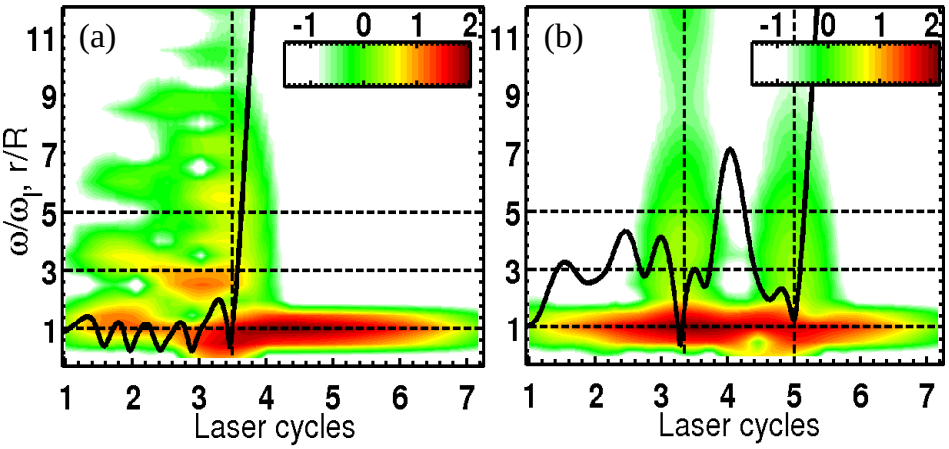

Figure 6.3: TF spectrograms for two PIC electrons of the Ar_{17256} cluster irradiated by the laser intensity $5 \times 10^{16}\mathrm{Wcm}^{-2}$. The dimensionless electron distance from the cluster center $r(t)/R_0$ is indicated by the solid line.

depending on the initial conditions and the form of the potential. In long pulses such oscillations at the eigenfrequency are damped due to various relaxation processes and do not contribute to the measured harmonic signal. Figure 6.2b shows an enhanced third harmonic (corresponding to Fig. 6.1b) at the time when $\omega_{\mathrm{Mie}}(t)/\omega_{\mathrm{l}} \approx 3$. The third harmonic power starts increasing again around the 6th cycle when $\omega_{\mathrm{Mie}}(t)$ passes through the same resonance due to the cluster expansion. Figures 6.2c,d show the TF spectrograms corresponding to spectra (c) and (d) in Fig. 6.1 at the intensity $7.5 \times 10^{17}\mathrm{Wcm}^{-2}$. Figure 6.2c clearly shows enhanced third and fifth harmonic emission when the scaled Mie-frequency approaches the respective odd numbers. For the bigger cluster Fig. 6.2d shows enhanced emission, preferentially following the Mie-frequency. As in the case with the second harmonic shown in Fig. 6.2a this is a consequence of the undamped oscillations at the time-dependent eigenfrequency in the expanding cluster potential. However, pronounced emission starts around the 4th cycle when $\omega_{\mathrm{Mie}}(t)$ meets $5\omega_{\mathrm{l}}$. Despite the same laser intensity as in Fig. 6.2c $\omega_{\mathrm{Mie}}(t)$ does not reach $3\omega_{\mathrm{l}}$ during the slower expansion of the bigger cluster in Fig. 6.2d. Note that the fulfillment of the resonance condition $\omega_{\mathrm{Mie}}(t) = m\omega_{\mathrm{l}}$ (with m integer) is not sufficient for the emission of harmonics. A necessary condition is the presence of some nonlinearity in the electron motion (i.e., anharmonicity in the effective potential). This nonlinearity may either originate from electrons jutting out of the core during their motion, sensing the Coulomb tail [35], or from the inhomogeneous charge distribution within the ion core [87].

6.1.2 Reason for the absence of high harmonics

To clarify where the major contribution to the spectrum comes from we consider the radiation of individual PIC particles. Figure 6.3 shows the TF analysis of the radiation from two PIC electrons. It is clearly seen that electrons radiate *harmonics* as long as they remain inside the cluster. Leaving the cluster, they emit an intense *flash* with an almost

continuous spectrum that extends up to significantly higher frequencies than present in the net harmonic spectrum shown in Fig. 6.1. After liberation, the electrons emit only the fundamental frequency (linear Rayleigh scattering). A liberated electron may rescatter, giving rise to a second flash in the TF spectrograms (Fig. 6.3b). However, no indications of such intense flashes are visible in the net spectra shown in Figs. 6.1 and 6.2. The mechanism behind outer ionization (nonlinear resonance) allows to interpret these findings. Individual electrons move in the selfconsistent field which could be subdivided into its slowly-varying and its oscillating component. The slowly-varying field is induced by the quasistatic part of the space charge. Ideally, it is a stationary potential well if one ignores a slow evolution of the charge distribution due to the inner and outer ionization and the cluster expansion. The oscillating part of the field is a superposition of the incident laser field and the field induced by the oscillating electron cloud. In the low-frequency limit $\omega_{\mathrm{Mie}}(t) \gg \omega_{\mathrm{l}}$ these two contributions are known to almost compensate each other so that the amplitude of the net oscillating field inside the cluster is small compared both to the applied laser field and the quasistatic space charge field. If the electron energy in the quasistatic well is far from the resonance its trajectory remains weakly disturbed by the oscillating field. This causes HG with rapidly decreasing yield as a function of the harmonic order. As soon as the electron energy approaches the resonance, the same small perturbation results in a strong effect: the electron motion becomes strongly disturbed and stochastic. A stochastic near-resonance behavior is a well-known property of nonlinear systems driven by time-dependent forces [117]. In the cluster case it leads to almost prompt and irreversible outer ionization. Hence, passing through the resonance, an individual electron, upon leaving the cluster potential, emits radiation due to its strong acceleration, seen as a flash in the TF spectrograms (Fig. 6.3). However, exactly because of the stochastic nature of nonlinear resonance the electrons' trajectories are very sensitive to the initial conditions with which the nonlinear resonance is entered. As a result, flashes from different electrons are incoherent (the corresponding amplitudes have nearly random phases), and, being added up in the total dipole acceleration, they disappear [118]. This shows that exactly the same mechanism behind efficient energy absorption by and outer ionization from clusters, namely nonlinear resonance [29–31, 69, 70, 113], restricts HG from them by breaking the coherent electron motion once it becomes strongly anharmonic. Only well-bound electrons trapped inside the ionic core with energies far from the resonance contribute to the net, coherent radiation of the cluster.

6.2 Reconstruction of the nanoplasma charge density: a numerical pump-probe study

The time-dependent enhancements of particular harmonics analyzed above may be used for the reconstruction of the maximum cluster charge density (i.e, maximum Mie-frequency). The TF spectrograms discussed above in Fig. 6.2 were obtained from our numerical experiments while it is not possible to record them in a real "single shot" experiment. To that end a more realistic pump-probe setup (see, e.g., [20, 114]) is envisaged with the following PIC simulations. We combine the 800 nm near-infrared laser pulse (M-pulse, pump) with

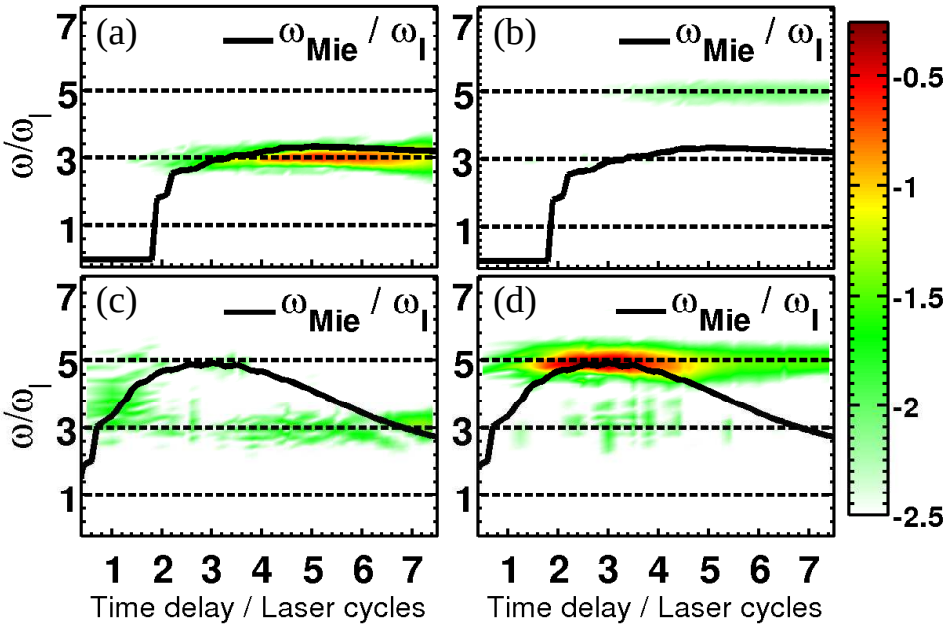

Figure 6.4: Dipole power $\log_{10} P_{y,z}(\omega)$ along y, z vs time delay t_d and frequency ω/ω_l with the pump-pulse intensities (a,b) $2.5 \times 10^{15}\mathrm{Wcm}^{-2}$ (cf. Fig. 6.2b), (c,d) $7.5 \times 10^{17}\mathrm{Wcm}^{-2}$ (cf. Fig. 6.2c) and the probe-pulse intensity $2.5 \times 10^{12}\mathrm{Wcm}^{-2}$ with $m = 3$ (a,c) and $m = 5$ (b,d).

two UV pulses (X-pulses, probe)

$$E_{y,z}(t) = E_{0y,z} \exp\left[-(\ln 2)\frac{\omega_l^2(t-t_d)^2}{\pi^2}\right] \sin[m\omega_l(t-t_d)]$$

of wavelength $\lambda_X = 800\,\mathrm{nm}/m$ (with $m = 3, 5$), applied at different time delays t_d. To distinguish the contributions of M and X-pulses to the dipole acceleration we apply them polarized along y and z axis, respectively. The two X-pulses of different harmonic frequencies $m = 3, 5$ trigger independent Mie-oscillations of electrons in the respective directions. The total power $P_{y,z}(\omega) = |A_{y,z}(\omega)/N|^2$ is recorded at various time delays. Whenever $Q_b(t)$ is such that $\omega_{\mathrm{Mie}}(t) = m\omega_l$ for a certain time delay the corresponding detector is expected to measure the maximum dipole radiation. Applying the two X-pulses simultaneously has the computational advantage of getting twice as much information in a single run than with just one probe pulse. Experimentally, a comb of low harmonics (e.g., from a gas jet) could be applied as a probe pulse.

Figures 6.4a,b show $\log_{10} P_{y,z}(\omega)$ vs t_d and ω using X-pulses of frequencies $3\omega_l$ and $5\omega_l$, respectively. For $\omega_X = 3\omega_l$ a resonance enhancement of the third harmonic power when $\omega_{\mathrm{Mie}}/\omega_l$ crosses ω_X at $t_d > 3.5$ cycles is clearly seen, showing that the information revealed in the TF spectrogram of Fig. 6.2b is accessible in the more realistic pump-probe set-up. The enhancement is maximum when $\omega_{\mathrm{Mie}}/\omega_l$ (i.e., the charge density ρ) is maximum around $t_d \approx 5$ laser cycles. The frequency $\omega_X = 5\omega_l$ of the X-pulse along z in Fig. 6.4b, being off-resonant with ω_{Mie}, shows (an order of magnitude) less intense radiation. Figure 6.4a allows the conclusion that the maximum cluster charge density was at least in

the vicinity corresponding to $\omega_{\rm Mie} \approx 3\omega_{\rm l}$, i.e., $\max[\rho(t)] \approx 27\omega_{\rm l}^2/4\pi$ at that time. Figures 6.4c,d are the analogues of Figs. 6.4a,b but at an M-pulse intensity $7.5 \times 10^{17}{\rm Wcm}^{-2}$, corresponding to Fig. 6.2c. The enhanced radiation is clearly seen at those times when $\omega_{\rm Mie}/\omega_{\rm l}$ meets the X-pulse (along y) frequency $\omega_X/\omega_{\rm l} = 3$. However, the maximum of $\omega_{\rm Mie}/\omega_{\rm l}$ resonates with the other X-pulse (along z, Fig. 6.4d) frequency $\omega_X = 5\omega_{\rm l}$ at $t_d \approx 3$ cycles, and, indeed, the maximum of the radiated power recorded in Fig. 6.4d is about an order of magnitude higher than in Fig. 6.4c.

6.3 Rigid sphere model

In this section we illustrate harmonic radiation from cluster nanoplasmas by the rigid sphere model described in chapter 3. In particular we show the same physical scenario of the harmonic emission as exhibited by the PIC results in the previous section, namely the incoherency between the emitted radiation of different electrons upon leaving the cluster potential via the nonlinear resonance. Thus we support our PIC results with a model.

We repeat the equation of motion for the electron sphere in a linearly polarized laser field,

$$\frac{{\rm d}^2\bar{r}}{{\rm d}\tau^2} + \left(\frac{\omega_{\rm Mie}}{\omega_{\rm l}}\right)^2 \left\{ \begin{array}{c} 1 - \dfrac{9r}{16} + \dfrac{r^3}{32} \\ r^{-3} \end{array} \right\} \bar{r} = -\frac{E_{\rm l}(\tau)}{R\omega_{\rm l}^2}. \tag{6.1}$$

We solve Eq. (6.1) numerically (with initial conditions $x(0) = 0, \dot{x}(0) = 0$) and record the dipole acceleration $a(\tau) = \ddot{\bar{r}}(\tau)$ and the effective frequency $\omega_{\rm eff}(\tau)$ [see Eq. (3.9)] at a given laser intensity. With the RSM it was shown before (see Fig.3.1) that NLR always occurs only above a threshold intensity $I_{\rm th}$. When NLR occurs $[\omega_{\rm eff}(\tau)/\omega_{\rm l}]^2 = 1$ is precisely met, the electron sphere becomes free, and energy absorption becomes efficient [30, 69, 70]. A deficiency of this RSM is that it yields a wrong exponent of the radiated power $P(k\omega) \propto |E_{\rm l}|^{(2k-2)}$ of the kth harmonic due to the even powers of excursion in the force (6.1) instead of the expected $P(k\omega) \propto |E_{\rm l}|^{2k}$ as in Ref. [35]. However, the RSM (6.1) still provides qualitative physical understanding.

6.3.1 Dipole radiation

The Fourier transform of the acceleration $a(\tau)$ yields the radiation power $P(\omega) = |a(\omega)|^2$ of a harmonic at the frequency ω. Figure 6.5a shows $P(\omega)$ vs $\omega/\omega_{\rm l}$ for a Xe_{1600} cluster at intensities $I_1 = 2.5 \times 10^{14}{\rm Wcm}^{-2}$, $I_2 = 1.5 \times 10^{16}{\rm Wcm}^{-2}$, and $I_3 = I_{\rm th} \simeq 1.698 \times 10^{16}{\rm Wcm}^{-2}$. Figures 6.5b,c are the TF diagrams corresponding to the spectra at I_2 and I_3 in Fig. 6.5a. The variation of $\omega_{\rm eff}/\omega_{\rm l}$ and the absolute phase $\delta(\tau)$ of the acceleration $a(\tau)$ vs time are also included in the TF plots. At the intensity $I_1 = 2.5 \times 10^{14}{\rm Wcm}^{-2}$ much below the threshold intensity of the NLR, one observes mainly odd harmonics of the laser frequency. Since $\omega_{\rm Mie} = \sqrt{4\pi\rho/3} = 4\omega_{\rm l}$, the fourth harmonic appears in the spectrum (Fig. 6.5a) due to the finite laser pulse. This illustrates the presence of even harmonics equal to the Mie-frequency as in the PIC results in Fig. 6.1a and 6.2a. At a

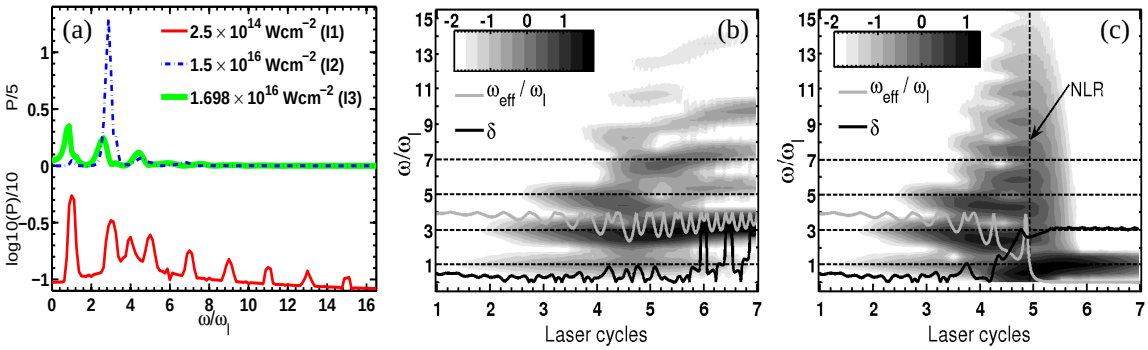

Figure 6.5: RSM results: (a) Harmonic power $P = |a(\omega)|^2$ vs the harmonic order ω/ω_l for a Xe_{1600} cluster (charge density $\rho = 48\rho_\mathrm{c}$, radius $R = 3.2$ nm) at intensities $I_1 = 2.5 \times 10^{14}\mathrm{Wcm}^{-2}$ (thin solid), $I_2 = 1.5{\times}10^{16}\mathrm{Wcm}^{-2}$ (dashed dot), and $I_\mathrm{th} \simeq 1.698{\times}10^{16}\mathrm{Wcm}^{-2}$ (thick solid). (b,c) TF spectrograms of the spectra at I_2 and I_3. Enhanced emission occurs only at the time of NLR (dashed vertical in (c)) at about 5-cycles when $\omega_\mathrm{eff}/\omega_\mathrm{l} = 1$. $\omega_\mathrm{eff}/\omega_\mathrm{l}$ drops to zero after the NLR. A phase change $\delta = \pi$ occurs immediately before the NLR. The $n = 8$-cycle laser pulse $E_\mathrm{l}(\tau) = E_0 \sin^2(\tau/2n)\cos(\tau)$ is of wavelength $\lambda_\mathrm{l} = 1056$ nm.

higher intensity $I_2 = 1.5 \times 10^{16}\mathrm{Wcm}^{-2}$ (which is little less than threshold intensity $I_\mathrm{th} \simeq 1.698 \times 10^{16}\mathrm{Wcm}^{-2}$), although the driver amplitude after the peak decreases the excited electron sphere continues to oscillate mostly in the anharmonic part of the potential where its eigenfrequency ω_eff resonates with $3\omega_\mathrm{l}$, leading to a resonance enhancement of the third harmonic radiation (also visible in Fig. 6.5a) even beyond the radiated power at the fundamental laser frequency. A stochastic behavior in the phase δ near the resonance $\omega_\mathrm{eff} = 3\omega_\mathrm{l}$ between $6 - 7$ laser cycles is clearly seen. At the threshold intensity $I_3 = I_\mathrm{th} \simeq 1.698 \times 10^{16}\mathrm{Wcm}^{-2}$ Fig. 6.5c shows harmonic radiation of higher orders occurring at the time before the NLR when $\omega_\mathrm{eff}/\omega_\mathrm{l}$ meets unity and the electron sphere becomes free ($\omega_\mathrm{eff}/\omega_\mathrm{l}$ approaches zero). After the NLR, only radiation at the frequency ω_l appears. Only the bound part of an electron trajectory is responsible for the harmonic emission in clusters. Thus the RSM resembles the harmonic emission of a single PIC particle in Fig. 6.3.

6.3.2 Collective radiation of non-interacting electrons

In the previous subsection harmonic emission was illustrated using a model where all electrons were frozen into a single sphere and coherently oscillating. In clusters, however, electrons can have different initial potential energies, i.e., different initial phases with respect to the laser field and "see" different total fields at a given laser intensity. Just looking at the harmonics spectrum in Fig. 6.5a for the low intensity I_1 one may think that higher order harmonics are possible if all electrons are well-bound. This is an artifact of the RSM. As an example, two well-bound electrons located just opposite to the cluster center (e.g., x and $-x$) when driven by the low intensity oscillating laser field will mostly radiate with opposite phase and the resultant radiation will certainly not contain higher frequencies than the spectrum in Fig. 6.5a. To simulate this situation within the RSM,

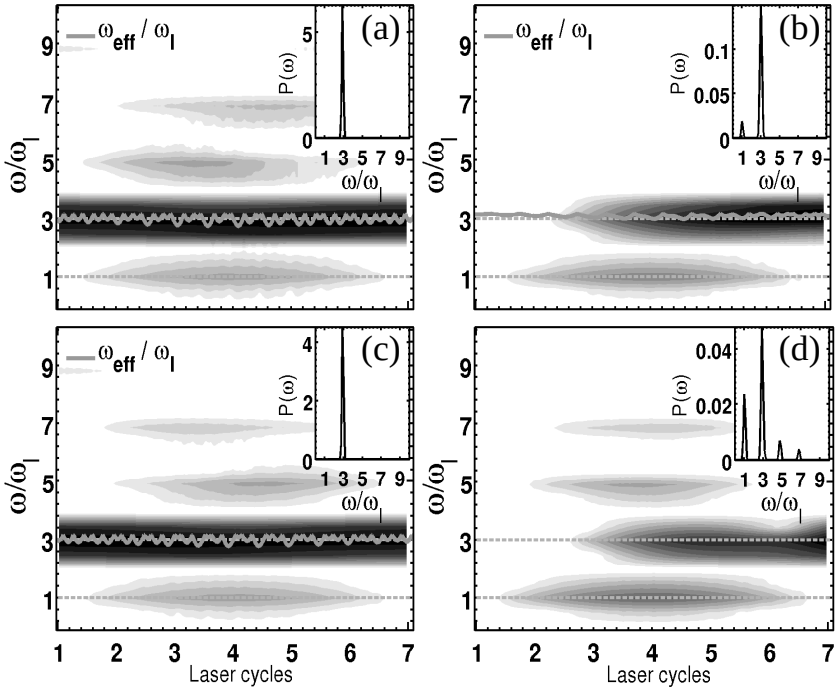

Figure 6.6: TF spectrograms of the dipole power $\log_{10} P(\omega)$ for three non-interacting electron spheres (a-c) and the normalized total dipole power (d) for an Ar_{1000} cluster of charge density $\rho \approx 30\rho_c$, i.e., $\omega_{Mie}/\omega_l \approx 3.15$. The laser intensity is 1.45×10^{15}Wcm^{-2} and the wavelength 800 nm. All three electron spheres remain bound.

we can think of an ensemble of a few non-interacting electron spheres centered at different initial positions within the radius of the fixed ion sphere.

We consider an Ar_{1000} cluster of fixed radius $R = 2.4$ nm, average charge density $\rho \approx 30\rho_c$ in an $n = 8$-cycle $\sin^2$-pulse as in Fig. 6.5. The laser wavelength is 800 nm. We take an ensemble of $N = 3$ identical, non-interacting electron spheres which are centered at $-R/2$, 0 and $R/2$ at time $t = 0$. For such a configuration we compute the harmonic spectra of the individual electrons (i.e., based on the individual accelerations $a_i(t)$) and the normalized total acceleration $A(t) = \sum_1^N a_i(t)/N$.

First we assume a low laser intensity 1.45×10^{15}Wcm^{-2} so that all electron spheres remain well-bound. In reality some outer ionization is also expected at this intensity. Figure 6.6 shows TF diagrams for the individual electron spheres (Fig. 6.6a-c) and the normalized total acceleration $A(t)$ (Fig. 6.6d). Insets show the corresponding harmonic spectra in the frequency domain. The bound spheres (Fig. 6.7a-c) oscillate near the Mie-frequency $\omega_{Mie}/\omega_l \approx 3.15$ and individually emit a strong third harmonic resonantly with the Mie-frequency. This situation can be compared to Fig. 6.5a (at I_2) where the third harmonic intensity emitted by a single electron sphere was much higher than the radiation at the fundamental. Figures 6.6a,c show TF plots for the electron spheres which started off the center at $-R/2$ and $R/2$ at time $t = 0$. Due to the opposite phases of their radiation the third harmonic emission cancels in the total spectra (Fig. 6.6d). The dominant contribution to the third harmonic in the total spectrum (Fig. 6.6d) thus comes

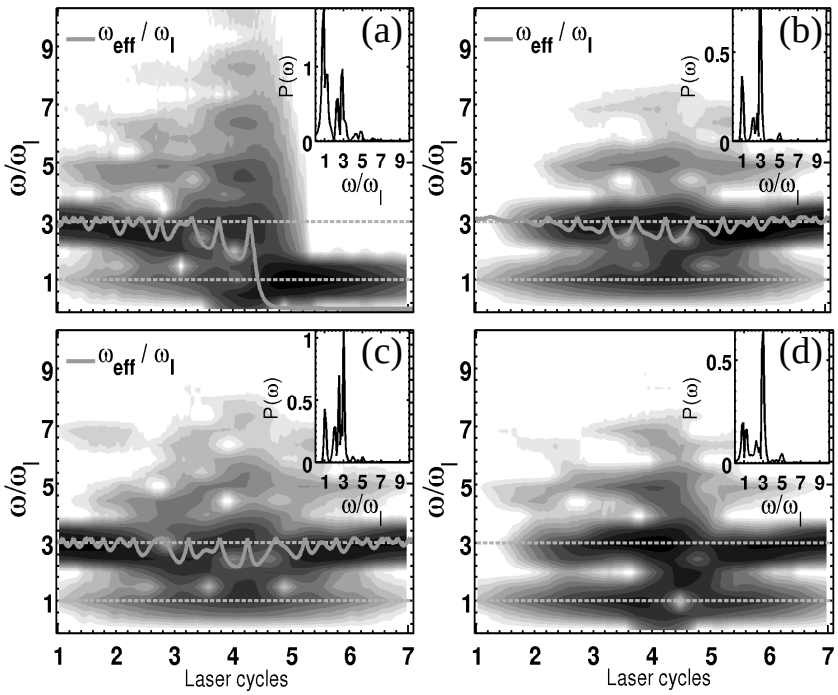

Figure 6.7: TF spectrograms corresponding to Fig. 6.6 at an intensity $1.45 \times 10^{16}\mathrm{Wcm}^{-2}$.

from the electron sphere which started at $x = 0$ at time $t = 0$ (Fig. 6.6b). It does not emit the third harmonic at early times since $\omega_{\mathrm{eff}}/\omega_{\mathrm{l}} = \omega_{\mathrm{Mie}}/\omega_{\mathrm{l}} = 3.15$ is off resonant. As the laser field increases, the electron sphere is drawn up the potential and from the pulse peak onwards it emits the third harmonic (as seen in Fig. 6.5b) which finally dominates the total spectrum (Fig. 6.6d).

Figure 6.7 shows the analogous TF diagram of the respective electron spheres in Fig. 6.6 at the higher laser intensity $1.45 \times 10^{16}\mathrm{Wcm}^{-2}$. One of the spheres becomes free (Fig .6.7a) while two remain bound (Figs .6.7b,c).

Figure 6.8a-f are the TF plots corresponding to an ensemble of $N = 11$ electron spheres (centered at equal distances between $-R/2$ to $R/2$) at an intensity $1.65 \times 10^{16}\mathrm{Wcm}^{-2}$. Only five of them are plotted in Figs. 6.8a-e and the total spectra is shown in Fig. 6.8f. Some of the particles remain bound (Figs.6.8b,c) while others become free (Figs.6.8a,d,e). The situation resembles already many body simulations (e.g., MD or PIC). There may be rescattering as clearly seen in Fig. 6.8d where the first flash appears upon leaving the cluster via NLR and the second because of rescattering. The situation is comparable to the PIC results in Fig. 6.3. The flashes occur stochastically and disappear in the net radiation (Fig. 6.8f).

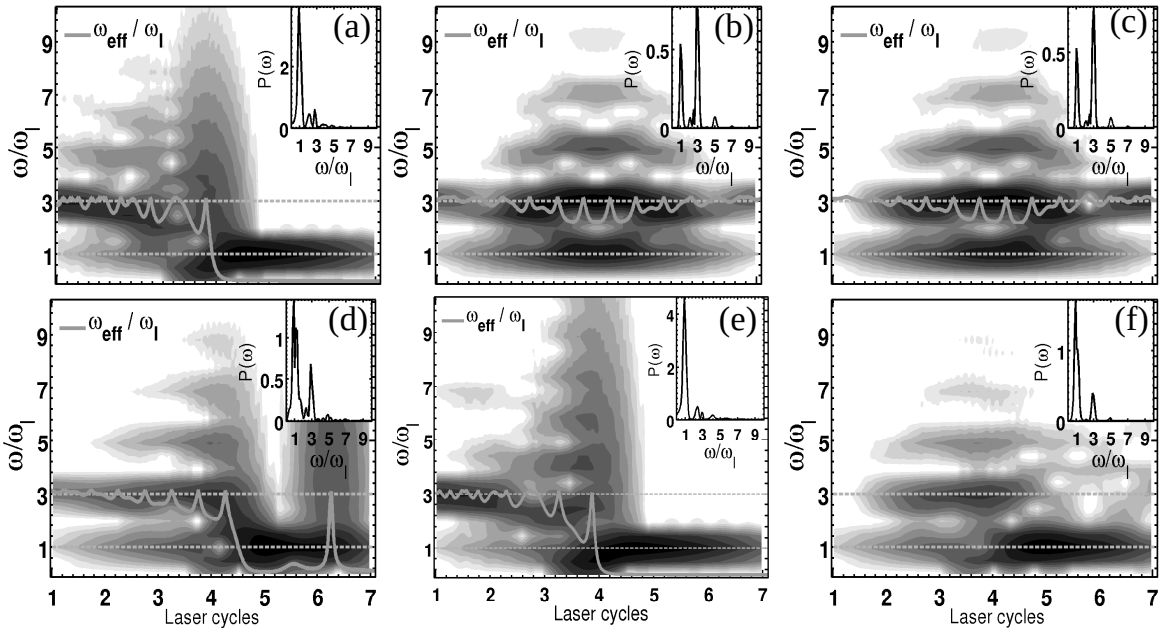

Figure 6.8: TF spectrogram corresponding to an ensemble of $N = 11$ non-interacting electron spheres. Only five of them are plotted in (a-e), the normalized total dipole power in (f). The laser intensity is $1.65 \times 10^{16}\mathrm{Wcm}^{-2}$. Other parameters are as in Fig.6.6.

6.4 Summary

In summary, we investigated numerically harmonic emission from laser-driven cluster nanoplasmas. The main contribution to the harmonic signal comes from electrons deeply bound inside the cluster potential. Such electrons emit only low-order harmonics with considerable efficiency since they sense a weakly anharmonic potential only. In contrast, electrons passing through the nonlinear resonance and leaving the cluster move along strongly disturbed trajectories. Their radiation, although intense and broad in wavelength, is incoherent due to the stochastic nature of the nonlinear resonance and therefore does not contribute to the net signal from the whole cluster. The time-frequency analysis of the dipole acceleration shows enhanced third and fifth harmonic emission when the Mie-frequency of the expanding cluster meets the respective harmonic frequencies, which is consistent with both previous theoretical studies [35, 87, 115, 116] and recent experiment [114]. A pump-probe experiment is proposed to measure the cluster charge density by detecting the dipole radiation at different time delays. This method can be used to monitor the inner and outer ionization dynamics of clusters.

Conclusion

In this thesis we studied the interaction of intense laser pulses with atomic clusters using three-dimensional particle-in-cell simulations and analytical models. The physics addressed included: (i) collisionless absorption, (ii) optimization of laser energy conversion, and (iii) harmonic generation in clusters. Because each chapter of this thesis was already summarized in place, only the main conclusions are highlighted here.

We showed that in the short-pulse regime efficient laser absorption and outer ionization occurs due to nonlinear resonance (NLR) absorption. At the time of NLR the instantaneous frequency of the electron motion in a time-dependent, anharmonic, effective potential transiently meets the laser frequency. NLR is the only possible absorption mechanism if the laser pulse is too short for the linear resonance to occur (or during the early cluster dynamics in longer pulses) and if electron-ion collisions are negligible.

Maximum ion energies are mainly carried by the ions of highest charge state which appear close to the cluster boundary along the laser polarization. For deuterium clusters, although ions are only singly charged, high energy ions are also emitted predominantly along the laser polarization because of the asymmetric electron dynamics in a linearly polarized laser field.

An optimization of laser energy conversion in a given cluster at a given laser intensity was envisaged with respect to the laser wavelength. It was shown that there exists an optimum laser wavelength which typically lies in the ultraviolet regime and may allow for a linear resonance during the early, rising part of a few-cycle pulse when the cluster expansion is inappreciable. The linear resonance for this optimal wavelength led to particularly efficient energy absorption and optimized average ion charge states much higher than for the conventional LR occurring in the expanding cluster in the long-pulse and long wavelength regime.

We investigated the harmonic emission from laser-driven cluster nanoplasmas. The main contribution to the harmonic signal was due to the deeply bound coherently oscillating electrons inside the cluster potential. The electrons leaving the cluster through the NLR emit incoherent radiation and therefore higher order harmonics are absent. We proposed a pump-probe experiment to measure the cluster charge density by detecting the dipole radiation at different time delays.

The following issues may be addressed in the future:

- The present particle-in-cell code applies to regimes where the dipole approximation is valid. To enable it for studies in the relativistic regime an inclusion of electromagnetic effects such as laser pulse propagation or ponderomotive forces is necessary.
- At present the ionization of the cluster atoms are modelled using over-the-barrier ionization only. Such an ionization model, however, is less applicable for short wavelengths where multiphoton ionization or even inner shell ionization may be significant. Hence the ionization model has to be extended in order to study the laser-cluster interaction in the regime of the new generation FEL light sources, for instance.

Appendix A

Perturbative solution of the rigid sphere model

We solve Eq. (3.13), i.e.,

$$\ddot{x} + \omega_{\rm Mie}^2 x + \alpha x^2 = -E_{\rm l}(t), \tag{A.1}$$

by the method of perturbation [72] in the region $r \leq 2$. The complementary solution $x_{\rm cp}$ and the particular integral $x_{\rm pi}$ of (A.1) satisfy, respectively, the equations

$$\ddot{x}_{\rm cp} + \omega_{\rm Mie}^2 x_{\rm cp} + \alpha x_{\rm cp}^2 = 0, \tag{A.2}$$

$$\ddot{x}_{\rm pi} + \omega_{\rm Mie}^2 x_{\rm pi} = -\alpha x_{\rm pi}^2 - E_{\rm l}(t). \tag{A.3}$$

Let, $x_{\rm cp}^{(0)}$, $x_{\rm cp}^{(1)}$ and $x_{\rm cp}^{(2)}$ be the $0^{\rm th}$, $1^{\rm st}$ and $2^{\rm nd}$ corrections for x and $\omega_{\rm Mie}$, $\omega^{(1)}$ and $\omega^{(2)}$ be the $0^{\rm th}$, $1^{\rm st}$ and $2^{\rm nd}$ corrections for the frequency ω so that $x_{\rm cp} = x_{\rm cp}^{(0)} + x_{\rm cp}^{(1)} + x_{\rm cp}^{(2)} + \cdots$ and $\omega = \omega_{\rm Mie} + \omega^{(1)} + \omega^{(2)} + \cdots$. To find $x_{\rm cp}$ we write

$$\ddot{x}_{\rm cp} + \omega_{\rm Mie}^2 x_{\rm cp} = -\alpha x_{\rm cp}^2, \tag{A.4}$$

and assume the $0^{\rm th}$ approximation as

$$x_{\rm cp}^{(0)} = a_0 \cos(\omega t + \delta_0). \tag{A.5}$$

However, if (A.5) is substituted in (A.4), the left hand side does not lead to zero. It means that $x_{\rm cp}^{(0)} = a_0 \cos(\omega t + \delta_0)$ is not an unperturbed solution. We rewrite (A.4) as

$$\frac{\omega_{\rm Mie}^2}{\omega^2}\, \ddot{x}_{\rm cp} + \omega_{\rm Mie}^2 x_{\rm cp} = -\alpha x_{\rm cp}^2 - (1 - \frac{\omega_{\rm Mie}^2}{\omega^2})\, \ddot{x}_{\rm cp}. \tag{A.6}$$

To the first approximation we substitute $x_{\rm cp}^{(0)}$ to the right hand side and $x_{\rm cp} = x_{\rm cp}^{(0)} + x_{\rm cp}^{(1)}$ to the left hand side of (A.6) and obtain

$$\ddot{x}_{\rm cp}^{(1)} + \omega_{\rm Mie}^2\, x_{\rm cp}^{(1)} = -\alpha \left[x_{\rm cp}^{(0)}\right]^2 - \frac{2\omega_{\rm cp}^{(1)}\omega_{\rm Mie}}{\omega^2}\, \ddot{x}_{\rm cp}^{(0)}, \tag{A.7}$$

where we have made the approximations $\omega^2 - \omega_{\rm Mie}^2 = 2\omega^{(1)}\omega_{\rm Mie} + [\omega^{(1)}]^2 \approx 2\omega^{(1)}\omega_{\rm Mie}$, $\omega_{\rm Mie}^2/\omega^2 = \left(1 + \omega^{(1)}/\omega_{\rm Mie}\right)^{-2} \approx \left(1 - 2\omega^{(1)}/\omega_{\rm Mie}\right)$ and $\left(1 - 2\omega^{(1)}/\omega_{\rm Mie}\right)\ \ddot{x}_{\rm cp}^{(1)} \approx \ddot{x}_{\rm cp}^{(1)}$ after

neglecting second order terms. To avoid the resonant term we let $\omega^{(1)} = 0$. Putting $x_{\rm cp}^{(0)}$ in (A.7) we get

$$\ddot{x}_{\rm cp}^{(1)} + \omega_{\rm Mie}^2\, x_{\rm cp}^{(1)} = A_0\left[1 + \cos(2\omega t + 2\delta_0)\right], \tag{A.8}$$

where $A_0 = -\alpha a_0^2/2$. Equation (A.8) is in-homogeneous. Its complementary function has the solution $x^{(1)} \sim \cos(\omega t + \delta_0)$ with $\omega^{(1)} = 0$. This does not lead to a solution with a frequency different from the unperturbed solution. The terms with the unperturbed frequency can be omitted to avoid the resonance term. The solution of (A.8) is

$$x_{\rm cp}^{(1)} = B_0\left[3 - \cos(2\omega t + 2\delta_0)\right], \tag{A.9}$$

were $B_0 = A_0/3\omega_{\rm Mie}^2 = -\alpha a_0^2/6\omega_{\rm Mie}^2$. To the second approximation we substitute $x_{\rm cp} = x_{\rm cp}^{(0)} + x_{\rm cp}^{(1)} + x_{\rm cp}^{(2)}$ and $\omega = \omega_{\rm Mie} + \omega^{(1)} + \omega^{(2)}$ in the left hand side and $x_{\rm cp} = x_{\rm cp}^{(0)} + x_{\rm cp}^{(1)}$ and $\omega = \omega_{\rm Mie} + \omega^{(1)}$ in the right hand side of (A.6) and obtain

$$\ddot{x}_{\rm cp}^{(2)} + \omega_{\rm Mie}^2 x_{\rm cp}^{(2)} = -2\alpha x_{\rm cp}^{(0)} x_{\rm cp}^{(1)} + 2\omega^{(2)}\omega_{\rm Mie}\, x_{\rm cp}^{(0)} - \alpha\left[x_{\rm cp}^{(1)}\right]^2. \tag{A.10}$$

Using $x_{\rm cp}^{(0)}$ and $x_{\rm cp}^{(1)}$ Eq. (A.10) can be written as

$$\ddot{x}_{\rm cp}^{(2)} + \omega_{\rm Mie}^2 x_{\rm cp}^{(2)} = \sum_{k=1,3} b_k \mathcal{C}_k, \tag{A.11}$$

with $b_1 = 2\omega^{(2)}\omega_{\rm Mie}a_0 - 5\alpha a_0 B_0$, $b_2 = 0$ and $b_3 = \alpha a_0 B_0 - 3\beta a_0^3 B_0/2$. For the absence of the resonant term from the solution, the coefficient of $\cos(\omega t + \delta_0)$ must be zero. Setting $b_1 = 0$, one obtains

$$\omega^{(2)} = -\frac{5\alpha^2 a_0^2}{12\omega_{\rm Mie}^3}. \tag{A.12}$$

The solution of (A.11) is

$$x_{\rm cp}^{(2)} = -\frac{b_3\cos(3\omega t + 3\delta_0)}{9\omega^2 - \omega_{\rm Mie}^2}. \tag{A.13}$$

We have omitted the term $\alpha[x_{\rm cp}^{(1)}]^2$ by considering this term small as compared to the other terms. But at a high laser intensity this term may contribute. Therefore we improve our approximation keeping the term $\alpha[x_{\rm cp}^{(1)}]^2$ and solve

$$\ddot{x}_{\rm cp}^{(3)} + \omega_{\rm Mie}^2 x_{\rm cp}^{(3)} = -\alpha[x_{\rm cp}^{(1)}]^2. \tag{A.14}$$

Substituting $x_{\rm cp}^{(1)}$ we get the solution of (A.14) as

$$x_{\rm cp}^{(3)} = -\frac{\alpha B_0^2}{2\omega_{\rm Mie}^2}\left[19 + 4\cos(2\omega_{\rm Mie}t + 2\delta_0) - \frac{\cos(4\omega_{\rm Mie}t + 4\delta_0)}{15}\right]. \tag{A.15}$$

The solution for $x_{\rm cp}$ up to the second order is given by

$$x_{\rm cp} = 3B_0 + \frac{b_0}{\omega_{\rm Mie}^2} + a_0\cos(\omega_{\rm Mie}t + \delta_0) - B_0\cos(2\omega_{\rm Mie}t + 2\delta_0) - \frac{b_3\cos\left(3\omega t + k\delta_0\right)}{9\omega^2 - \omega_{\rm Mie}^2} - \frac{\alpha B_0^2}{2\omega_{\rm Mie}^2}\left[19 + 4\cos(2\omega_{\rm Mie}t + 2\delta_0) - \frac{\cos(4\omega_{\rm Mie}t + 4\delta_0)}{15}\right]. \tag{A.16}$$

To find out the particular integral ($x_{\rm pi}$) which depends upon the driving field we consider an n-cycle pulse of electric field $E_{\rm l}(t) = E_0 \sin(\omega_{\rm l} t/2n)\cos(\omega_{\rm l} t)$ for simplicity and write $E_{\rm l}(t) = \sum_{k=1}^{2} f_k \sin(\omega_k t)$ with $f_1 = E_0/2$, $f_2 = -E_0/2$, $\omega_1 = (1 + 1/2n)\omega_{\rm l}$, $\omega_2 = (1 - 1/2n)\omega_{\rm l}$, $w_+ = \omega_1 + \omega_2 = 2\omega_{\rm l}$, $w_- = \omega_1 - \omega_2 = \omega_{\rm l}/n$. We assume the $0^{\rm th}$ approximation

$$x_{\rm pi}^{(0)} = \sum_{k=1}^{2} a_k \sin(\omega_k t) \tag{A.17}$$

to satisfy the $0^{\rm th}$ order equation

$$\ddot{x}_{\rm pi}^{(0)} + \omega_{\rm Mie}^2 x_{\rm pi}^{(0)} = E_{\rm l}(t). \tag{A.18}$$

Substituting (A.17) into (A.18) we get

$$\sum_{k=1}^{2} a_k \left(\omega_{\rm Mie}^2 - \omega_k^2\right) \sin(\omega_k t) = \sum_{k=1}^{2} f_k \sin(\omega_k t). \tag{A.19}$$

Equating the terms of identical k we obtain the amplitudes $a_k = f_k/(\omega_{\rm Mie}^2 - \omega_k^2)$ for $k = 1, 2$. We substitute $x_{\rm pi}^{(0)}$ to the right hand side and $x_{\rm pi} = x_{\rm pi}^{(0)} + x_{\rm pi}^{(1)}$ to the left hand side of (A.3) as a first approximation and obtain

$$\ddot{x}_{\rm pi}^{(1)} + \omega_{\rm Mie}^2\, x_{\rm pi}^{(1)} = -\alpha \left[x_{\rm pi}^{(0)}\right]^2. \tag{A.20}$$

Putting $x_{\rm pi}^{(0)}$ into (A.20) yields

$$\ddot{x}_{\rm pi}^{(1)} + \omega_{\rm Mie}^2\, x_{\rm pi}^{(1)} = A_0 + \frac{\alpha}{2} \sum_{k=1}^{2} a_k^2 \mathcal{C}_{2\omega_k} - \alpha a_1 a_2 \left(\mathcal{C}_{\omega_1 - \omega_2} - \mathcal{C}_{\omega_1 + \omega_2}\right). \tag{A.21}$$

We use the notation $\mathcal{C}_{\omega_k} = \cos(\omega_k t)$ and $\mathcal{S}_{\omega_k} = \sin(\omega_k t)$ and assume $A_0 = -\frac{\alpha}{2}\sum_{k=1}^{2} a_k^2$. The complementary function of (A.21) has the solution $x^{(1)} \sim \sin(\omega_{\rm Mie} t + \delta_0)$ with the unperturbed frequency $\omega_{\rm Mie}$. We can omit this resonance term and find

$$x_{\rm pi}^{(1)} = A_s + \sum_{k=1}^{2} B_k \mathcal{C}_{2\omega_k} + A_p\, \mathcal{C}_{\omega_1 + \omega_2} + A_m\, \mathcal{C}_{\omega_1 - \omega_2}, \tag{A.22}$$

with $A_s = -A_0/\omega_{\rm Mie}^2$, $A_p = \alpha a_1 a_2/(\omega_{\rm Mie}^2 - (\omega_1 + \omega_2)^2)$, $A_m = -\alpha a_1 a_2/(\omega_{\rm Mie}^2 - (\omega_1 - \omega_2)^2)$. In the second approximation we substitute $x_{\rm pi} = x_{\rm pi}^{(0)} + x_{\rm pi}^{(1)} + x_{\rm pi}^{(2)}$ in the left hand side and $x_{\rm pi} = x_{\rm pi}^{(0)} + x_{\rm pi}^{(1)}$ in the right hand side of (A.3). Keeping the terms first order in $x_{\rm pi}^{(1)}$ we obtain

$$\ddot{x}_{\rm pi}^{(2)} + \omega_{\rm Mie}^2 x_{\rm pi}^{(2)} = -2\alpha x_{\rm pi}^{(0)} x_{\rm pi}^{(1)}. \tag{A.23}$$

We substitute $x_{\rm pi}^{(0)}$ and $x_{\rm pi}^{(1)}$ in (A.23) and obtain

$$x_{\rm pi}^{(2)} = \sum_{j=1}^{2} \frac{A_j \mathcal{S}_{\omega_j}}{\omega_{\rm Mie}^2 - (\omega_j)^2} + \sum_{j,k=1}^{2,2} B_{jk} \left[\frac{\mathcal{S}_{2\omega_k+\omega_j}}{\omega_{\rm Mie}^2 - (2\omega_k+\omega_j)^2} - \frac{\mathcal{S}_{2\omega_k-\omega_j}}{\omega_{\rm Mie}^2 - (2\omega_k-\omega_j)^2} \right] + \sum_{j=1}^{2} D_j \left[\frac{\mathcal{S}_{\omega_1+\omega_2+\omega_j}}{\omega_{\rm Mie}^2 - (\omega_1+\omega_2+\omega_j)^2} - \frac{\mathcal{S}_{\omega_1+\omega_2-\omega_j}}{\omega_{\rm Mie}^2 - (\omega_1+\omega_2-\omega_j)^2} \right] + \sum_{j=1}^{2} E_j \left[\frac{\mathcal{S}_{\omega_1-\omega_2+\omega_j}}{\omega_{\rm Mie}^2 - (\omega_1-\omega_2+\omega_j)^2} - \frac{\mathcal{S}_{\omega_1-\omega_2-\omega_j}}{\omega_{\rm Mie}^2 - (\omega_1-\omega_2-\omega_j)^2} \right]. \quad \text{(A.24)}$$

The term $\alpha[x_{\rm pi}^{(1)}]^2$ is neglected by considering that this term is small as compared to the other terms. At a high intensity this term may also contribute. To improve the approximation we keep the term $\alpha[x^{(1)}]^2$ and solve

$$\ddot{x}_{\rm pi}^{(3)} + \omega_{\rm Mie}^2 x_{\rm pi}^{(3)} = -\alpha[x_{\rm pi}^{(1)}]^2. \quad \text{(A.25)}$$

Substituting $[x_{\rm pi}^{(1)}]^2$ in (A.25) leads to

$$\ddot{x}_{\rm pi}^{(3)} + \omega_{\rm Mie}^2 x_{\rm pi}^{(3)} = P_0 + P_1 \sum_{k=1}^{2} B_k \mathcal{C}_{2\omega_k} + P_2 \sum_{k=1}^{2} \frac{\alpha B_k^2}{2} \mathcal{C}_{4\omega_k} + P_3\, \mathcal{C}_{\omega_1+\omega_2} + P_4 \mathcal{C}_{\omega_1-\omega_2} + P_5\, \mathcal{C}_{2(\omega_1+\omega_2)} + P_6\, \mathcal{C}_{2(\omega_1-\omega_2)} + P_7\, \mathcal{C}_{3\omega_1+\omega_2} + P_8\, \mathcal{C}_{3\omega_1-\omega_2} + P_9\, \mathcal{C}_{\omega_1+3\omega_2} + P_{10}\, \mathcal{C}_{\omega_1-3\omega_2}\,. \quad \text{(A.26)}$$

The coefficients are: $P_0 = -\alpha \left[\frac{2A_s^2+B_1^2+B_2^2+A_p^2+A_m^2}{2} \right]$, $P_1 = -2\alpha A_s$, $P_2 = -1$, $P_3 = -\alpha(2A_sA_p + B_1A_m)$, $P_4 = -\alpha(2A_sA_m + B_2A_m + B_1A_p + B_2A_p)$, $P_5 = -\alpha(A_p^2/2 + B_1B_2)$, $P_6 = -\alpha(A_m^2/2 + B_1B_2)$, $P_7 = -\alpha B_1A_p$, $P_8 = -\alpha B_1A_m$, $P_9 = -\alpha B_2A_p$, $P_{10} = -\alpha B_2A_m$. The solution of $x_{\rm pi}^{(3)}$ is

$$x_{\rm pi}^{(3)} = Q_0 + \sum_{k=1}^{2} Q_{1k} \mathcal{C}_{2\omega_k} + \sum_{k=1}^{2} Q_{2k} \mathcal{C}_{4\omega_k} + Q_3\, \mathcal{C}_{\omega_1+\omega_2} + Q_4 \mathcal{C}_{\omega_1-\omega_2} + Q_5\, \mathcal{C}_{2(\omega_1+\omega_2)} + Q_6\, \mathcal{C}_{2(\omega_1-\omega_2)} + Q_7\, \mathcal{C}_{3\omega_1+\omega_2} + Q_8\, \mathcal{C}_{3\omega_1-\omega_2} + Q_9\, \mathcal{C}_{\omega_1+3\omega_2} + Q_{10}\, \mathcal{C}_{\omega_1-3\omega_2}\,, \quad \text{(A.27)}$$

with $Q_0 = P_0/\omega_{\rm Mie}^2$, $Q_{1k} = P_1B_k/(\omega_{\rm Mie}^2 - 4\omega_k^2)$, $Q_{2k} = P_2B_k^2/(2(\omega_{\rm Mie}^2 - 16\omega_k^2))$, $Q_3 = P_3/(\omega_{\rm Mie}^2 - (\omega_1+\omega_2)^2)$, $Q_4 = P_4/(\omega_{\rm Mie}^2 - (\omega_1-\omega_2)^2)$, $Q_5 = P_5/(\omega_{\rm Mie}^2 - 4(\omega_1+\omega_2)^2)$, $Q_6 = P_6/(\omega_{\rm Mie}^2 - 4(\omega_1-\omega_2)^2)$, $Q_7 = P_7/(\omega_{\rm Mie}^2 - (3\omega_1+\omega_2)^2)$, $Q_8 = P_8/(\omega_{\rm Mie}^2 - (3\omega_1-\omega_2)^2)$, $Q_9 = P_9/(\omega_{\rm Mie}^2 - (\omega_1+3\omega_2)^2)$, and $Q_{10} = P_{10}/(\omega_{\rm Mie}^2 - (\omega_1-3\omega_2)^2)$. Up to second order

corrections we find

$$
\begin{aligned}
x_{\rm pi} = A_s + A_p\,\mathcal{C}_{\omega_1+\omega_2} + A_m\,\mathcal{C}_{\omega_1-\omega_2} + \sum_{k=1}^{2}\left(a_k\mathcal{S}_{\omega_k} + B_k\,\mathcal{C}_{2\omega_k} + \frac{A_k\mathcal{S}_{\omega_k}}{\omega_{\rm Mie}^2-\omega_k^2}\right) \\
+\sum_{j,k=1}^{2,2} B_{jk}\left[\frac{\mathcal{S}_{2\omega_k+\omega_j}}{\omega_{\rm Mie}^2-(2\omega_k+\omega_j)^2} - \frac{\mathcal{S}_{2\omega_k-\omega_j}}{\omega_{\rm Mie}^2-(2\omega_k-\omega_j)^2}\right] \\
+\sum_{j=1}^{2} D_j\left[\frac{\mathcal{S}_{\omega_++\omega_j}}{\omega_{\rm Mie}^2-(\omega_++\omega_j)^2} - \frac{\mathcal{S}_{\omega_+-\omega_j}}{\omega_{\rm Mie}^2-(\omega_+-\omega_j)^2}\right] \\
+\sum_{j=1}^{2} E_j\left[\frac{\mathcal{S}_{\omega_-+\omega_j}}{\omega_{\rm Mie}^2-(\omega_-+\omega_j)^2} - \frac{\mathcal{S}_{\omega_--\omega_j}}{\omega_{\rm Mie}^2-(\omega_--\omega_j)^2}\right] \\
+Q_0 + \sum_{k=1}^{2} Q_{1k}\,\mathcal{C}_{2\omega_k} + \sum_{k=1}^{2} Q_{2k}\,\mathcal{C}_{4\omega_k} + Q_3\,\mathcal{C}_{\omega_1+\omega_2} + Q_4\,\mathcal{C}_{\omega_1-\omega_2} + Q_5\,\mathcal{C}_{2(\omega_1+\omega_2)} \\
+Q_6\,\mathcal{C}_{2(\omega_1-\omega_2)} + Q_7\,\mathcal{C}_{3\omega_1+\omega_2} + Q_8\,\mathcal{C}_{3\omega_1-\omega_2} + Q_9\,\mathcal{C}_{\omega_1+3\omega_2} + Q_{10}\,\mathcal{C}_{\omega_1-3\omega_2}. \qquad \text{(A.28)}
\end{aligned}
$$

The complete solution for the excursion x (up to the second order corrections) is obtained as $x = x_{\rm cp} + x_{\rm pi}$.

Appendix B

Conversion between SI units and atomic units

In this thesis we have mostly used atomic units. The conversion relations between SI and atomic units for the fundamental physical quantities are:

one atomic mass unit $= m_{\mathrm{e}} = 9.1094 \times 10^{-31}$ kg,
one atomic charge unit $= e = 1.6022 \times 10^{-19}$ C,
one atomic action unit $= \hbar = 1.0546 \times 10^{-34}$ Js,
one atomic length unit $= a_0 = 5.292 \times 10^{-11}$ m.

Note that in atomic units $4\pi\varepsilon_0 = 1$. Here ε_0 is the permittivity of vacuum, $-e$ and m_{e} are the charge and the mass of the electron, $\hbar$ is the Planck constant and a_0 is the Bohr radius. Based on the above relations the following conversion of various physical quantities are useful:

one atomic electric field strength unit $E_0 = e/4\pi\varepsilon_0 a_0^2 = 5.142 \times 10^{11}$ V/m,
one atomic energy unit $= \mathcal{E}_0 = eE_0 a_0 = 27.212$ eV,
one atomic frequency unit $= \omega_0 = \mathcal{E}_0/\hbar = 4.134 \times 10^{16}$ s^{-1},
one atomic time unit $= t_0 = \hbar/\mathcal{E}_0 = 0.024$ fs,
one atomic velocity unit $= v_0 = a_0/t_0 = c/137.04$,
one atomic intensity unit $= I_0 = c\varepsilon_0 E_0^2/2 = 3.51 \times 10^{16}$Wcm^{-2}.

Bibliography

[1] M.D. Perry and G. Mourou, Science **264**, 917 (1994).

[2] P. Gibbon and E. Forster, Plasma Phys. Controlled Fusion **38**, 769 (1996).

[3] D. Umstadter, Phys. Plasmas **8**, 1774 (2001).

[4] Molecules and clusters in intense laser fields, edited by Jan Posthumus (Cambridge University Press, Cambridge, U.K., 2001).

[5] U. Saalmann and J.M. Rost, J. Phys. B: At. Mol. Opt. Phys. **39**, R39-R77 (2006).

[6] V.P. Krainov and M.B. Smirnov, Physics Reports **370**, 237 (2002).

[7] T. Ditmire, R.A. Smith, J.W.G. Tisch, and M.H.R. Hutchinson, Phys. Rev. Lett. **78**, 3121 (1997).

[8] T. Ditmire, J.W.G. Tisch, E. Springate, M.B. Mason, N. Hay, J. Marangos, and M.H.R. Hutchinson, Nature (London) **386**, 54 (1997).

[9] V. Kumarappan, M. Krishnamurthy, and D. Mathur, Phys. Rev. A **67**, 43204 (2003).

[10] E. Springate, S.A. Aseyev, S. Zamith, and M.J.J. Vrakking, Phys. Rev. A **68**, 53201 (2003).

[11] C. Rose-Petruck, K.J. Schafer, K.R. Wilson, and C.P.J. Barty, Phys. Rev. A **55**, 1182 (1997).

[12] D. Bauer and A. Macchi, Phys. Rev. A **68**, 33201 (2003).

[13] Kenichi Ishikawa and Thomas Blenski, Phys. Rev. A **62**, 63204 (2000).

[14] F. Megi, M. Belkacem, M.A. Bouchene, E. Suraud, and G. Zwicknagel, J. Phys. B: At. Mol. Opt. Phys. **36**, 273 (2003).

[15] C. Jungreuthmayer, M. Geissler, J. Zanghellini, and T. Brabec, Phys. Rev. Lett. **92**, 133401 (2004).

[16] D. Bauer, J. Phys. B: At. Mol. Opt. Phys. **37**, 3085 (2004).

[17] Christian Siedschlag and Jan-Michael Rost, Phys. Rev. Lett. **93**, 43402 (2004).

[18] C. Jungreuthmayer, L. Ramunno, J. Zanghellini, and T. Brabec, J. Phys. B: At. Mol. Opt. Phys. **38**, 3029 (2005).

[19] T. Ditmire, T. Donnelly, A.M. Rubenchik, R.W. Falcone, and M.D. Perry, Phys. Rev. A **53**, 3379 (1996).

[20] T. Döppner, Th. Fennel, Th. Diederich, J. Tiggesbäumker, and K.H. Meiwes-Broer, Phys. Rev. Lett. **94**, 013401 (2005); T. Döppner, Th. Fennel, P. Radcliffe, J. Tiggesbäumker, and K.H. Meiwes-Broer, Eur. Phys. J. D **36**, 165 (2005).

[21] L. Köller, M. Schumacher, J. Köhn, S. Teuber, J. Tiggesbäumker, and K.H. Meiwes-Broer, Phys. Rev. Lett. **82**, 3783 (1999).

[22] S. Zamith, T. Martchenko, Y. Ni, S.A. Aseyev, H.G. Muller, and M.J.J. Vrakking, Phys. Rev. A **70**, 11201(R) (2004).

[23] I. Last and J. Jortner, Phys. Rev. A **60**, 2215 (1999).

[24] Ulf Saalmann and Jan-Michael Rost, Phys. Rev. Lett. **91**, 223401 (2003).

[25] Th. Fennel, G.F. Bertsch, and K.H. Meiwes-Broer, Eur. Phys. J. D **29**, 367 (2004).

[26] C. Siedschlag and J.M. Rost, Phys. Rev. A **71**, 31401 (2005).

[27] T. Martchenko, Ch. Siedschlag, S. Zamith, H. G. Muller, and M. J. J. Vrakking, Phys. Rev. A **72**, 53202 (2005).

[28] T. Taguchi, T.M. Antonsen, Jr., and H.M. Milchberg, Phys. Rev. Lett. **92**, 205003 (2004)

[29] Thomas M. Antonsen, Jr., Toshihiro Taguchi, Ayush Gupta, John Palastro, and Howard M. Milchberg Phys. Plasmas **12**, 56703 (2005).

[30] P. Mulser and M. Kanapathipillai, Phys. Rev. A **71**, 63201 (2005).

[31] P. Mulser, M. Kanapathipillai, and D.H.H. Hoffmann, Phys. Rev. Lett. **95**, 103401 (2005).

[32] D. Bauer and P. Mulser, J. Phys.: Conf. Ser. **11**, 169 (2005).

[33] Ph.A. Korneev, S.V. Popruzhenko, D.F. Zaretsky, W. Becker, Laser Phys. Lett. **2**, 452 (2005).

[34] P.B. Parks, T.E. Cowan, R.B. Stephens, and E.M. Campbell, Phys. Rev. A **63**, 63203 (2001).

[35] S.V. Fomichev, S.V. Popruzhenko, D.F. Zaretsky, and W. Becker, J. Phys. B: At. Mol. Opt. Phys. **36**, 3817 (2003).

[36] J.Y. Lin, H. Chu, M. Shen, Y. Xiao, C.H. Lee, S. Chen, and J. Wang, Optics Communications **231**, 375 (2004).

[37] V. Kumarappan, M. Krishnamurthy, D. Mathur, and L.C. Tribedi Phys. Rev. A **63**, 23203 (2001).

[38] S. Ter-Avetisyan, M. Schnürer, H. Stiel, U. Vogt, W. Radloff, W. Karpov, W. Sandner, and P.V. Nickles, Phys. Rev. E **64**, 36404 (2001).

[39] M. Krishnamurthy, D. Mathur, and V. Kumarappan Phys. Rev. A **69**, 33202 (2004).

[40] V. Kumarappan, M. Krishnamurthy, and D. Mathur, Phys. Rev. Lett. **87**, 85005 (2001).

[41] D.R. Symes, M. Hohenberger, A. Henig, and T. Ditmire, Phys. Rev. Lett. **98**, 123401 (2007).

[42] Y.I. Salamin, S.H. Hu, K.Z. Hatsagortsyan, C.H. Keitel, Phys. Rep. **427**, 41 (2006).

[43] L. Keldysh, Sov. Phys. JETP **20**, 1307 (1965).

[44] P. Agostini, F. Fabre, G. Mainfray, G. Petite, and N. Rahman, Phys. Rev. Lett. **42**, 1127 (1979).

[45] H.B. Bebb and A. Gold, Phys. Rev. **143**, 1 (1966).

[46] M. Perry, O. Landen, A. Szöke, and E. Campbell, Phys. Rev. A **37**, 747 (1988).

[47] E. Mevel, P. Breger, R. Trainham, G. Petite, and P. Agostini, Phys. Rev. Lett. **70**, 406 (1993).

[48] M. Protopapas, C.H. Keitel, and P.L. Knight, Reports on Progress in Physics **60**, 389 (1997).

[49] V.S. Popov, Physics-Uspekhi, **47**, 855 (2004).

[50] L.D. Landau and E.M. Lifshitz, *Quantum Mechanics* (Pergamon, Oxford, 1977).

[51] M. Ammosov, N. Delone, and V. Kramov, Sov. Phys. JETP **64**, 1191 (1986).

[52] H.A. Bethe and E.E. Salpeter, *Quantum mechanics of one- and two-electron atoms* (Plenum Publishing Corporation, New York, 1977).

[53] J. Eberly and J. Javanainen, Eur. J. Phys. **9**, 265 (1988).

[54] S. Augst, D. Strickland, D.D. Meyerhofer, S.L. Chin, and J.H. Eberly, Phys. Rev. Lett. **63**, 2212 (1989).

[55] S. Augst, D. Meyerhofer, D. Strickland, and S. Chin, J. Opt. Sot. Am. B **8**, 858 (1991).

[56] T. Auguste, P. Monot, L.A. Lompre, G. Mainfray, and C. Manus, J. Phys. B: At. Mol. Opt. Phys. **25**, 4181 (1992).

[57] M. Hirokane, S. Shimizu, M. Hashida, S. Okada, S. Okihara, F. Sato, T. Iida, and S. Sakabe, Phys. Rev. A **69**, 63201 (2004).

[58] W. Lotz, Z. Physik **206**, 205 (1967).

[59] W. Lotz, Z. Physik **216**, 241 (1968).

[60] F.F. Chen, *Introduction to Plasma Physics and Controlled Fusion, Vol. 1: Plasma Physics* (Plenum Press, New York, 1984).

[61] J.D. Jackson, *Classical Electrodynamics* (Wiley, New York, 1999).

[62] W.L. Kruer, *The Physics of Laser Plasma Interactions* (Addison-Wesley, New York, 1988).

[63] F. Brunel, Phys. Rev. Lett. **59**, 52 (1987).

[64] A. Getz and V. Krainov, JETP **101**, 80 (2005).

[65] C.K. Birdsall and A. B. Langdon, *Plasma Physics via Computer Simulation* (Adam Hilger, New York, 1991).

[66] R.W. Hockney and J.W. Eastwood, *Computer Simulation using Particles* (Institute of Physics Publishing, Bristol, 1988).

[67] A. Pukhov and J. Meyer-ter-Vehn, Phys. Rev. Lett. **79**, 2686 (1997).

[68] William H. Press, Brian P. Flannery, Saul A. Teukolsky, and William T. Vetterling, *Numerical Recipes in C : The Art of Scientific Computing* (Cambridge University Press, New York, 1992).

[69] M. Kundu and D. Bauer, Phys. Rev. Lett. **96**, 123401 (2006).

[70] M. Kundu and D. Bauer, Phys. Rev. A **74**, 63202 (2006).

[71] G.L. Kotkin and V.G. Serbo, *Collection of problems in classical mechanics* (Pergamon, Oxford, 1971).

[72] L.D. Landau and E.M. Lifshitz, *Mechanics* (Pergamon, Oxford, 1980).

[73] I.V. Hertel, T. Laarmann, and C.P. Schulz, Adv. At. Mol. Opt. Phys. **50**, 219 (2005).

[74] A. Jaroń-Becker, A. Becker, and F.H.M. Faisal, Phys. Rev. Lett. **96**, 143006 (2006).

[75] T. Ditmire, Contemporary Physics **38**, 315 (1997).

[76] T. Ditmire, J.W.G. Tisch, E. Springate, M.B. Mason, N. Hay, J.P. Marangos, and M.H.R. Hutchinson, Phys. Rev. Lett. **78**, 2332 (1997).

[77] M. Krishnamurthy, J. Jha, D. Mathur, Ch. Jungreuthmayer, L. Ramunno, J. Zanghellini and T. Brabec, J. Phys. B: At. Mol. Opt. Phys. **39**, 625 (2006).

[78] M. Lezius, S. Dobosz, D. Normand, and M. Schmidt Phys. Rev. Lett. **80**, 261 (1998).

[79] V. Kumarappan, M. Krishnamurthy, and D. Mathur, Phys. Rev. A **66**, 33203 (2002).

[80] E. Springate, N. Hay, J.W.G. Tisch, M.B. Mason, T. Ditmire, M.H.R. Hutchinson, and J.P. Marangos, Phys. Rev. A **61**, 63201 (2000).

[81] Y.L. Shao, T. Ditmire, J.W.G. Tisch, E. Springate, J.P. Marangos, and M.H.R. Hutchinson, Phys. Rev. Lett. **77**, 3343 (1996).

[82] L.M. Chen, J.J. Park, K.H. Hong, I.W. Choi, J.L. Kim, J. Zhang and C.H. Nam, Phys. Plasmas **9**, 3595 (2002).

[83] T. D. Donnelly, T. Ditmire, K. Neuman, M. D. Perry, and R. W. Falcone, Phys. Rev. Lett. **76**, 2472 (1996).

[84] J.W.G. Tisch, T. Ditmire, D.J. Fraser, N. Hay, M.B. Mason, E. Springate, J.P. Marangos, and M.H.R. Hutchinson, J. Phys. B: At. Mol. Opt. Phys. **30**, 709 (1997).

[85] C. Vozzi, M. Nisoli, J-P. Caumes, G. Sansone, S. Stagira, S. De Silvestri, M. Vecchiocattivi, D. Bassi, M. Pascolini, L. Poletto, P. Villoresi, and G. Tondello, Appl. Phys. Lett. **86**, 111121 (2005).

[86] M.B. Smirnov and V.P. Krainov, Phys. Rev. A **69**, 43201 (2004).

[87] M.V. Fomyts'kyi, B.N. Breizman, A.V. Arefiev, and C. Chiu, Phys. Plasmas **11**, 3349 (2004).

[88] T. Ditmire, J. Zweiback, V.P. Yanovsky, T.E. Cowan, G. Hays, and K.B. Wharton, Nature (London) **398**, 489 (1999).

[89] J. Zweiback, R.A. Smith, T.E. Cowan, G. Hays, K.B. Wharton, V.P. Yanovsky, and T. Ditmire, Phys. Rev. Lett. **84**, 2634 (2000).

[90] K.W. Madison, P.K. Patel, D. Price, A. Edens, M. Allen, T.E. Cowan, J. Zweiback, and T. Ditmire, Phys. Plasmas **11**, 270 (2004).

[91] K.W. Madison, P.K. Patel, M. Allen, D. Price, R. Fitzpatrick, and T. Ditmire, Phys. Rev. A **70**, 53201 (2004).

[92] G.M. Petrov, J. Davis, and A.L. Velikovich, Plasma Phys. Controlled Fusion **48**, 1721 (2006).

[93] F. Buersgens, K.W. Madison, D.R. Symes, R. Hartke, J. Osterhoff, W. Grigsby, G. Dyer, and T. Ditmire, Phys. Rev. E **74**, 16403 (2006).

[94] A. Gupta, T.M. Antonsen, T. Taguchi, and J. Palastro, Phys. Rev. E **74**, 46408 (2006).

[95] Hongyu Li, Jiansheng Liu, Cheng Wang, Guoquan Ni, Ruxin Li, and Zhizhan Xu, Phys. Rev. A **74**, 23201 (2006).

[96] S. Sakabe, S. Shimizu, M. Hashida, F. Sato, T. Tsuyukushi, K. Nishihara, S. Okihara, T. Kagawa, Y. Izawa, K. Imasaki, and T. Iida, Phys. Rev. A **69**, 23203 (2004).

[97] K.J. Mendham, J.W.G. Tisch, M.B. Mason, N. Hay, R.A. Smith, and J.P. Marangos, J. Phys. B: At. Mol. Opt. Phys. **35**, 663 (2002).

[98] I. Last and J. Jortner, Phys. Rev. Lett. **87**, 33401 (2001), I. Last and J. Jortner, J. Phys. Chem. A **106**, 10877 (2002), I. Last and J. Jortner, J. Chem. Phys. **121**, 8329 (2004).

[99] M. Hohenberger, D.R. Symes, K.W. Madison, A. Sumeruk, G. Dyer, A. Edens, W. Grigsby, G. Hays, M. Teichmann, and T. Ditmire, Phys. Rev. Lett. **95**, 195003 (2005)

[100] J. Jha, D. Mathur, and M. Krishnamurthy, Appl. Phys. Lett. **88**, 041107 (2006).

[101] Yuji Fukuda, Koichi Yamakawa, Yutaka Akahane, Makoto Aoyama, Norihiro Inoue, Hideki Ueda, and Yasuaki Kishimoto, Phys. Rev. A **67**, 61201 (2003).

[102] K. Kondo, A. B. Borisov, C. Jordan, A. McPherson, W. A. Schroeder, K. Boyer, and C. K. Rhodes, J. Phys. B **30**, 2707 (1997).

[103] W. A. Schroeder, F. G. Omenetto, A. B. Borisov, J. W. Longworth, A. McPherson, C. Jordan, K. Boyer, K. Kondo, and C. K. Rhodes, J. Phys. B **31**, 5031 (1998).

[104] A. McPherson, B. D. Thompson, A. B. Borisov, K. Boyer, and C. K. Rhodes, Nature (London) **370**, 631 (1994).

[105] H. Wabnitz *et al.*, Nature (London) **420**, 482 (2002).

[106] S. Namba, N. Hasegawa, M. Nishikino, T. Kawachi, M. Kishimoto, K. Sukegawa, M. Tanaka, Y. Ochi, K. Takiyama, and K. Nagashima, Phys. Rev. Lett. **99**, 043004 (2007).

[107] G.M. Petrov and J. Davis, Phys. Plasmas **13**, 033106 (2006).

[108] J. Davis, G.M. Petrov, and A. Velikovich, Phys. Plasmas **14**, 060701 (2007).

[109] G.M. Petrov, J. Davis, A.L. Velikovich, P.C. Kepple, A. Dasgupta, R.W. Clark, A.B. Borisov, K. Boyer, and C.K. Rhodes, Phys. Rev. E **71**, 036411 (2005).

[110] M. Kundu, S.V. Popruzhenko, and D. Bauer, Phys. Rev. A **76**, 033201 (2007).

[111] J. Andruszkow *et al.*, Phys. Rev. Lett. **85**, 3825 (2000).

[112] V. Ayvazyan *et al.*, Phys. Rev. Lett. **88**, 104802 (2002).

[113] I.Yu. Kolstyukov, JETP **100**, 903 (2005).

[114] B. Shim, G. Hays, R. Zgadzaj, T. Ditmire, and M.C. Downer, Phys. Rev. Lett. **98**, 123902 (2007).

[115] S.V. Fomichev, D.F. Zaretsky, D. Bauer, and W. Becker, J. Phys. B **37**, L175 (2003).

[116] S.V. Fomichev, D.F. Zaretsky, D. Bauer, and W. Becker, Phys. Rev. A **71**, 13201 (2005).

[117] A.J. Lichtenberg and M.A. Lieberman, *Regular and Chaotic Dynamics* (Springer, New York, 1982).

[118] A similar behavior was observed in classical ensemble simulations of atomic HG [G. Bandarage, A. Maquet, T. Ménis, R. Taïeb, V. Véniard, and J. Cooper, Phys. Rev. A **46**, 380 (1992)].

Thanks

I convey my sincere thanks to my supervisor PD Dr. Dieter Bauer. His encouragement, friendly supervision and continuous support in many situations were indeed valuable.

I would like to thank Prof. Christoph H. Keitel for the excellent working atmosphere and the facilities provided in his division.

Without the excellent computational facility this thesis would not have been completed. Thanks to Peter Brunner and all members of the computer maintenance. Thanks to Martina Weizmann, Vera Beyer, all people in the administration, colleagues and friends from the theory and experimental divisions of the Max–Planck–Institute for Nuclear Physics in Heidelberg, for the help whenever needed.

To the Max-Planck society and Deutsche Forschungsgemeinschaft (DFG) I thank for the financial support and the excellent working facilities.

I convey my thank to the examiners Prof. Markus Oberthaler, Prof. Peter Bachert and Prof. Ralf Klessen from the university of Heidelberg.

My sincere thanks to Prof. P.K. Kaw and Prof. A. Sen of the Institute for Plasma Research (IPR), India, for granting me leave to pursue my PhD thesis work. I remember the moment when I asked Prof. Kaw regarding my thesis. His support was very crucial for me.

Thanks to Dr. S.P. Deshpande, Dr. S. Chaturvedi of IPR and Dr. H. Ramachandran presently at the Indian Institute of Technology, Madras. I learnt many things from all of you. To all my other colleagues and friends, from IPR, I would like to say "thank you" for many sharing moments which I cannot all list here.

Thanks to that woman (I do not know her name and she is not alive today) in the then neighborhood who put me in the primary school and showed me the light of education. I convey many thanks to Ajay Basu who guided me back into studies with his valuable time. His heavenly departure during my thesis was a shock to me. Thanks to Narendranath Bhowmick, my high school teacher, for standing behind me always and providing a place at his home for my studies. Thanks to other people who supported me during difficulties.

I am indebted to my elder brother and mother who brought up me amidst our poverty after I lost my father in the early childhood. The most difficult time I ever faced was the demise of my mother when I was about to finalize this thesis. I pray my parent's souls may rest in peace. Thanks to Shonku and my parents-in-law for supporting me always. My most personal thanks go to my wife Rinku and my loving daughter Anushka for their sacrifice, love and encouragement.

Thank you !